Karin Margit Friess, BSc

Properties of lead-free dielectrics: Effects of ionic radii and electronegativity difference

MASTER'S THESIS

to achieve the university degree of

Diplom-Ingenieurin

Master's degree programme: Technical Chemistry

submitted to

Graz University of Technology

Supervisor

Ao.Univ.-Prof. Dipl.-Ing. Dr.techn. Klaus Reichmann

Institute for Chemistry and Technology of Materials

Graz, October 2017

EIDESSTATTLICHE ERKLÄRUNG

Ich erkläre an Eides statt, dass ich die vorliegende Arbeit selbstständig verfasst, andere als die angegebenen Quellen/Hilfsmittel nicht benutzt und die den benutzten Quellen wörtlich und inhaltlich entnommene Stellen als solche kenntlich gemacht habe.

Graz, am …………………………… ………………………………………………..
(Unterschrift)

STATUTORY DECLARATION

I declare that I have authored this thesis independently, that I have not used other than the declared sources / resources, and that I have explicitly marked all material which has been quoted either literally or by content from the used sources.

…………………………… ………………………………………………..
date (signature)

Kurzfassung

Ferroelektrische und antiferroelektrische Materialien, die zurzeit in Leistungskondensatoren mit hoher Ladungsdichte eingesetzt werden, enthalten in vielen Fällen Blei. Seit vielen Jahren wird versucht, wo immer es möglich ist, dieses giftige Schwermetall aus Produkten zu verbannen.

Das umweltfreundliche, bleifreie antiferroelektrische Natriumniobat (NN) wurde Mitte des 20. Jahrhunderts entdeckt. Aufgrund der vielen polymorphen Phasenübergänge und ihrer exklusiven Eigenschaften vor allem in festen Lösungen mit $KNbO_3$ hat dieses System die Aufmerksamkeit der Wissenschaftler immer schon auf sich gezogen. Einige Jahre später stieg die Nachfrage nach antiferrolektrischen Dielektrika in der Energiespeicherung an. Deshalb hat $NaNbO_3$ wieder ein beträchtliches Interesse an der Erforschung der Struktur und der Phasenübergänge gewonnen.

Im Allgemeinen weisen antiferroelektrische Materialien charakteristische Doppelhysteresekurven auf. Aber in der NN-Keramik wird es kaum beobachtet, da eine metastabile ferroelektrische (FE) Phase vorliegt, die durch verschiedene Parameter induziert wird und die das Zurückschalten in den antiferroelektrischen Zustand hemmt.

Dennoch wird in einer Publikation gezeigt, dass die antiferroelektrische Phase in Natriumniobat durch die Bildung fester Lösungen mit diversen Dotierstoffen wie $CaZrO_3$ und $SrZrO_3$ stabilisiert werden kann. Dies ist auf die Reduktion des Toleranzfaktors und die Steigerung der durchschnittlichen Elektronegativitätsdifferenz zwischen Kationen und Sauerstoff zurückzuführen. Zur Herstellung der festen Lösungen wird das Mischoxidverfahren verwendet. Anschließend werden die Proben bei 1050 °C kalziniert und 1350 °C gesintert. Die Struktur sowie die dielektrischen Eigenschaften der entsprechenden Proben werden durch folgende Charakterisierungsmethoden ermittelt: Röntgendiffraktometrie, Kleinsignalmessungen und Polarisationsmessungen. Letztere Methode wird angewendet um antiferroelektrische Eigenschaften wie Schaltfelder, Sättigungspolarisation und Hysteresenverlust zu erhalten.

Da dieses Konzept für die Stabilisierung der antiferroelektrischen Phase in der Perowskit-Struktur vielversprechend zu sein scheint, wird es auf andere Materialsys-

teme übertragen. Als Alternative zu $NaNbO_3$ wird $BiYbO_3$, welches bereits als Bestandteil von Relaxorsystemen untersucht wurde, fokussiert. Weiters werden $CaZrO_3$ und $SrZrO_3$ als Grundmaterial auserwählt. Wieder werden diese Systeme mit verschiedenen Ionen und verschiedenen Konzentrationen substituiert und auf die strukturellen und dielektrischen Modifikationen genauer untersucht.

Aufgrund der gewonnenen Daten wird ersichtlich, dass die Stabilisierung der antiferroelektrischen Phase von $NaNbO_3$ nicht nur von der Substitution von verschiedenen Dotierstoffen abhängt, sondern auch die Bearbeitung der Probe ausschlaggebend ist. Denn im Vergleich zur Literatur wird ersichtlich, dass die geformten Materialien nur paraelektrisches Verhalten zeigen. Ebenso kann man erkennen, dass sich dieses Konzept nicht auf jedes System übertragen lässt.

Abstract

Ferroelectric and antiferroelectric materials currently used in high charge density capacitors contain lead in many cases. For many years it has been tried wherever it is possible to ban this toxic heavy metal from products.

In the middle of the 20th century the eco-friendly, lead-free antiferroelectric sodium niobate (NN) was discovered. This system has always attracted the attention of scientists due to its many polymorphic phase transitions and its exclusive properties especially in solid solutions with $KNbO_3$. A few years later the demand of antiferroelectric dielectrics in energy storage is increased. Therefore $NaNbO_3$ has again gained considerable interest on the investigation of the structure and the phase transitions.

Commonly antiferroelectric materials exhibit characteristic double hysteresis curves. But in the NN ceramics it is hardly observed due to a metastable ferroelectric (FE) phase induced by different parameters that inhibits back-switching to the antiferroelectric state.

In a publication, it has been shown that the antiferroelectric phase in sodium niobate can be stabilized by the formation of solid solutions with various doping agents such as $CaZrO_3$ and $SrZrO_3$. Primarily this is attributed to the reduction of the tolerance factor and increase in the average electronegativity difference between cations and oxygen. Solid solutions are prepared by using the mixed oxide process. Subsequently the samples are calcinated at 1050 °C and sintered at 1350 °C. The structure and the dielectric properties of the corresponding samples are determined by the common characterization methods: X-ray diffraction, small signal measurements and polarization measurements. The latter method is used to obtain antiferroelectric properties such as switching fields, saturation polarization and hysteretic losses.

Since this concept for the stabilization of the antiferroelectric phase in the perovskite structure appeared to be promising it is transmitted to other material systems. $BiYbO_3$, which has already been studied as a component of relaxation systems, is being focussed as an alternative to $NaNbO_3$. Furthermore, $CaZrO_3$ and $SrZrO_3$ are also chosen as raw material. Again these systems are substituted with various ions and different concentrations and examined more closely for the structural and dielectric modifications.

Based on the obtained data, the stabilization of the antiferroelectric phase of $NaNbO_3$ is not only dependent on the substitution of different dopants, but also the processing of the sample is decisive. Compared with literature, it can be clarified that the formed materials only show paraelectric behaviour. Likewise, it can be seen that this concept cannot be applied to each system.

Acknowledgement

During my studies and for finalizing this work, the support of many people was necessary.

First of all, I would like to demonstrate my gratefulness to Prof. Klaus Reichmann for accepting me in his working group and supporting me throughout my stay with his superior technical knowledge. It was a pleasure for me to work in this field I really relish.

Furthermore I want to thank Prof. Brigitte Bitschnau, Prof. Franz Mautner and Prof. Jörg Albering for recording the XRD measurements and for helping me to characterize the spectra. Also I want to acknowledge the help of Christina Albering for supplying all the chemicals needed and the EPCOS OHG for the sample preparation.

Special thanks belong to my colleagues Isabel and Verena for the helpful discussions and for spending many hours together. Additionally I want to thank all my friends for giving courage at hard times.

Moreover I like to thank Markus, who tolerates me during stressful times and has always a sympathetic ear for me.

Last but not least, I want to thank my family for giving me the chance to study and for believing in me in every situation. Thank you for being like you are.

Table of contents

1 Introduction

Antiferroelectric materials with perovskite type structure (ABO_3) such as lead zirconate titanate (PZT) and lead-lanthanum zirconate titanate (PLZT) have been widely examined in literature and are used for many electronic applications over decades.[1] However at the beginning of the 21st century the Restriction of Hazardous Substances Directive (RoHS) was coming into force, which gives a limit for the use of lead because of its harmful impact to the environment and the health.[2]

Eco-friendly lead-free materials also suffer from drawbacks. For example $BiFeO_3$ (BF) shows high leakage currents due to Fe^{2+}/Fe^{3+} valency variation. $NaNbO_3$ (NN) demonstrates an irreversible phase transition to ferroelectric which is induced by temperature, electrical field and mechanical stress.[3] However Shimizu et al. claim that the insertion of various doping agents into the lattice leads to a stabilization of the antiferroelectric phase in the NN ceramics.[4]

Dopants have a big influence on the properties of a material and its structure. Through different factors like ionic size, atomic weight, electronegativity, concentration of A-site vacancies and electronic configurations the stability of the antiferroelectric phase can be controlled. Shimizu et al. stabilized this lead-free system by the formation of solid solutions with $CaZrO_3$ and $SrZrO_3$. They attribute this stabilization to the lowering of the tolerance factor t and raising the average electronegativity difference X.[5], [4]

The objective of this thesis is to investigate the dielectric properties of the lead-free system $x\mathrm{CaZrO_3} - (1\text{-}x)\mathrm{NaNbO_3}$ and try to reproduce the results from literature. Further it is intended to transmit the concepts applied on $NaNbO_3$ to other material systems. For this purpose $BiYbO_3$ was chosen, which was investigated as a component of relaxor dielectrics, such as $BaTiO_3$-$BiFeO_3$-$BiYbO_3$ solid solutions.[6] The influence of the constituents of the solid solution with $CaZrO_3$ and $SrZrO_3$ as well as rare earth oxides such as La_2O_3 on the properties densification, shrinkage, permittivity, loss factor, switching field, saturation polarization and hysteretic losses are determined.

2 General Aspects

The following chapter describes the relationship between the structure and the properties in antiferroelectric compounds.

Polar oxide materials with perovskite structure can be substituted by different ions at the A- and B-site to improve the stability region of the antiferroelectric phase. Many effects such as ionic size, electronegativity and polarizability are suggested to influence this phase and are examined in this thesis.[4], [7]

2.1 Stabilization of the Antiferroelectric Phase of Sodium Niobate

Sodium niobate (NN) has always attracted the attention of scientists due to its many polymorphic phase transitions and its exclusive properties especially in solid solutions with $KNbO_3$. This environmentally acceptable, lead-free antiferroelectric system possesses a large number of phase transitions, therefore the main focus of research has been laid on the investigation of the structure and the phase transitions after its discovery in the year 1949.[8], [9], [10], [11]

In the 1990s $NaNbO_3$ has gained again considerable interest because of the increased demand in the use of antiferroelectric dielectrics in energy storage and high-switch power supplies.[12], [13]

In general antiferroelectric materials exhibit characteristic double hysteresis curves. However in the NN ceramics this behaviour is hardly observed due to a metastable ferroelectric (FE) phase induced by temperature, mechanical stress and electrical field that inhibits back-switching to the antiferroelectric state.[12], [3]

Shimizu et al. [4], [7] have discovered that the antiferroelectric (AFE) phase in this system can be stabilized by the formation of solid solutions with $CaZrO_3$ and $SrZrO_3$. They attribute this stabilization to the lowering of the tolerance factor t and raising the average electronegativity difference X. Also the polarizability is lowered by the simultaneous substitution of Ca^{2+} and Zr^{4+} ions in the Na and Nb sites, correspondingly, while maintaining charge neutrality.

$CaZrO_3$ is a common dopant in a variation of ferroelectric perovskites. It has been established to enhance the piezoelectric characteristics of ferroelectrics, for example in $BaTiO_3$- and $(K_{0.5}Na_{0.5})NbO_3$-based ceramics.[14], [15] But for the antiferroelectric materials, primarily for the lead-free configurations, its doping effect on the antiferroelectricity development has not yet been investigated. However in Figure 1 excellent results can be shown with the substitution of $CaZrO_3$ in the NN-systems. Also $SrZrO_3$ indicates good results in the stabilization of the antiferroelectric phase.[4], [7]

Figure 1 shows a plot of the tolerance factor and the electronegativity difference for $(Na_{1-x}A^{2+}{}_x)(Nb_{1-x}B^{4+}{}_x)O_3$ compositions, where (A, B) are termed for following dopants: (Ca, Zr), (Ca, Hf), (Sr, Zr) and (Sr, Hf). Furthermore a molar content $x = 0.00 - 0.10$ is selected. The dotted lines are drawn at the tolerance factor of lead zirconate (PZ) and at the electronegativity difference in strontium titanate (ST), respectively. The abbreviation CZNN stands for the Ca- and Zr-substitution in the NN system, which has achieved the lowest t.[4], [7]

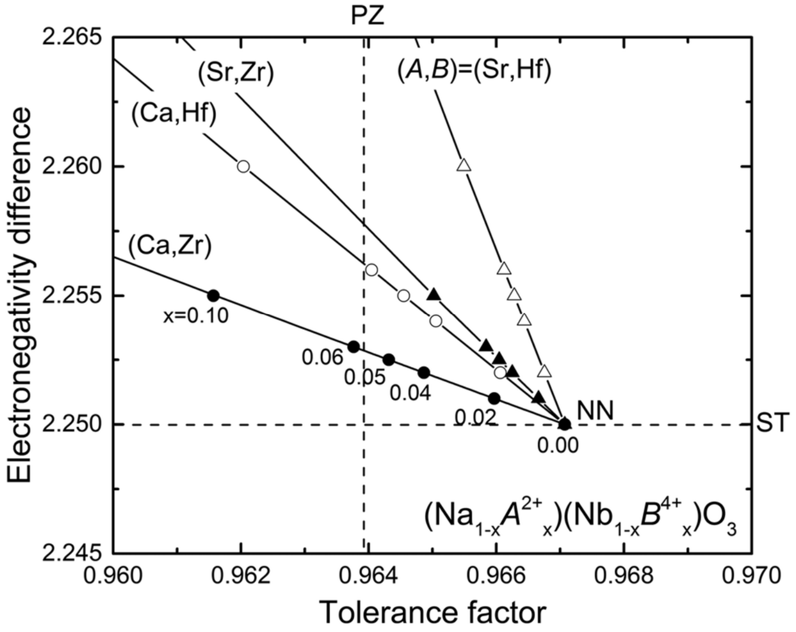

Figure 1: Tolerance factor t versus averaged electronegativity difference X for the lead-free antiferroelectric $(Na_{1-x}A^{2+}{}_x)(Nb_{1-x}B^{4+}{}_x)O_3$ system. The vertical dotted line is placed at the tolerance factor t for $PbZrO_3$ (PZ) and the horizontal dotted line is placed at the electronegativity difference X in $SrTiO_3$ (ST). Picture taken from Shimizu et al. Dalton Trans., 2015.

The preparation for the CZNN ceramics was done through the solid state method using a calcination temperature in the range of 1000 °C and 1150 °C with 3 hours holding time in an air atmosphere. The sintering time is chosen between 1320 °C and 1400 °C with a holding time of 2 hours and the process was done again in an air atmosphere. Afterwards dielectric and polarization measurements were done on the samples with the highest relative density. For polarization measurement the samples were polished to a thickness of 0.3 mm and sputtered with platinum electrodes.[4]

At room temperature NN ceramics exhibits typical square-shaped polarization curves, whereas the 2 mol% substitution of Calcium and Zirconium in NN ceramics shows an antiferroelectric behaviour. As seen in Figure 2 the measurements at 120°C yield typical double hysteresis loops for the substituted CZNN ceramics. At a concentration of 5 mol% the field-induced polarization has dropped drastically from ~40 to ~15 μC/cm^2, which shows an effect in the reduction of the tolerance factor. Moreover with rising substitution, the AFE-to-FE switching field has tripled from ~50 to ~150 kV/cm. With a concentration of 6 mol% and 10 mol% $CaZrO_3$ in the NN system no double hysteresis loops can be observed. For the CZNN10 sample it was found that this composition exceeds the solubility range.[4]

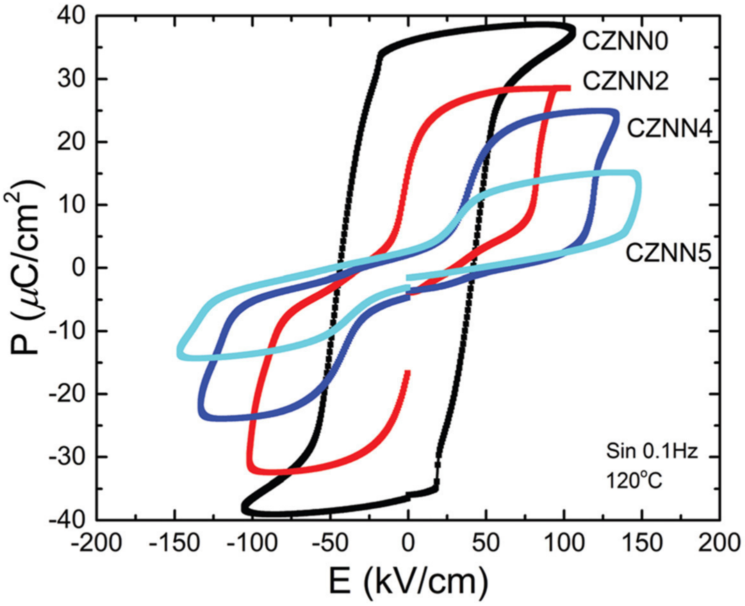

Figure 2: Polarization versus electrical field in the CZNN ceramics at 120°C. Picture taken from Shimizu et al. Dalton Trans., 2015.

Since this concept for the stabilization of the antiferroelectric phase appeared to be promising it is transferred in this study to other material systems.

2.1.1 Transformation of the Concept to other Material Systems

2.1.1.1 Bismuth Ytterbium (BY)

As already known Bi^{3+} resembles Pb^{2+} in many ways. The similarities are perceived in their electronic structure and in the polarizability caused by the stereochemically active $6s^2$ orbital. For that reason $BiYbO_3$, which was investigated as a component of relaxor dielectrics[6], [16], is chosen and is substituted on the A-site with the isovalent ion La^{3+}, which is well-known to stabilize the antiferroelectric phase.[5] Again $CaZrO_3$ and $SrZrO_3$ are used as dopants for the formation of solid solutions.

In Figure 3 the relationship between t versus X for the BY-system is illustrated, where it can be seen that the substitution of BY with Lanthanum leads to lower t-values, whereas the other dopants at the A- and B-site lead to an increase of the t-factor. Here is the challenge located in the ionic radius of the B-site cations. To reduce the tolerance factor of the system larger dopants on the B-site are required. In contrast, all samples of the BY-system exhibit an increase in the electronegativity difference with higher concentrations of dopants. Since Ca^{2+} and Sr^{2+} possess the identical electronegativity value, an equivalent X value is established for both systems at a defined doping level x.[4]

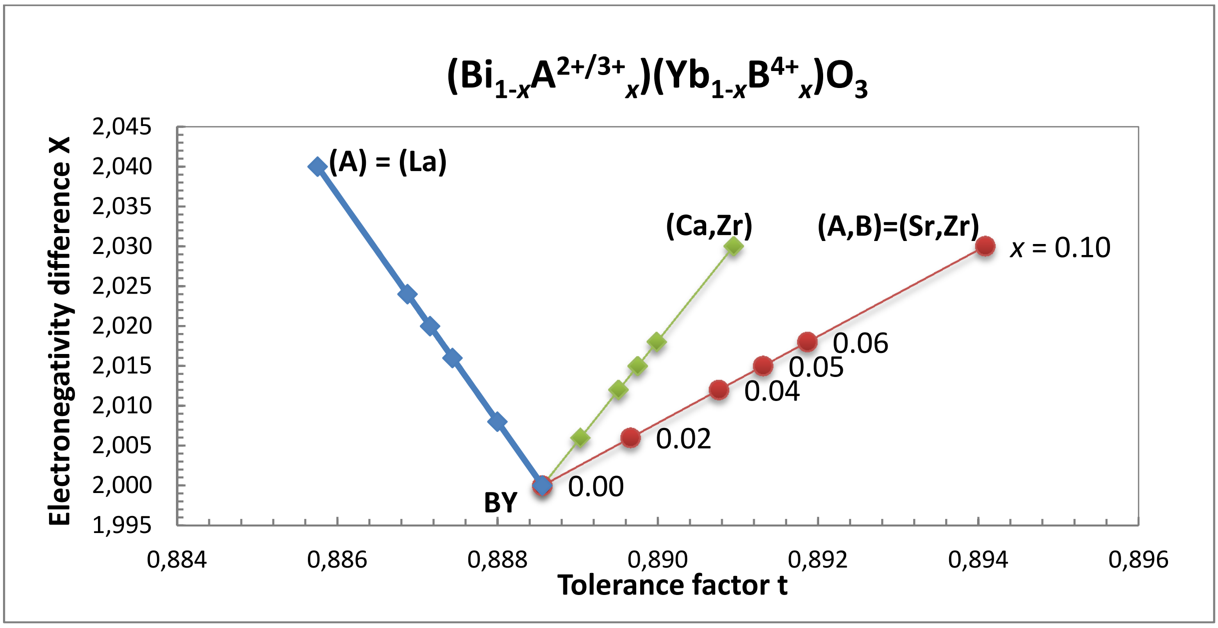

Figure 3: Tolerance factor versus electronegativity difference of $BiYbO_3$ with different substitutions at the A- and B-site.

2.1.1.2 Calcium Zirconate (CZ) and Strontium Zirconate (SZ)

In this case, on the one hand $CaZrO_3$ and on the other hand $SrZrO_3$ are chosen as base material. These systems are substituted on the A-site with the aliovalent ion La^{3+} and on the B-site with the ion Yb^{3+}. Figure 4 again shows the coherence between *t* and *X* for the CZ- and SZ-based ceramics. Finally, it can be said that the La^{3+}- and Yb^{3+}-substitution leads to a decrease in the tolerance factor in both systems and an increase in the electronegativity difference. Compared with the BY-system the CZ- and SZ systems show higher values for *t* and *X*.

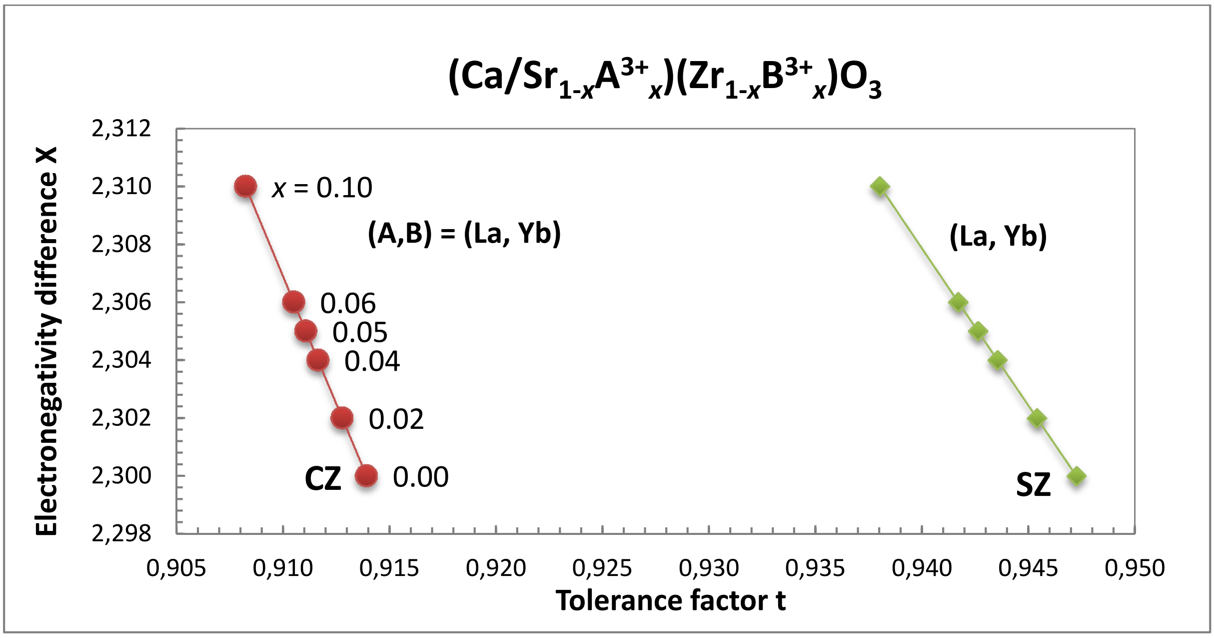

Figure 4: Tolerance factor t versus electronegativity difference X of $CaZrO_3$ and $SrZrO_3$, where (A, B) designates (La, Yb).

2.2 The Perovskite Structure

The perovskite crystal structure with the general formula ABO_3 is that of many ferroelectric oxides. The name of the structure is derived from the mineral $CaTiO_3$. However the structure itself was found and described by Goldschmidt in 1926.[17], [18], [19]

One possible view is a face centered cubic unit cell with three different atomic positions, shown in Figure 5. In the corners the 12-fold coordinated A-site is occupied by common metal ions with an ionic radius >1 Å, a similar size of the oxygen anions. The B-site, which is placed in the center is preferrably occupied by metal ions with an ionic radius <1 Å. This centre ion is coordinated by six oxygen ions in an octahedral configuration, which are placed at the face centers of the cube.

Additionally it is important to maintain charge neutrality in the structure. Therefore the compensation mechanisms for donor and acceptor dopants have to be considered.[18]

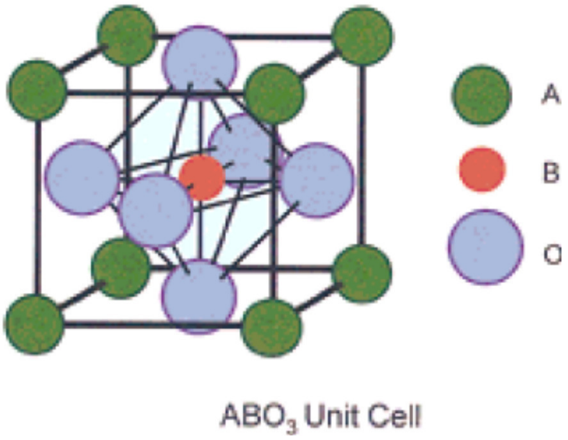

Figure 5: Schematic representation of the perovskite unit cell.[18]

2.2.1 Goldschmidt Tolerance Factor

In an ideal cubic perovskite, the relation between the ionic radii of A- and B-site cations as well as the anion radius is described by Equation 1:

$$r_A + r_O = \sqrt{2}\,(r_B + r_O)$$

Equation 1: Relationship of the radii on the A- and B-site of a cubic perovskite structure. (r_A…ionic radius of the A-site cation, r_B…ionic radius of B-site cation, r_O…ionic radius of oxygen) [1]

In order to determine the stability of perovskite crystals the so-called Goldschmidt tolerance factor *t* is introduced (Equation 2). For an ideal cubic perovskite t equals to one. A reduction in the size of the A-cation and an increase in the size of the B-cation lead to a reduction of this factor. Acceptable values for the perovskite structure are located in the range between 0.8 and 1.0. Lower or higher values of tolerance factor lead to typically instable perovskite crystals. For example, values higher than one leads to a hexagonal crystal structure, whereas a factor smaller than one leads to an orthorhombic, tetragonal or rhombohedral crystal structure.[20], [21]

$$t = \frac{(r_A + r_O)}{\sqrt{2}\,(r_B + r_O)}$$

Equation 2: Calculation of the Goldschmidt tolerance factor *t*.[20]

2.2.2 Shannon Ionic Radii

The following Table 1 represents a summarization of the ions with their corresponding ionic radii, which are used in this thesis. In 1976 these values were released by Shannon and are used many times in literature for the estimation of the Goldschmidt´s tolerance factor.[22], [19]

Table 1: Ions with varied coordination number inclusive their dedicated ionic radii and their average electronegativities.[22], [23]

Ion	Site occupation	Coordination number	Ionic radius [Å]	Average Electronegativities
Na^+	A	XII	1.39	0.9
Ca^{2+}	A	XII	1.34	1.0
Sr^{2+}	A	XII	1.44	1.0
Bi^{3+}	A	XII	1.45*	1.9
La^{3+}	A	XII	1.36	1.1
Yb^{3+}	B	VI	0.868	1.2
Zr^{4+}	B	VI	0.72	1.4
Nb^{5+}	B	VI	0.64	1.6
O^{2-}	O	VI	1.4	3.5

*) The value for Bismuth is linearly extrapolated from literature data for other coordination numbers.[22]

2.2.3 Electronegativity Difference

Table 1 also contains the data about the average electronegativities, which are used for the calculation of electronegativity difference according to the formula below (Equation 3). Besides the ionic bonds, the electronegativity difference is also an indicator for the amount of covalent bonds in the crystal structure. The lower the difference the higher is the amount of covalent bonding, which in addition to the Coulomb forces of ionic bonding stabilizes the crystal lattice.

$$X = \frac{(X_{AO} + X_{BO})}{2}$$

Equation 3: Calculation of the average electronegativity difference X (X_{AO}… electronegativity difference between the A cation and the oxygen anion, X_{BO}… electronegativity difference between the B cation and the oxygen anion).[4]

2.3 Defect Chemistry

This part describes all defects with respect to the NN material including the used dopants. Caused by disturbances in the real crystal lattice defects occur which also affect the electrical properties.[24] These defects are divided into:

0-dimensional defects:

Point defects are formed by missing, substituted or excess ions or electrons.

1-dimensional defects:

Line defects are induced by dislocations in the crystal lattice and can have an influence on (especially ionic) charge transport in the lattice.

2-dimensional defects:

As surface defects boundary surfaces (surfaces as external interfaces and in particular grain boundaries as internal interfaces) have a large influence on the conductivity of ceramics.

In crystalline oxides numerous reasons lead to deviations from the ideal stoichiometry and to the formation of point defects. For instance these defects can be placed through non stoichiometry or dopants and are subordinated thermodynamically equilibriums reactions and the kinetic.

For the description of the point defects related to the ideally occupied lattice the Kröger-Vink-notation is used. Besides the Kröger-Vink-notation the electron neutrality, the space ratio of cation and anion and the conservation of the mass has to be kept in mind.

Table 2: Kröger Vink notation for ionic point defects in a binary oxide MO. The Indices **x**, ´ and • characterize the neutral, negative and positive charge.

Symbol	Definition
M_M	Metal cation M^{2+} on a regular lattice site
O_O	Oxygen ion O^{2-} on a regular lattice site
V_M^X, $V_M^{´}$, $V_M^{``}$	neutral, simply negative and doubly negative cation vacancy
V_O^X, $V_O^{\bullet}$, $V_O^{\bullet\bullet}$	neutral, simple positive and doubly positive anion vacancy
M_i^x, $M_i^{\bullet}$, $M_i^{\bullet\bullet}$	neutral, simple positive and doubly positive interstitial cation
O_i^x, $O_i^{´}$, $O_i^{´´}$	neutral, simply negative and doubly negative interstitial anion

2.3.1 Intrinsic Defects

Point defects are developed in the thermodynamic equilibrium at higher temperatures (T). Thereby the entropy (ΔS) increases and the free enthalpy (ΔH) is reduced as presented through the equation:

$$\Delta G = \Delta H - T\Delta S$$

Equation 4: Equilibria of the Gibbs free energy ΔG.

There are two types of intrinsic defects:

1. Schottky defects
2. Frenkel defects

The *Schottky defects* corresponds to the assembly of anion and cation vacancies according to Equation 5. The ions are attached on the crystal surface under expansion of the lattice. Typically this kind of defect is find in close-packed lattices.

$$M_M + O_O \leftrightarrow V_M^{´´} + V_O^{\bullet\bullet} + MO$$

Equation 5: Schottky defect in a binary oxide.

For the NN system the following model is most preferred. Sodium oxide is shifting to the surface (Equation 6) and evaporates due to its low boiling point leaving sodium and oxygen vacancies in the lattice. A Sodium deficiency usually is prevented by a minor excess in the powder mixture.

$$2Na_{Na} + O_O \leftrightarrow V_{Na}^{''} + V_O^{\bullet\bullet} + Na_2O$$

Equation 6: NN specific Schottky defect.

The *Frenkel defects* can be seen in relatively open crystal structures. This occurs when an ion leaves its regular lattice site and occupies an interstitial site (Equation 7).

$$M_M \leftrightarrow V_M^{''} + M_i^{\bullet\bullet}$$

$$O_O \leftrightarrow V_O^{\bullet\bullet} + O_i^{''}$$

Equation 7: Frenkel defect in a binary oxide for cation and anion interstitial site.

In NN, Niobium is chosen as it has the lowest radius, but the concentration of Nb-interstitials is regarded as neglectable (Equation 8).

$$Nb_{Nb} \leftrightarrow V_{Nb}^{'''''} + Nb_i^{\bullet\bullet\bullet\bullet\bullet}$$

Equation 8: NN specific Frenkel defect.

2.3.2 Extrinsic Defects

Another way to get point defects are substituents in the material. These substituents may be added purposely as dopants to gain the desired properties of the material or occur as inevitable impurities.

2.3.2.1 Acceptor Doping

Negatively charged doping agents are called acceptors. These can be compensated through the formation of oxygen vacancies, interstitial cations or holes.

In Sodium Niobate Zirconium is considered as acceptor dopant because of substituting Nb (Equation 9).

$$ZrO_2 \leftrightarrow Zr_{Nb}^{'} + 2O_O + \frac{1}{2}V_O^{\bullet\bullet}$$

Equation 9: NN specific acceptor doping.

2.3.2.2 Donor Doping

Donors refer to the positively charged doping ions. They are compensated by cation vacancies, interstitial oxygen ions or electrons.

In this work Calcium is used as donor because of substituting Na (Equation 10).

$$CaO \leftrightarrow Ca_{Na}^{\bullet} + O_O + V_{Na}^{'}$$

Equation 10: NN specific donor doping.

2.3.2.3 Compensating Dopants

This type of dopants vary in the valency from the element, which is substituted. This can be either an addition of acceptors or donors in the material. To get averagely the identical oxidation state as the base cation these two different dopants have to balance each other. Thus no vacancies or electrons are formed.

In the prepared material Zirconium and Calcium compensate their function as acceptor and donor.

$$ZrO_2 + CaO \leftrightarrow Zr_{Nb}^{'} + Ca_{Na}^{\bullet} + 3O_O$$

Equation 11: Specific acceptor donor neutralization in NN.

2.3.2.4 Isovalent Dopants

Isovalent dopants change not in the valency from the ion they are replacing, but in their atomic weight and ionic radius. In addition the dopants do not incorporate vacancies of any form into the material. Therefore this procedure leads to a stoichiometrically fully occupied perovskite formation.

Another considerable example in this thesis is the substitution of the rare earth element La^{3+} with Bi^{3+}.

$$La_2O_3 \leftrightarrow 2La_{Bi} + 3O_o$$

Equation 12: BY specific isovalent doping.

2.3.2.5 Oxygen Partial Pressure

Moreover the defect chemistry can also be influenced by the oxygen partial pressure. Consequently the oxygen deficit can lead to oxygen vacancies or interstitial cations.

$$O_O \leftrightarrow \frac{1}{2} O_2\,(g) + V_O^{\bullet\bullet} + 2e^-$$

Equation 13: Development of oxygen vacancies and free electrons through an oxygen deficit.

By reason of oxygen excess oxides can shift to cation vacancies or oxygen ions can shift to interstitial sites. The resulting holes are in some cases balanced by cations.

2.4 Dielectric Properties

The dielectric properties are represented through physical equations. Only a choice of parameters, which are necessary for the interpretation of the results will be explained.[25], [24]

The dielectric displacement (*δx*) of an ion in the lattice leads to a generation of a dipole moment (p_i). The intensity depends on the degree of the change in position as well as on the charge (q_i) of the ion (Equation 14).

$$\overrightarrow{p_i} = q_i \cdot \delta\vec{x}$$

Equation 14: Dipole moment p_i.

As displayed in Equation 15, the polarization yields from the total of dipole moments in the elementary cell. Accordingly a definite relative permittivity ε_r and capacitance C of the material result.

$$\vec{P} = \sum_n \overrightarrow{p_i}$$

Equation 15: Polarization P is equal to the sum of dipole moments.

Through the concentration *c* = *n/V* of the dipoles, the density of the dipole moments gives the polarization. This factor differs with the concentration of the dipoles and is strongly addicted to the material. As shown in Equation 17, the electric polarization can be expressed as a function of an applied external field $\vec{E}$ by inserting the electric susceptibility χ (Equation 16).

$$\chi = \varepsilon_r - 1$$

Equation 16: Electric susceptibility χ (ε_r…relative permittivity).

$$\vec{P} = c \cdot \overrightarrow{p_i} = \chi \cdot \varepsilon_0 \cdot \vec{E}$$

Equation 17: Polarization P (ε_0...dieelectric constant, χ...electric susceptibilitiy, $\vec{E}$... electric field).

The relative permittivity is another important factor, which depicts the power of energy storing in contrast to the vacuum with its permittivity ε_0. The coherence of the dielectric polarization $\vec{P}$ and the electrical field $\vec{E}$ is seen in Equation 18. If this parameter cannot be evaluated directly at high field measurement, the following Equation 18 is very helpful.

$$\varepsilon_r = \frac{\vec{P}}{\varepsilon_0 \cdot \vec{E}} + 1$$

Equation 18: relative permittivity ε_r.

The geometry of the constructing component as well as the relative permittivity maintain the capacity C. Furthermore a high permittivity, a great area of the electrodes and little distances between the electrodes leads to a rise of the capacity.

$$C = \varepsilon_0 \varepsilon_r \frac{A}{d} (n-1)$$

Equation 19: capacity C of a plate capacitor (A…area of the electrodes, d…thickness of the component, n…number of electrodes (the n-1 term is insignificant inside a plate capacitor).

The conductance refers to the loss factor tanδ which is relevant in the dielectric measurement. The conductivity in a circuit is described through the ohmic resistor (R), which is responsible for the thermal loss in a capacitor. To prevent such capacity changes caused by temperature changes, the loss factor has to be minimized.

In Equation 20 the loss factor tanδ is expressed by the ratio of the real to the imaginary part of an alternating current with the circular frequency ω.

$$tan\delta = \frac{1}{\omega \cdot R \cdot C}$$

Equation 20: loss factor tanδ (ω…circular frequency, R...ohmic resistor).

2.5 Polarization Mechanism

In this chapter different types of dielectric polarization mechanisms are discussed. The four mechanisms are classified into electronic, ionic, orientation and space charge polarization.[25], [24]

Electronic Polarization

This kind of polarization originates on the displacement of the electron shell (negatively charged) against the atomic nucleus (positively charged) in the electric field, thereby a dipole is induced. It is found in all dielectric materials. The deflection from the equilibrium position is very small, however it is largely temperature-independent.

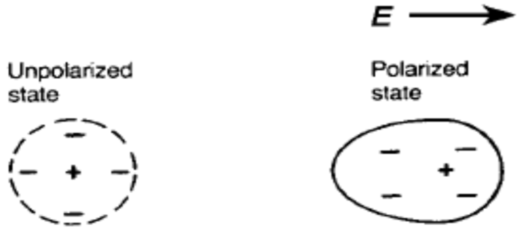

Figure 6: Electronic polarization, which causes the displacement of nucleus and shell. Left: unpolarized state and right polarized state.[1]

Ionic Polarization

As the name suggests, it appears in ionic materials and thus in all oxide dielectrics. The polarization in the electric field is induced by the displacement of the positive and negative ions.

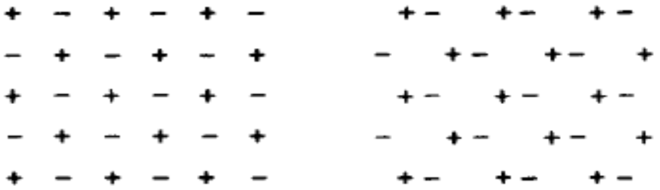

Figure 7: Ionic polarization, which shows the movement of positive and negative charged ions by an electric field which induces dipoles. Left: unpolarized state and right polarized state.[1]

Orientation Polarization

In many substances there are building blocks which have a permanent dipole moment. These can be polar molecules or associates of moving, reciprocally charged point defects in the crystal lattice. Based on the random directional arrangement which is caused by the thermal movement all dipole moments compensate. When an electrical field is applied, a preferential direction for the dipoles is induced and thus an orientation polarization.

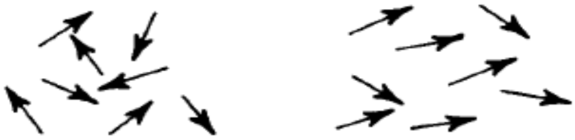

Figure 8: Orientation polarization, which displays the orientation of permanent dipoles. Left: unpoled state and right poled state.[1]

Space charge Polarization

By applying an electrical field in materials with conductivity inhomogenities free charge carriers are moving along many lattice distances and gather at interfaces between the conductive and the isolating region. Thus a space charge polarization is induced. Large differences in the local conductivity occur sometimes in oxide ceramics between the grain interior and grain boundary region.

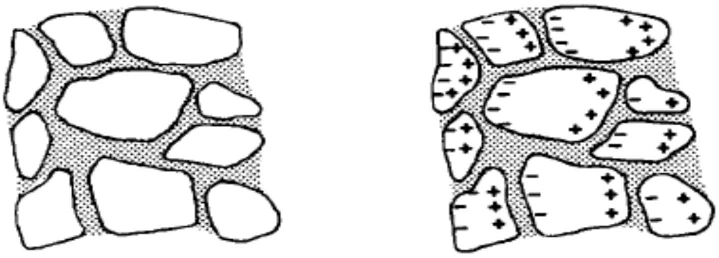

Figure 9: Space charge orientation, which visualizes the free charge carriers at the grain boundary. Left: unpolarized state and right polarized state.[1]

2.6 Polar Oxides and Charge Storage in Dielectric Materials

2.6.1 Polar Oxides

Crystals are categorized into 32 symmetry point groups which are split in seven fundamental crystal systems. These systems are specified as triclinic, monoclinic, orthorhombic, tetragonal, rhombohedral, hexagonal and cubic. Additionally they are divided into 21 non-centrosymmetric and 11 centrosymmetric point groups. 20 of the former point groups do not possess an inversion centre and thus piezoelectric effects can be appear. That is the reason why polarization under mechanical stress can occur.[25], [1], [24], [27], [28]

Moreover there are 10 groups of these non-centrosymmetric crystal systems, which reveal a permanent polar axis along a specific spatial direction. This group of material is called pyroelectric since their polarization strongly depends on the temperature. However this polarisation is not long-lasting and disappears at constant temperature.
An additional subcategory of the piezoelectric and pyroelectric materials are the ferroelectrics that can be seen in the figure beneath. Related to pyroelectrics, ferroelectrics also feature a permanent polar axis, which can change the direction of the spontaneous polarization through an applied external electric field.

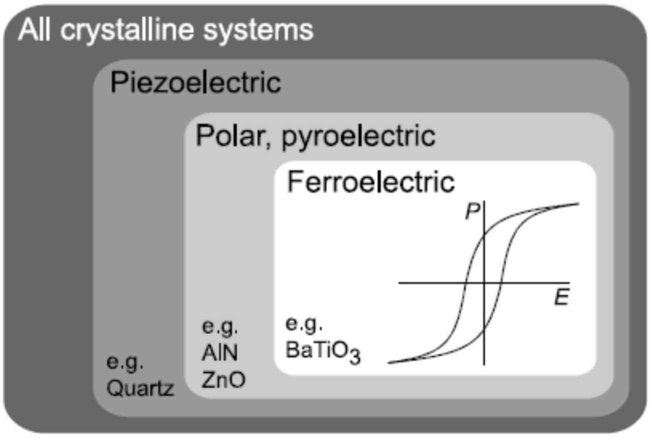

Figure 10: Categorization of the different crystal systems by their electrical properties.[25]

The insertion in Figure 10 shows a hysteresis loop, which is characteristic for ferroelectric materials. It will be discussed into detail in the next chapter.

2.6.2 Charge Storage in Dielectric Materials

As dielectrics several electrically isolating materials come into consideration. The different types of dielectrics are classified into paraelectrics, antiferroelectrics, ferroelectrics and relaxor ferroelectrics. The relationship between the electric field (E) and the polarization (P) of the different types is shown in Figure 11. In this part the properties as well as the dissimilarities will be covered.[25], [26], [1], [24]

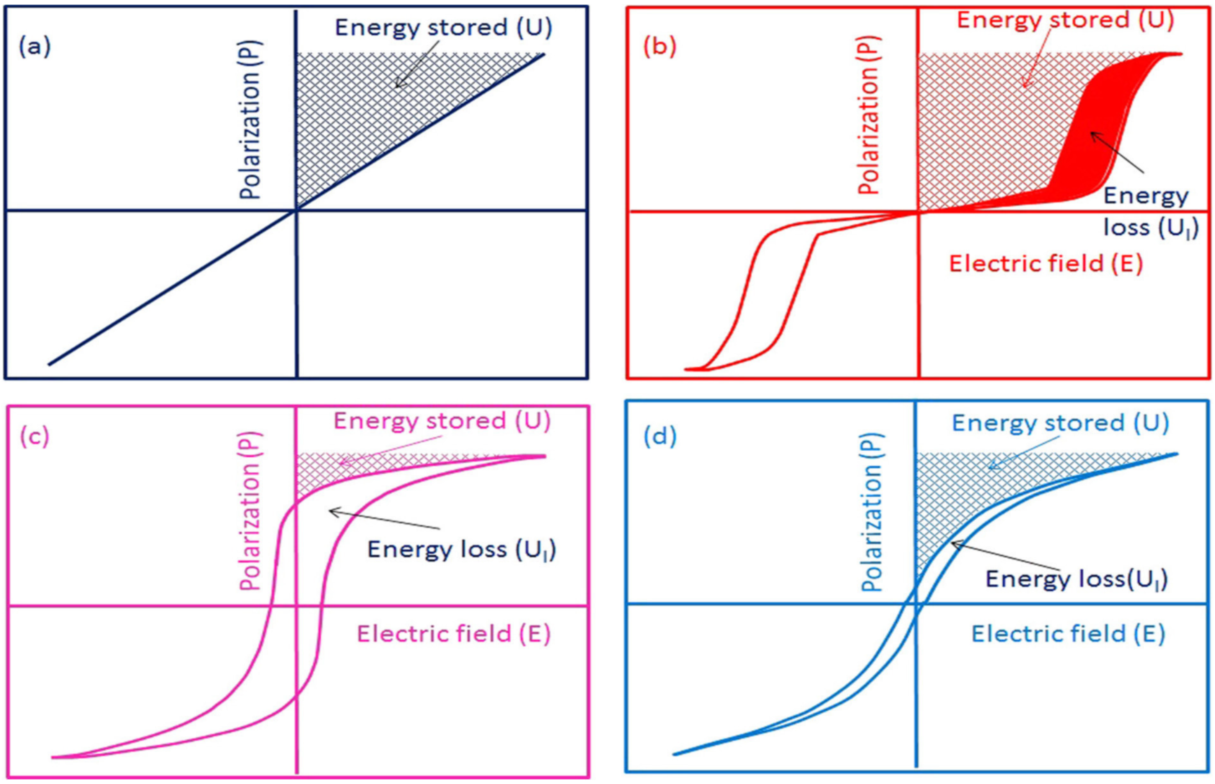

Figure 11: Differentiation of paraelectric (dark blue), antiferroelectric (red), ferroelectric (pink) and relaxor ferroelectric (light blue) behaviour by the polarization vs. electric field. Picture taken from Patel et al. Materials Research Express, 2014.

2.6.2.1 Paraelectrics

If an electrical field is applied on paraelectric materials, dipoles are induced. These dipoles of the material become aligned and the external field is degraded. Once the electrical field is removed, the dielectric polarization also disappears and a linear relationship between electric field and polarization is seen in Figure 11a.

Designated in Figure 11 the cross-hatched area in the diagram indicates the energy stored in the material. But in this case the area can only be increased by increasing the electric field.

2.6.2.2 Ferroelectrics

As mentioned in chapter 2.6.1 ferroelectric materials contain spontaneously generated dipoles, which can be changed in direction by an external electric field and exhibit a characteristic hysteresis curve, which is shown in Figure 11c. These materials possess sections in which the polarization has the same direction as well as the same strength. These sections are called domains. In addition they are separated through domain walls from regions where the polarization has a different orientation.

The polarization is increased by applying an electrical field where the dipoles align in one direction at a certain field strength. This leads to a maximum of polarization, which is the so-called saturation polarization. By decreasing the field to zero, the orientation of the dipoles is maintained to a great extent and a remnant polarization can be measured. By reversing the direction of the electric field, the directions of the dipoles is gradually reversed. At a definite field, the so-called coercive field, the net polarization is zero. In ferroelectrics this hysteretic behaviour leads to an energy loss, which is equivalent to the area in the hysteresis loop. It is commonly converted into heat.
Additionally the shaded area in Figure 11c displays the stored energy.

2.6.2.3 Relaxor Ferroelectrics

This kind of materials exhibit a hysteresis loop, too, but with a coercive field, which is nearly zero. The energy storage capacity is higher and the energy loss is lower compared to ferroelectrics (Figure 11d).

2.6.2.4 Antiferroelectrics

In contrast to the ferroelectric materials the alignment of the switchable dipoles in the unit cell of antiferroelectrics is antiparallel, which leads to a net zero polarization at zero field. As seen in the figure above the linear behaviour at low electrical field develops only a small amount of polarization until a certain electric field is reached. At the so called forward switching field the dipoles are constrained to align in parallel and furthermore a ferroelectric loop is triggered.

This transition is reversible when the electric field is decreased and the ferroelectric state disappears. That is observed when the limiting value of the electrical field, called backward switching field, is reached and so the material returns to its antiferroelectric

state. The polarization is reduced further to zero at zero electric field. In Figure 11b the characteristic double-hysteresis curve is shown.
Again the embedded area within the double hysteresis is equivalent to the energy loss, which is mostly transferred into heat.

On the other hand antiferroelectric materials show the largest energy storage capacity and thus these materials are ideal for high energy storage capacitors. To increase the stored energy and to tailor the polarization curves many parameters can be used to influence this material. By raising both maximum polarization and the strength of the switching fields, the hatched area can be increased. In addition this could be affected by the difference of both switching fields, which should be retained little to inhibit losses. The best performance is attained by a small polarization curve as it offsets to high electric fields and amplifies the polarization.

3 Experimental

The following chapter presents the preparation and characterization of the samples in this thesis. Initially the calculation of the tolerance factor versus the electronegativity difference is done in order to achieve an overview of possible candidates for the preparation of lead-free dielectrics. In the next step the ceramics are synthesized and the structural and dielectric characteristics are measured in detail.

In Figure 12 the tolerance factor and electronegativity difference for diverse perovskites, comprising an extensive range of complex and simple ones are displayed. The materials used in this study are highlighted in green.

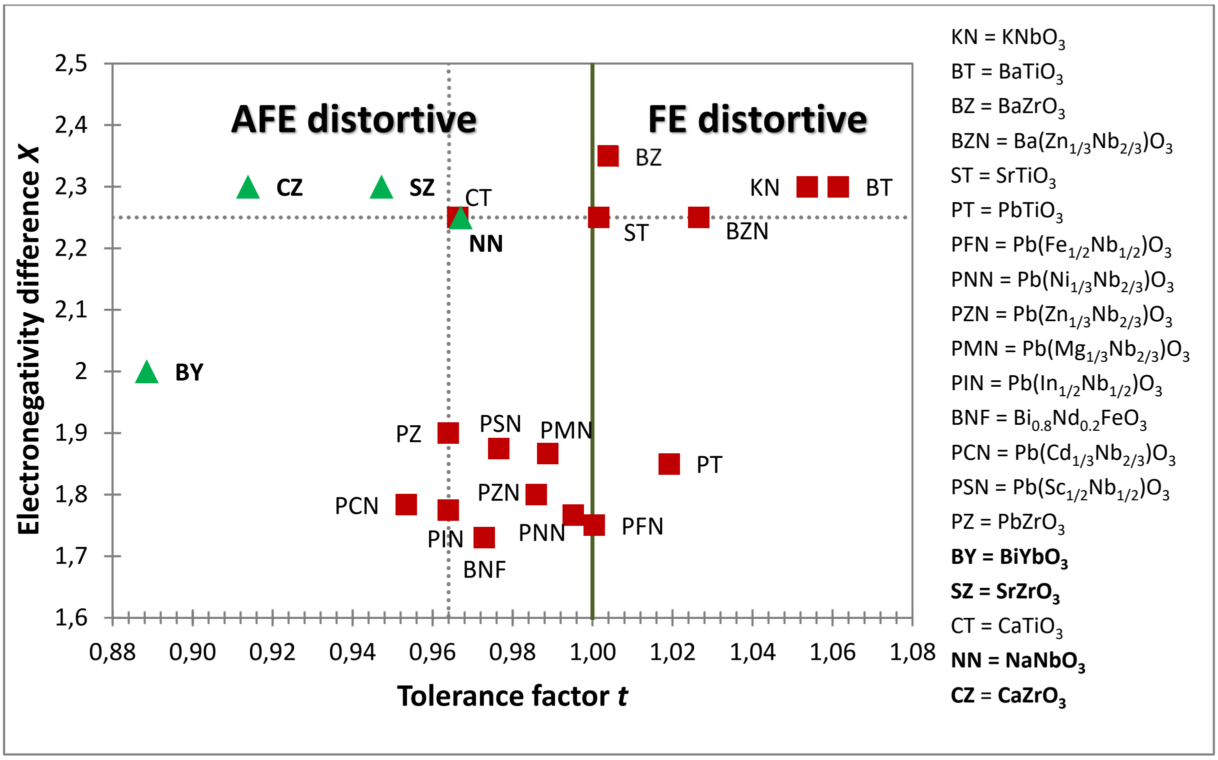

Figure 12: Tolerance factor *t* versus averaged electronegativity difference *X* for diverse perovskites. The horizontal dotted line shows the *X* for $SrTiO_3$. The vertical dotted line shows the *t*-factor for $PbZrO_3$.

At first the substitution of NN with Calcium and Zirconium from literature is verified and then it is transferred to the other material systems. A list of samples which are produced by the conventional solid state method can be found in Table 3.

Table 3: Samples under investigation including their abbreviations.

Samples	Abbreviation
$NaNbO_3$	CZNN0
$Na_{0.98}Ca_{0.02}Nb_{0.98}Zr_{0.02}O_3$	CZNN2
$Na_{0.96}Ca_{0.04}Nb_{0.96}Zr_{0.04}O_3$	CZNN4
$Na_{0.90}Ca_{0.10}Nb_{0.90}Zr_{0.10}O_3$	CZNN10
$BiYbO_3$	BY
$Bi_{0.90}La_{0.10}YbO_3$	LBY10
$Bi_{0.98}Sr_{0.02}Yb_{0.98}Zr_{0.02}O_3$	SZBY2
$Bi_{0.90}Sr_{0.10}Yb_{0.90}Zr_{0.10}O_3$	SZBY10
$Bi_{0.98}Ca_{0.02}Yb_{0.98}Zr_{0.02}O_3$	CZBY2
$Bi_{0.90}Ca_{0.10}Yb_{0.90}Zr_{0.10}O_3$	CZBY10
$Ca_{0.90}La_{0.10}Zr_{0.90}Yb_{0.10}O_3$	LYCZ10
$Sr_{0.90}La_{0.10}Zr_{0.90}Yb_{0.10}O_3$	LYSZ10

3.1 Powder Preparation

The ceramic powders are produced by the mixed metal oxide route. For that reason following powders are used as starting materials and listed in Table 4.

Table 4: Raw materials used for syntheses with information about their purity and CAS number.

Powder	Purity [%]	Manufacturer	CAS
$NaCO_3$	99.99	Merck	497-19-8
$CaCO_3$	99.0	Merck	471-34-1
$SrCO_3$	Reagent grade	Solvay Bario e Derivati, Massa, Italy	1633-05-2
Bi_2O_3	99.9	MCP-HEK GmbH, Lübeck, Germany	1304-76-3
La_2O_3	min. 99	Treibacher, Austria	1312-81-8
Nb_2O_5	99.9	H.C. Starck	1313-96-8
Yb_2O_3	99.9	Treibacher, Austria	1314-37-0
Yb_2O_3	99.99	Treibacher, Austria	1314-37-0
ZrO_2	Grade 15	MEL Chemicals, Manchester, UK	1314-23-4

The amount of the different starting compounds is calculated and weighted corresponding to Equation 21.

$$W_n = \frac{X_n \cdot Y_n}{Z_n} \cdot \frac{W_{ges}}{\sum_{i=1}^{n} \frac{X_i \cdot Y_i}{Z_i}} \qquad\qquad Z_n = \frac{x_{metal} \cdot M_{metal}}{M_{ges}}$$

Equation 21: Computation formula of the weighted ratio.

X_n	atomic weight of the educt [g/mol]
Y_n	proportion of the metal in the ceramic [g/g]
Z_n	metal content of the carbonate or the oxide [g/g]
W_n	net weight of the educt [g]
W_{ges}	amount of the raw materials [g]
x_{metal}	amount of the metal [ ]
M_{metal}	atomic weight of the metal [g/mol]
M_{ges}	atomic weight of the starting compound [g/mol]

Table 5: Calculation for $Na_{0.98}Ca_{0.02}Nb_{0.98}Zr_{0.02}O_3$.

W_{ges} = 25 g	Na_2CO_3	$CaCO_3$	Nb_2O_5	ZrO_2	
X_n [g/mol]	45.98	40.08	185.81	91.22	
Y_n [g/g]	0.98	0.02	0.98	0.02	
Z_n [g/g]	0.43	0.40	0.70	0.74	
$\frac{X_n \cdot Y_n}{Z_n}$	104.79	2.00	260.13	2.46	**∑= 369.38**
W_n [g]	7.092	0.135	17.606	0.167	

After weighing on an analytical balance (Acculab ALC-210.4) the mixture of raw material is homogenized in 50 g ethanol with a planetary mill (Fritsch Pulverisette 6) in 250 ml zirconia beakers with 250 g yttrium stabilized zirconia spheres 5 mm in diameter. This first milling is carried out for 1 hour with 400 rpm. Subsequently the resulting slurry is filtered to separate it from the milling medium and dried in the cabinet dryer (Heraeus T20) at 80 °C overnight, thus the ethanol is removed.

The calcination procedure is performed in a box furnace (Nabertherm C 290) at 1050 °C for 3 hours. For the heating and cooling rates 5 °C/min are chosen. In order to control the completion of the reaction X-ray diffraction (XRD) is done. In Figure 13 the temperature program for the calcination procedure is shown.

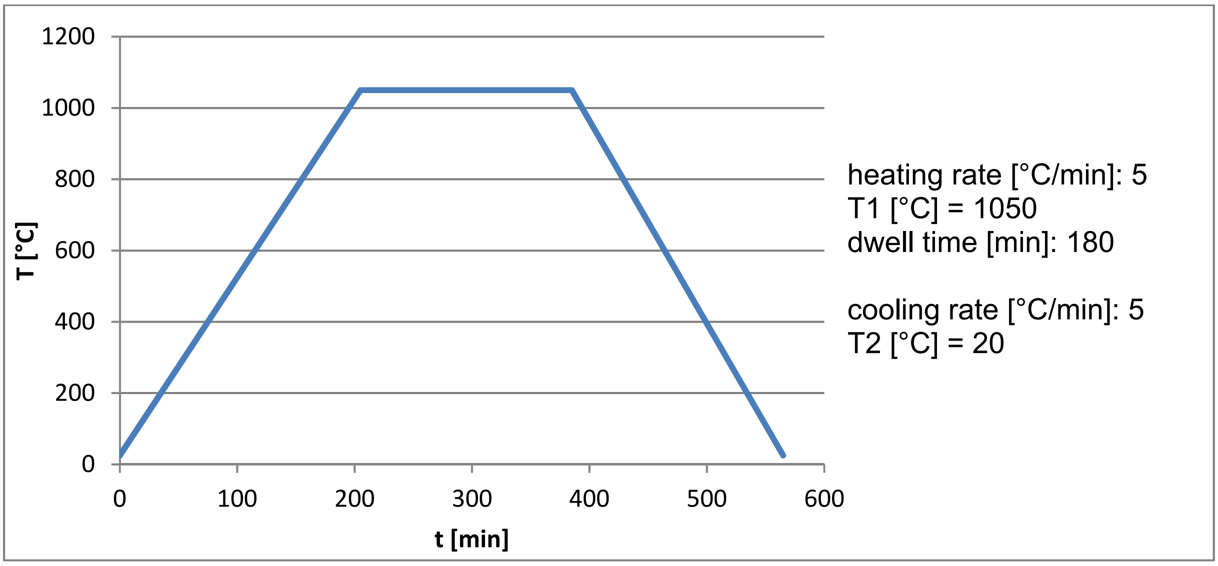

Figure 13: Temperature program for the calcination procedure.

Next the compounds are milled again. For this step the substance is milled with yttrium stabilized zirconia spheres with 2 mm in diameter for 1 hour with a lower speed of 300 rpm. Again ethanol is used as dispersion liquid and dried at 80 °C for 24 hours. This second milling is necessary to lower the particle size and crushing agglomerates.

After drying the fine particles are granulated by adding 1 gram binder solution (30 wt% polyethylene glycol PEG 20000) to 10 gram powder and dried in a drying oven at 80 °C for at least 10 minutes. This yields a binder content of 3 % PEG in the green compact. Before pressing into disc shaped samples the material is sieved with a mesh size of 315 µm and 180 µm. Subsequently the granulate is pressed with a maximum pressure of 150 MPa (2 tons) for 5 minutes into discs with a green body diameter of 13 mm and a height of around 1.20 - 1.40 mm.

Before removing the binder the density of the green bodies is determined geometrically through a calliper gauge and by weighing the pellets. The samples are then arranged in open alumina crucibles to support the pyrolysis of the binder to H_2O and CO_2. Zirconia sand is used to avoid that the pellets stick together. The temperature program depicted in Figure 14 is chosen for the debindering procedure in a box furnace (Nabertherm C 290).

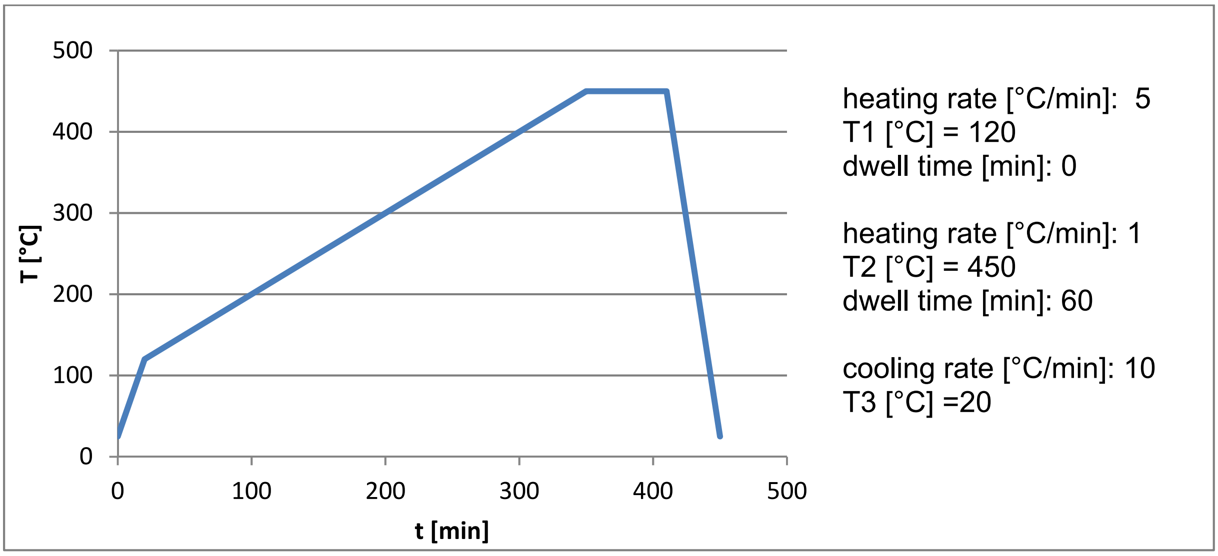

Figure 14: Temperature program for the debindering procedure.

Finally the samples have to be sintered. The purpose is to reach dense samples without evaporation and decomposition of the components. Sintering is carried out under air atmosphere in closed alumina crucibles. Since there are varying compositions with different sintering temperatures three different temperature programs are applied. The sintering of both compositions CZNN and LYCZ/LYSZ is done at 1350 °C in a box furnace (Nabertherm HT 04/17). Also the heating and cooling rate of 10 °C/min is the same, only the duration of the dwell time is different (Figure 15). As $BiYbO_3$ has a lower melting point than the other compositions a peak temperature of 890°C is chosen with a subsequent dwell time of 1200 min at 850 °C (Figure 16).

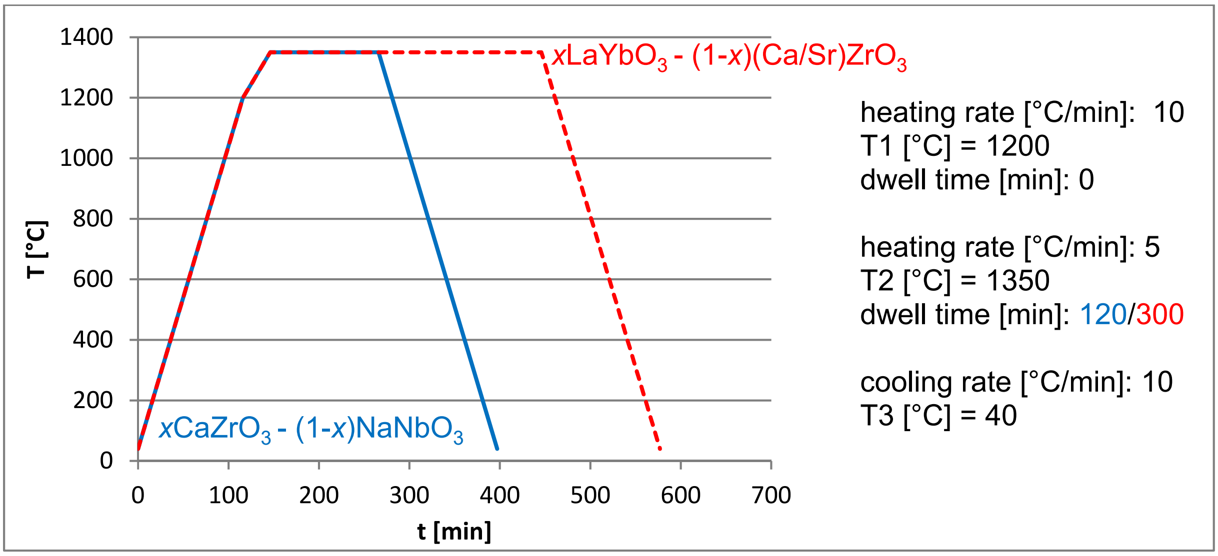

Figure 15: Temperature program for the sintering procedures of CZNN and LYCZ/LYSZ.

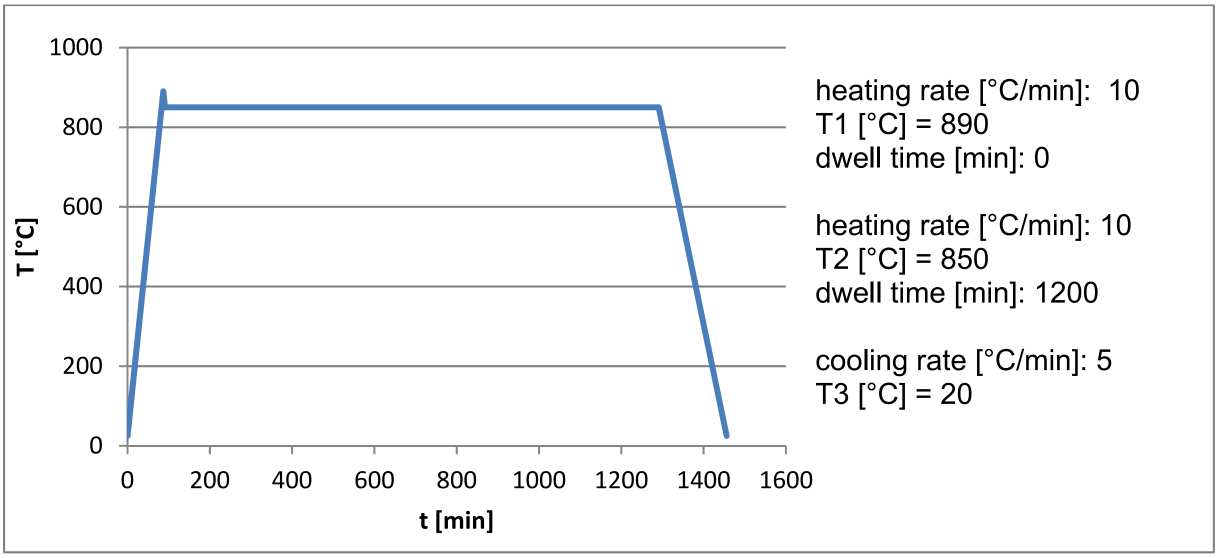

Figure 16: Temperature program for the sintering procedures of doped $BiYbO_3$.

After sintering the samples are measured with different techniques, which are described in chapter 3.2.

3.2 Sample Characterization

The following measurement techniques are used.

3.2.1 X-Ray Powder Diffraction

To acquire data about the phase composition and the lattice parameters calcined and sintered samples are analysed by XRD. Therefore the samples are ground in an agate mortar with a pestle to a fine powder. All samples are measured with a BRUKER D8 Advance diffractometer using Cu K_α radiation. With the help of Panalytics X'Pert High Score Plus and the ICSD database the spectra are analyzed and phases can be identified. The Rietveld refinement is done to provide the lattice constants for the calculation of the cell volume. Consequently the theoretical density of the samples is determined according to the formula.

$$\delta_{theo.} = \frac{n \cdot M}{V \cdot N}$$

$\delta_{theo.}$	theoretical density [g/cm^3]
n	number of formula units/unit cell [1]
M	atomic weight [g/mol]
V	volume of unit cell [Å^3]
N	Avogadro's number [$6.022 \cdot 10^{23}$ atoms/mol]

3.2.2 Density and Shrinkage Measurement

For the determination of the geometric density the pellets are measured prior to and after sintering. Accordingly the thickness as well as the diameter is obtained through a digital calliper rule (Workzone) and the weight of the pellets with an analytical balance (Acculab ALC-210.4). As second method for determining apparent density the Archimedes method (Mettler Toledo XS204 DeltaRange) is used.
Moreover the theoretical density is calculated by the lattice parameters through X-ray diffraction. The ratio of the apparent density and the theoretical density yields the relative density. For measurement under high electric fields the relative density should be > 95 %.

To estimate the shrinkage during the sintering procedure the geometric data of the green body as well as the sintered sample are related. The values for the diameter shrinkage should be in the range between 14 and 16 %. The volume shrinkage should be located in a range of 35 – 40 % and the length shrinkage between 12 and 14 %. The higher the values for shrinkage, the better the densification.

3.2.3 Small Signal Electrical Measurement

Five pellets of each sample are polished and covered with silver paste (Leitsilber 200). Each side of the surface is dried for 10 minutes at 80 °C and the excess of the paint at the sidewise surface is eliminated with a fine silicon carbide grinding paper (800 mesh). Subsequently the capacity C and the dielectric loss factor tan δ (Hewlett-Packard 4192A LF Analyzer) are determined at an amplitude of 1 V sine with different frequencies from 1 kHz, 10 kHz and 100 kHz at room temperature. Higher frequencies of 10 kHz and 100 kHz are used, if the metering range of the capacity and the loss factor is not sufficient. To evaluate the permittivity ε_r the following equation of a plate capacitor is used for the calculation.

$$C = \varepsilon_r \varepsilon_0 \frac{A}{d}$$

C	capacitance [F]
ε_r	relative permittivity [for vacuum = 1]
ε_0	vacuum permittivity [$8.854 \cdot 10^{-12}$ F/m]
A	area of the capacitor [m^2]
d	thickness of the capacitor [m]

3.2.4 Hysteresis Loops

Before measuring, the samples are lapped to 300 µm, ground to a circular shape of 10 mm diameter and sputtered with a 0.3 µm Cr-Ni-Ag layer. For the recording of the polarization curves an aixACCT-aixPES piezoelectric evaluation system is used. The voltage is applied in the kV-range up to 7.2 kV with a frequency of 0.1 Hz (triangular shape) and at temperatures from 25 °C to 140 °C. Both the temperature and the amplitude are varied to achieve saturation in polarization. However some of the compositions exhibit a breakthrough voltage below saturation.

4 Results and Discussion

In this part the assessment of the three different sample series - is discussed in a detailed way.

4.1 Properties of xCaZrO$_3$ – (1-x)NaNbO$_3$

This chapter presents the comparison of the data from literature and the achieved data in this study. According to literature[4] the influence of the Ca^{2+}- and Zr^{4+}- substitution on $NaNbO_3$ leads to antiferroelectric polarization curves.

4.1.1 X-ray Diffraction

In Table 6 and Table 7 the space group, the lattice parameter as well as the cell volume of the calcinated and sintered samples are listed. For all samples an orthorhombic perovskite structure with different space group can be determined. The cell volume as well as the lattice parameters of the calcinated samples are increasing up to a substitution of 2 mol%. When the dopant concentration in the calcinated samples exceeds 4 mol% a secondary phase appears, which is identified as roughly 1 wt% zirconium oxide. This impurity is eventually a residue from the solid state synthesis. After sintering all samples are single phase perovskite and no ZrO_2 could be found. It is apparently incorporated in the crystal structure of the perovskite.

Table 6: List of the space group, the lattice parameters and the cell volume of the calcinated xCaZrO$_3$ – (1-x)NaNbO$_3$.

CALCINATED					
Sample	**Space group**	**a [Å]**	**b [Å]**	**c [Å]**	**Cell volume [Å^3]**
CZNN0	Pnma	5.5669	7.7655	5.086	238.14
CZNN2	Pbma	5.5680	15.5529	5.5091	477.08
CZNN4	Pnma	5.5666	7.7706	5.5076	238.23
CZNN10	Pnma	5.5637	7.7868	5.5101	238.71

Table 7: List of the space group, the lattice parameters and the cell volume of the composition xCaZrO$_3$ – (1-x)NaNbO$_3$ after sintering.

SINTERED					
Sample	**Space group**	**a [Å]**	**b [Å]**	**c [Å]**	**Cell volume [Å^3]**
CZNN0	Pbcm	5.5017	5.5632	15.5411	475.66
CZNN2	Pbma	5.5635	15.5502	5.50310	476.09
CZNN4	Pbcm	5.5078	5.5650	15.5706	477.25
CZNN10	Pbcm	5.5088	5.5656	15.5885	477.93

4.1.2 Densification and Shrinkage

In Table 8 the measured densities of the sintered samples are presented. The apparent and the relative density achieve the highest value with a content of x = 0.02. Except for the sample, which is doped with 10 mol% calcium and zirconium, all samples show a relative density above 95 % which indicates adequate densification for further characterization.

Table 8: List of the densities of xCaZrO$_3$ – (1-x)NaNbO$_3$.

Sample	**Theoretical density [g·cm^{-3}]**	**Archimedes' density [g·cm^{-3}]**	**Relative density [%]**
CZNN0	4.577	4.43	96.79
CZNN2	4.582	4.56	99.52
CZNN4	4.579	4.53	98.93
CZNN10	4.598	4.10	89.17

The same trend is observed in Figure 17 which shows the shrinkage after sintering. Up to a molar content of x = 0.02 the values are increasing and then with higher concentration they are deteriorated.

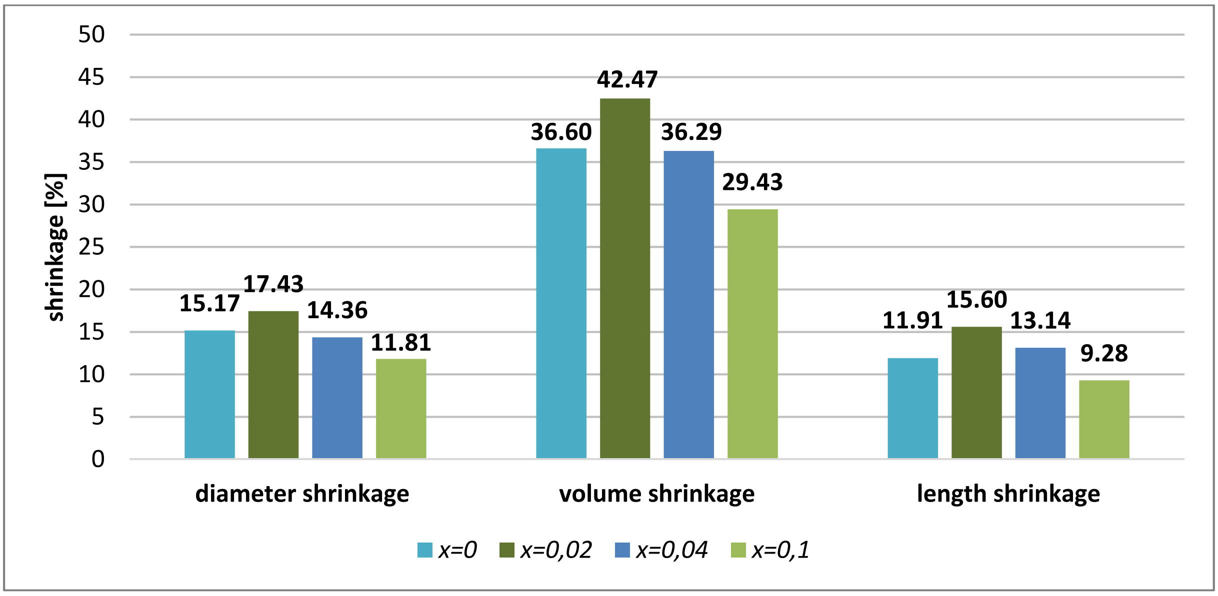

Figure 17: Shrinkage values of $x\text{CaZrO}_3 - (1\text{-}x)\text{NaNbO}_3$.

4.1.3 Small Signal Electrical Measurement

The small signal measurement is done at room temperature with a frequency of 1 kHz and a voltage of 1 V. In Table 9 the results of the small signal dielectric measurements are shown. By increasing the molar content of Ca^{2+} and Zr^{4+} from 0 to 4 mol% the capacitance shows a stable increase from 140 to 210 pF. Likewise the relative permittivity is growing over the same compositional range from 196 to 274. The loss factor declines with increasing dopant content. Interestingly, with the substitution of 2 mol% calcium and zirconium the loss factor is below the detection limit of the equipment. The decrease of relative permittivity and the increase of the loss factor with the substitution of 10 mol% calcium and zirconium is due to the insufficient densification of the sintered samples (see Table 8).

Table 9: Results of small signal electrical measurements of $x\text{CaZrO}_3 - (1\text{-}x)\text{NaNbO}_3$.

Sample	Capacitance [nF]	Loss factor []	Relative permittivity []
CZNN0	0.14	0.002	196
CZNN2	0.15	0	221
CZNN4	0.21	0.001	274
CZNN10	0.17	0.014	228

4.1.4 Hysteresis Loops

As seen in Figure 18 neither the sodium niobate nor the solid solutions with calcium zirconate exhibit at room temperature a ferroelectric or antiferroelectric behaviour. From the density data presented in Table 8 it is obvious that the sample with 10 mol% has not achieved sufficient density, therefore this sample was not considered for measurement. On the other samples only paraelectric polarization can be observed. Nevertheless with increasing substitution the breakthrough strength reaches higher values compared with literature.[4] Moreover it is obvious that the energy loss (area inside the loop) is also growing with higher substitution.

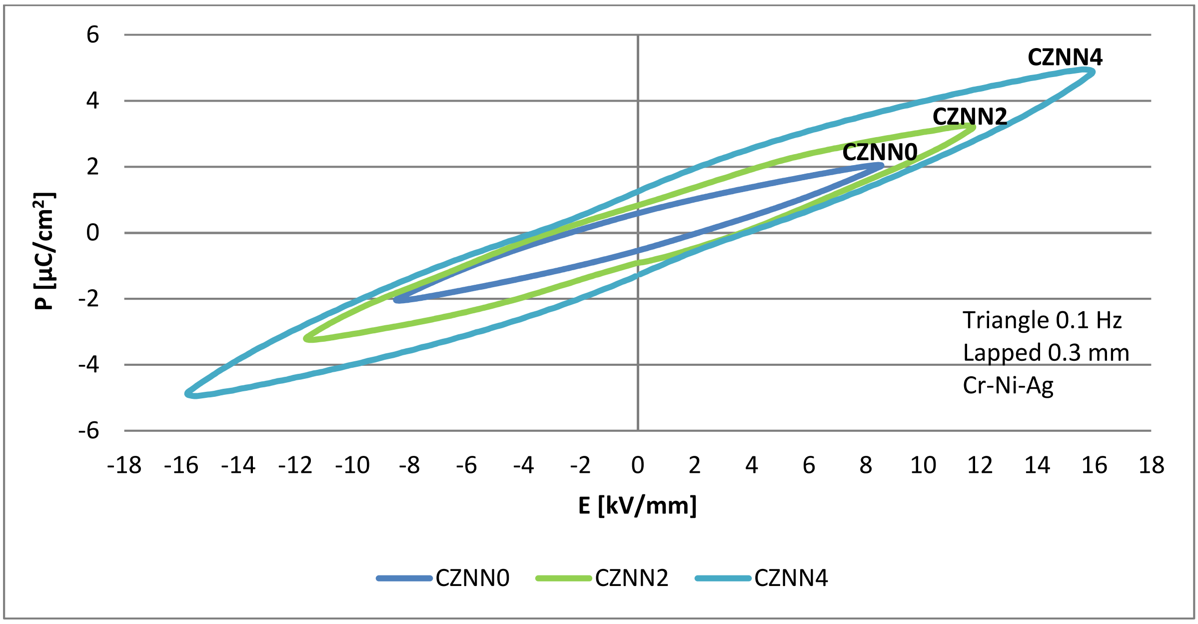

Figure 18: Polarization curves of different compositions of $x\mathrm{CaZrO_3} - (1\text{-}x)\mathrm{NaNbO_3}$ at 25°C.

Samples of CZNN4 are chosen for polarization measurements at elevated temperatures.

The measured ceramic shows again no antiferroelectric polarization at temperatures from 110 °C to 140 °C (Figure 19). Moreover, it can be observed that with higher temperatures the energy loss is rising which leads to a drop in charge storage capacity.

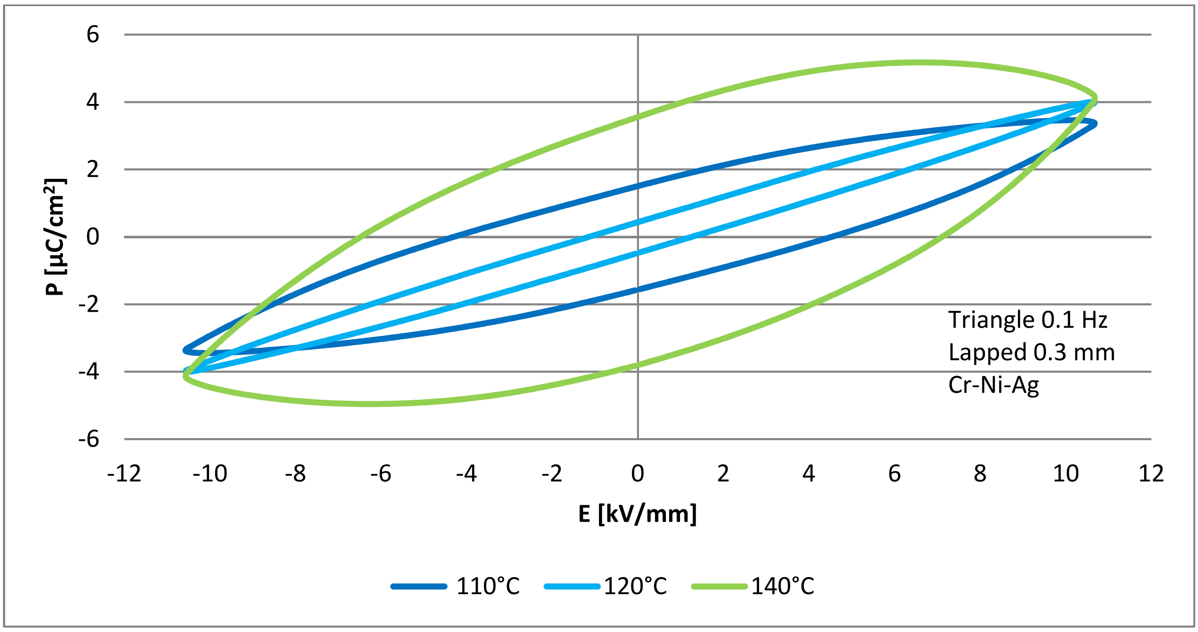

Figure 19: Polarization curves of $Na_{0.96}Ca_{0.04}Nb_{0.96}Zr_{0.04}O_3$ at various temperatures.

As shown in Figure 18 and Figure 19 the results from the publication of Shimizu et al. could not be reproduced.[4] Therefore we have communicated with the authors of the publication to find out what might be the reason for this discrepancy. Hanzheng Guo and Lisheng Gao advised not to grind the sintered pellets of approximately 1 mm thickness down to 0.3 mm by lapping with an aqueous suspension. Also they suggested not to apply electrodes by sputtering.

For that reason the thickness of the CZNN4 ceramic is unchanged and is just dry grinded to eliminate the residue of zirconia sand. The surface of the ceramic is covered with a silver paste (ÖGUSSA Leitsilber 200) and dried for 10 minutes at 80 °C. After that the sample is measured at room temperature and then the temperature is risen to 120°C. With increasing temperature the energy loss is also growing. The polarization values are very low and also the breakthrough voltage is not so high anymore due to the higher thickness of the sample. It can be summarized, that no improvement compared to the results shown in Figure 18 and Figure 19 can be seen in Figure 20.

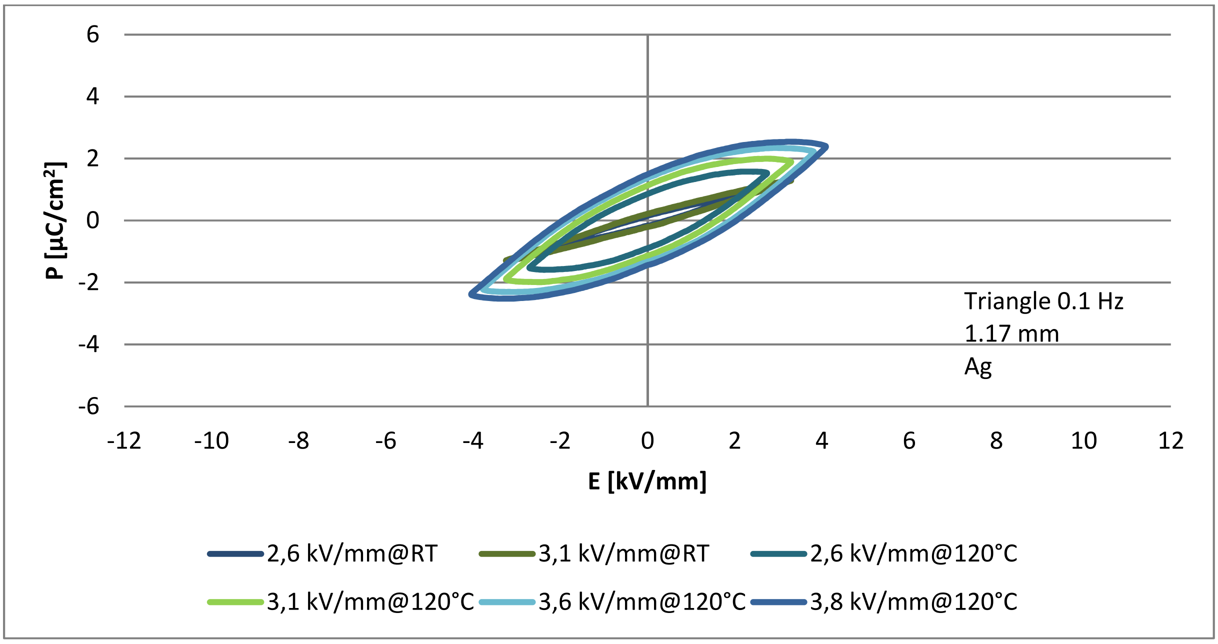

Figure 20: Polarization curves of $Na_{0.96}Ca_{0.04}Nb_{0.96}Zr_{0.04}O_3$ with different electrode variation at 25°C and 120°C.

4.2 Properties of *x*LaO_3 – (1-*x*)$BiYbO_3$, *x*$CaZrO_3$ – (1-*x*)$BiYbO_3$ and *x*$SrZrO_3$ – (1-*x*)$BiYbO_3$

In this section the focus is on the synthesis of $BiYbO_3$ doped with $CaZrO_3$, $SrZrO_3$ and La_2O_3. The samples are prepared in a similar way as described in chapter 4.1. Only the temperatures and the dwell time for the sintering process are different. The samples of doped $NaNbO_3$ are sintered with a dwell time of 120 minutes at 1350°C whereas the samples of doped $BiYbO_3$ are sintered at a peak temperature of 890 °C with a dwell time of 1200 minutes at 850 °C. Examination of the structure determination, density measurement and dielectric properties are discussed in this chapter.

4.2.1 X-ray Diffraction

The Rietveld refinement results from the XRD analysis of the doped $BiYbO_3$ are summarized for each sample in Table 10 to Table 15. All samples contain secondary phases, however a trend can be observed. Below a concentration of 10 mol% both the calcinated and the sintered sample contain a Bi-rich and a Bi-deficient phase. A concentration of 10 mol% leads to three or more phases after the calcination process. The sintered samples show again only two phases. Probably inevitable evaporation of Bi_2O_3 is the reason for the formation of two phases with different composition.

4.2.1.1 $BiYbO_3$

The results from the XRD measurement of the calcinated and the sintered $BiYbO_3$ are presented in Table 10. The analysis of both samples shows a phase with a small, cubic defect-fluorite cell and a secondary phase with a big, cubic cell which has a Yb_2O_3 structure. After sintering the cell volume is lower than just after calcination. Furthermore the fraction of the defect-fluorite increases and the Yb_2O_3 decreases after sintering.

Table 10: List of the phases, the structure type, the symmetry, the lattice parameters, the cell volume and the weight percent of the sample with nominal composition $BiYbO_3$ after calcination and sintering.

CALCINATED					
Phase	**Type of Structure**	**Symmetry**	**a [Å]**	**Cell volume [Å^3]**	**Wt%**
$(Yb,Bi)_2O_3$	Defect-fluorite	Cubic	5.4226	159.45	75.9
$(Yb_{1-x}Bi_x)_2O_3$	Yb_2O_3	Cubic	10.4360	1136.59	24.1

SINTERED					
(Yb,Bi)$_2$O$_3$	Defect-fluorite	Cubic	5.40959	159.30	83.2
(Yb$_{1-x}$Bi$_x$)$_2$O$_3$	Yb$_2$O$_3$	Cubic	10.4335	1135.77	16.8

4.2.1.2 xCaZrO$_3$ – (1-x)BiYbO$_3$ x = 0.02

The results from the XRD measurement of the calcinated and the sintered $Bi_{0.98}Ca_{0.02}Yb_{0.98}Zr_{0.02}O_3$ are summarized in Table 11. The composition of both samples again shows a phase with a small, cubic defect-fluorite cell and a secondary phase with a big, cubic cell with Yb_2O_3 structure.

After sintering the cell volume again is lower than just after calcination. Furthermore the phase fraction of the defect-fluorite increases and the Yb_2O_3 decreases after sintering.

Table 11: List of the phases, the structure type, the symmetry, the lattice parameters, the cell volume and the weight percent of the sample with nominal composition $Bi_{0.98}Ca_{0.02}Yb_{0.98}Zr_{0.02}O_3$ after calcination and sintering.

CALCINATED					
Phase	**Type of Structure**	**Symmetry**	**a [Å]**	**Cell volume [Å^3]**	**Wt%**
(Yb,Bi)$_2$O$_3$	Defect-fluorite	Cubic	5.4206	159.27	74.5
(Yb$_{1-x}$Bi$_x$)$_2$O$_3$	Yb$_2$O$_3$	Cubic	10.4354	1136.39	25.5
SINTERED					
(Yb,Bi)$_2$O$_3$	Defect-fluorite	Cubic	5.40984	158.30	82.4
(Yb$_{1-x}$Bi$_x$)$_2$O$_3$	Yb$_2$O$_3$	Cubic	10.4339	1135.90	17.6

4.2.1.3 xCaZrO$_3$ – (1-x)BiYbO$_3$ x = 0.1

The data of the XRD measurement of the calcinated and the sintered $Bi_{0.90}Ca_{0.10}Yb_{0.90}Zr_{0.10}O_3$ are listed in Table 12. After calcination four distinct phases could be identified in these samples. Two of them are already known as the cubic Bi-rich and a Bi-deficient phase. The third is identified as orthorhombic $CaZrO_3$ with a fraction of 2.6 wt% and the fourth phase as monoclinic Bi_2O_3 with a fraction of 1 wt%. After sintering the third and the fourth phase could not be detected anymore.

Table 12: List of the phases, the structure type, the symmetry, the lattice parameters, the cell volume and the weight percent of the sample with nominal composition $Bi_{0.90}Ca_{0.10}Yb_{0.90}Zr_{0.10}O_3$ after calcination and sintering.

CALCINATED							
Phase	**Type of Structure**	**Symmetry**	**a [Å]**	**b [Å]**	**c [Å]**	**Cell volume [Å^3]**	**Wt%**
$(Yb,Bi)_2O_3$	Defect-fluorite	Cubic	5.4286	5.4286	5.4286	159.98	64.6
$(Yb_{1-x}Bi_x)_2O_3$	Yb_2O_3	Cubic	10.4365	10.4365	10.4365	1136.75	31.8
$CaZrO_3$		Ortho-rhombic	0.05787	8.007	5.647	2.62	2.6
Bi_2O_3		Monoclinic	5.892	8.134	7.558	362.22	1.0
SINTERED							
$(Yb,Bi)_2O_3$	Defect-fluorite	Cubic	5.41669	5.41669	5.41669	158.93	76.7
$(Yb_{1-x}Bi_x)_2O_3$	Yb_2O_3	Cubic	10.4324	10.4324	10.4324	1135.41	23.3

4.2.1.4 xSrZrO$_3$ – (1-x)BiYbO$_3$ $x = 0.02$

As seen in Table 13 the results of the calcinated and the sintered sample are similar to the samples of xCaZrO$_3$ – (1-x)BiYbO$_3$ with a molar content of 2 mol%. Again two phases which can be identified as the two cubic Yb-Bi-compounds are found. After sintering the cell volume shows lower values than the calcinated one. The phase fraction of the defect-fluorite increases and the Yb_2O_3 decreases after sintering.

Table 13: List of the phases, the structure type, the symmetry, the lattice parameters, the cell volume and the weight percent of the sample with nominal composition $Bi_{0.98}Sr_{0.02}Yb_{0.98}Zr_{0.02}O_3$ after calcination and sintering.

CALCINATED					
Phase	**Type of Structure**	**Symmetry**	**a [Å]**	**Cell volume [Å^3]**	**Wt%**
$(Yb,Bi)_2O_3$	Defect-fluorite	Cubic	5.4168	158.94	75.8
$(Yb_{1-x}Bi_x)_2O_3$	Yb_2O_3	Cubic	10.4373	1137.01	24.2
SINTERED					
$(Yb,Bi)_2O_3$	Defect-fluorite	Cubic	5.41171	158.49	81.6
$(Yb_{1-x}Bi_x)_2O_3$	Yb_2O_3	Cubic	10.4357	1136.49	18.4

4.2.1.5 *x*$SrZrO_3$ – (1-*x*) $BiYbO_3$ *x* = 0.1

The data of the XRD measurement reveal three different phases after calcination, which are listed in Table 14. Two of them are already known as the cubic Bi-compounds and the third is identified as trigonal $Bi_6Sr_2O_{11}$ with a fraction of 7.6 wt%. This third compound is not found after sintering.

Table 14: List of the phases, the structure type, the symmetry, the lattice parameters, the cell volume and the weight percent of the sample with nominal composition $Bi_{0.90}Sr_{0.10}Yb_{0.90}Zr_{0.10}O_3$ after calcination and sintering.

CALCINATED							
Phase	**Type of Structure**	**Symmetry**	**a [Å]**	**b [Å]**	**c [Å]**	**Cell volume [Å^3]**	**Wt%**
$(Yb,Bi)_2O_3$	Defect-fluorite	Cubic	5.4282	5.4282	5.4282	159.94	62.6
$(Yb_{1-x}Bi_x)_2O_3$	Yb_2O_3	Cubic	10.4362	10.4362	10.4362	1136.65	29.8
$Bi_6Sr_2O_{11}$		Trigonal	3.9493	3.9493	28.131	438.76	7.6
SINTERED							
$(Yb,Bi)_2O_3$	Defect-fluorite	Cubic	5.43484	5.43484	5.43484	160.53	74.4
$(Yb_{1-x}Bi_x)_2O_3$	Yb_2O_3	Cubic	10.4329	10.4329	10.4329	1135.57	25.6

4.2.1.6 $(Bi_{1-x}La_x)YbO_3$ *x* = 0.1

Likewise in the Lanthanum-substituted $BiYbO_3$ three phases can be determined after calcination (Table 15). The third phase is identified as around 9 wt% of the trigonal $(La_{0.225}Bi_{0.775})_2O_3$ which disappears after sintering (Table 15).

Table 15: List of the phases, the structure type, the symmetry, the lattice parameters, the cell volume and the weight percent of the sample with nominal composition $(Bi_{0.90}La_{0.10})YbO_3$ after calcination and sintering.

CALCINATED							
Phase	**Type of Structure**	**Symmetry**	**a [Å]**	**b [Å]**	**c [Å]**	**Cell volume [Å^3]**	**Wt%**
$(Yb,Bi)_2O_3$	Defect-fluorite	Cubic	5.4327	5.4327	5.4327	160.34	58.7
$(Yb_{1-x}Bi_x)_2O_3$	Yb_2O_3	Cubic	10.4367	10.4367	10.4367	1136.81	32.3
$(La_{0.225}Bi_{0.775})_2O_3$		Trigonal	4.011	4.011	27.497	442.38	9.0

SINTERED							
$(Yb,Bi)_2O_3$	Defect-fluorite	Cubic	5.4307	5.4307	5.4307	160.16	77.4
$(Yb_{1-x}Bi_x)_2O_3$	Yb_2O_3	Cubic	10.4343	10.4343	10.4343	1136.03	22.6

4.2.2 Densification and Shrinkage

The theoretical density as well as the relative density of the samples cannot be determined due to the multi-phase composition which is measured by the X-ray diffraction analysis and unknown compositions. For that reason the shrinkage data are much more meaningful in the assessment of the sintering process. The apparent density, which is measured by the Archimedes method, is shown in Table 16.

Table 16: List of the apparent density of the different samples.

Sample	Archimedes' density [$g \cdot cm^{-3}$]
BY	8.75
CZBY2	8.79
CZBY10	8.23
SZBY2	8.79
SZBY10	8.68
BLY10	8.56

Both samples, CZBY2 and SZBY2 have the same value for the apparent density. The samples CZBY10 and SZBY10 show lower values for the apparent density related to the samples with a concentration of 2 mol%. This behaviour can also be seen in the shrinkage measurement (Figure 21).

As seen in Figure 21 the highest shrinkage values can be achieved with BY and LBY10. These data indicate that these samples achieved a higher density compared to the others.

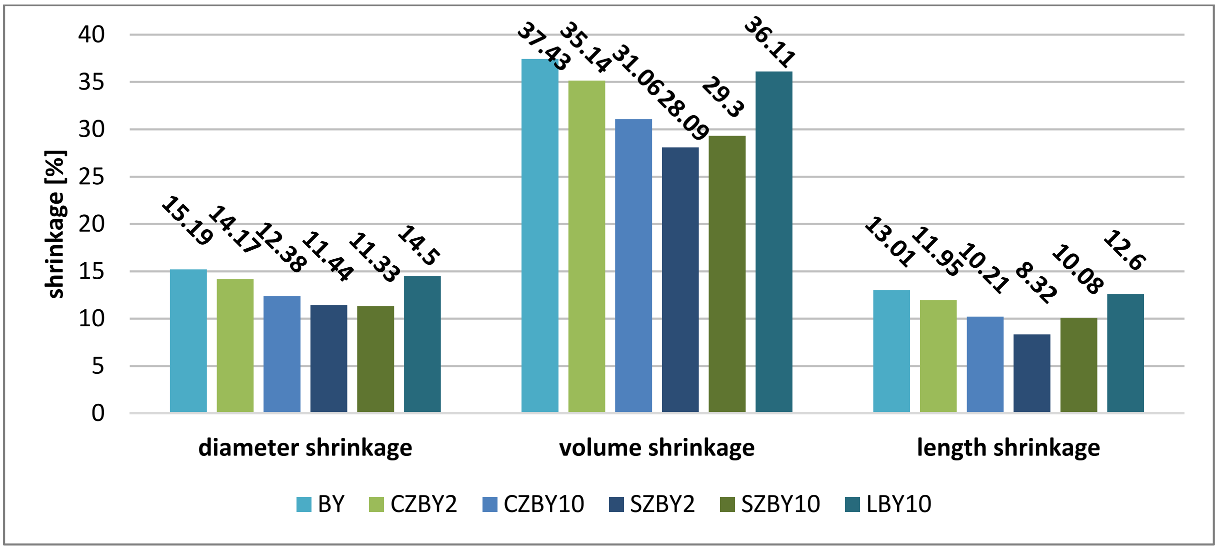

Figure 21: Shrinkage measurement of the different substitutions of $BiYbO_3$.

4.2.3 Small Signal Electrical Measurement

Small signal values of capacitance, loss factor and relative permittivity of all samples are documented in the following table (Table 17).

Almost all samples are recorded with a frequency of 10 kHz. For the samples CZBY10 and SZBY10 a higher frequency of 100 kHz is used as the metering range for the capacity and the loss factor is not sufficient.

The influence of the substitution of $BiYbO_3$ with $CaZrO_3$ and $SrZrO_3$ is rather similar: Relative permittivity declines from 18 to ~15 by increasing the amount of both dopants from 2 mol% to 10 mol%. The loss factor decreases from 0.007 to 0.004 with higher concentration. On the other hand, the substitution of 10 mol% Lanthanum for Bismuth increases the relative permittivity and the loss factor is twice as high as the average.

Table 17: Results of small signal electrical measurements of the different substitutions in $BiYbO_3$.

Sample	Capacitance [pF]	Loss factor []	Relative permittivity []
BY	13.94	0.005	18
CZBY2	13.36	0.004	18
CZBY10	11.53	0.004	15
SZBY2	12.66	0.007	18
SZBY10	11.55	0.006	16
LBY10	12.59	0.013	19

4.2.4 Hysteresis Loops

The polarization curves of the samples BY, CZBY2, CZBY10 and SZBY10 could not be measured and thus they are not shown in this chapter. Therefore only the polarization curves of LBY10 and SZBY2, which are measured at room temperature, are shown in Figure 22 and Figure 23.

In Figure 22 the hysteresis loop of the Lanthanum-substitution in $BiYbO_3$ is shown. No phase transition from antiferroelectric to ferroelectric behaviour could be observed. This might be an effect of the secondary phases.
Despite the fact that a high electric field is applied, the hysteresis loops reach only low polarization.

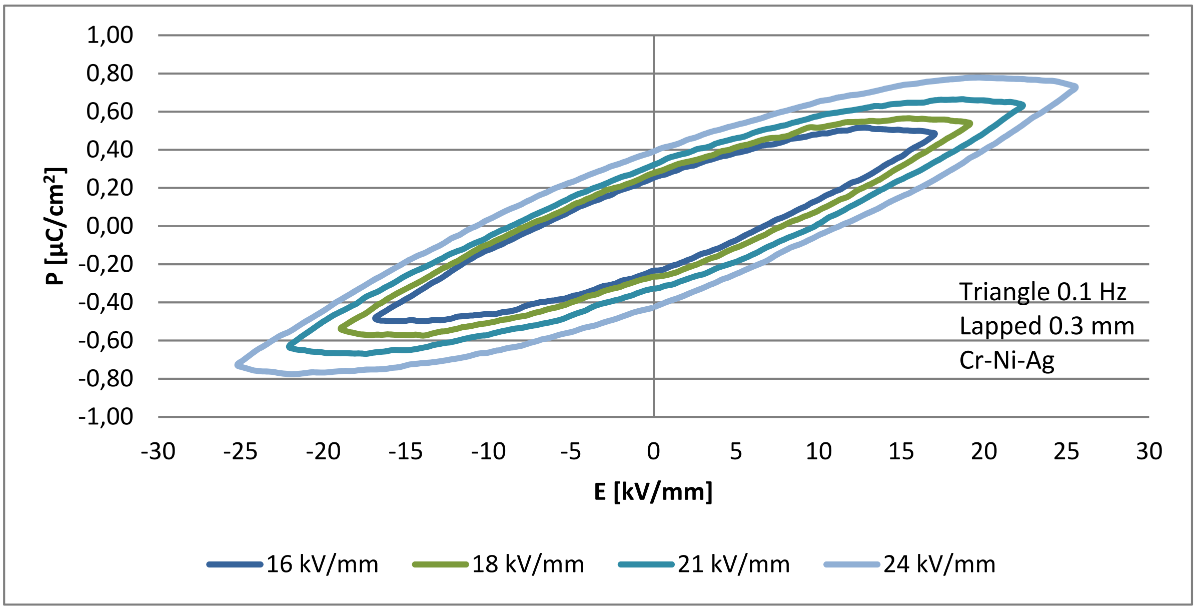

Figure 22: Polarization curves of Lanthanum substitution in $BiYbO_3$ at room temperature.

In Figure 23 the hysteresis loop of the 2 mol% $SrZrO_3$ doped $BiYbO_3$ is shown. Again no phase transition from antiferroelectric to ferroelectric behaviour could be observed. Also this sample shows low polarization at an applied high electric field.

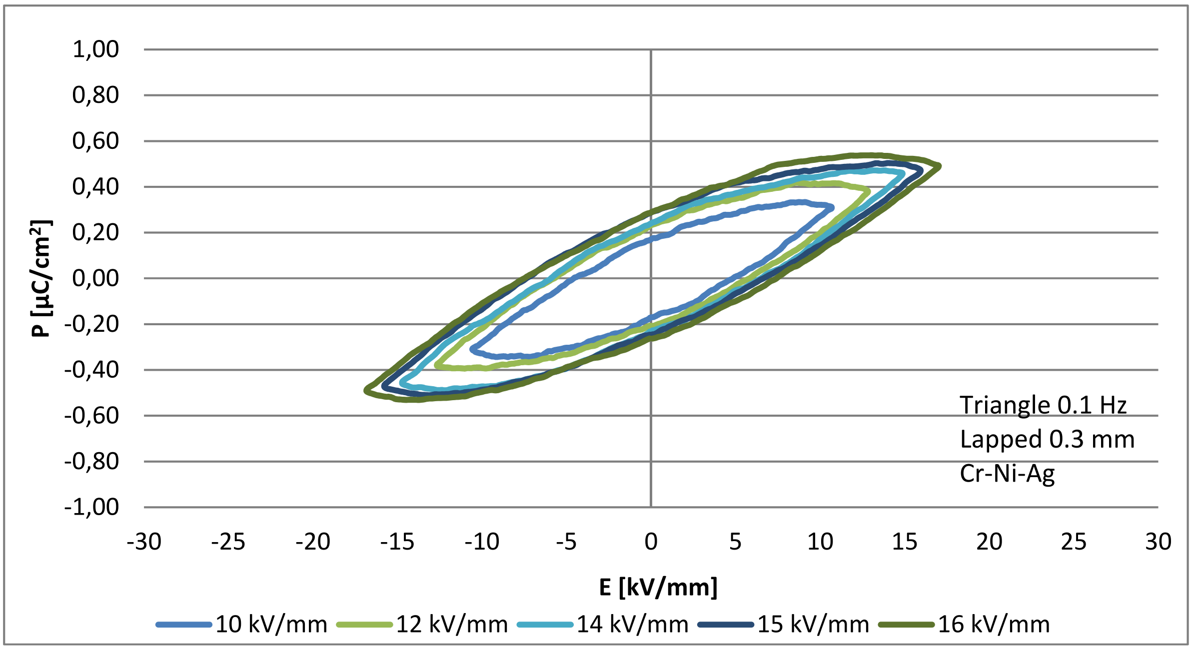

Figure 23: Polarization curves of $Bi_{0.98}Sr_{0.02}Yb_{0.98}Zr_{0.02}O_3$ at room temperature.

4.3 Properties of xLaYbO$_3$ - (1-x)CaZrO$_3$ and xLaYbO$_3$ - (1-x)SrZrO$_3$

This section provides information about the influence of La^{3+}- and Yb^{3+}- substitution on the CaZrO$_3$- and SrZrO$_3$-based ceramics. The preparation is done with nearly the same conditions as they are used in chapter 4.1. Only the holding period for the sintering process is changed from 2 h to 5 h.

The attention lies on the mechanism of the formation reaction, the density measurement as well as the dielectric properties.

4.3.1 X-ray Diffraction

The Rietveld refinement results of the compositions $Ca_{0.90}La_{0.10}Zr_{0.9}Yb_{0.10}O_3$ and $Sr_{0.90}La_{0.10}Zr_{0.9}Yb_{0.10}O_3$ are presented in Table 18 and Table 19. Both calcinated samples show multiphase composition and after sintering only one phase remains.

4.3.1.1 xLaYbO$_3$ – (1-x)CaZrO$_3$ x = 0.1

The achieved results from the XRD measurement of the calcinated powder indicate three phases (Table 18). The main component in this composition is the orthorhombic CaZrO$_3$. The other phases are identified as the big, cubic cell which has a Yb$_2$O$_3$ structure and a small amount of the hexagonal La(OH)$_3$ can be seen. After sintering only a pure phase of CaZrO$_3$ is left over, in which a slight increase in cell volume can be detected (Table 18). The two phases are possibly incorporated in the crystal structure of the perovskite.

Table 18: List of the phases, the symmetry, the lattice parameters, the cell volume and the weight percent of the sample with nominal composition $Ca_{0.90}La_{0.10}Zr_{0.9}Yb_{0.10}O_3$ after calcination and sintering.

CALCINATED						
Phase	**Symmetry**	**a [Å]**	**b [Å]**	**c [Å]**	**Cell volume [Å^3]**	**Wt%**
CaZrO$_3$	Orthorhombic	5.7619	8.0315	5.6064	259.45	80.9
Yb$_2$O$_3$	Cubic	10.4346	10.4346	10.4346	1136.13	16.6
La(OH)$_3$	Hexagonal	6.5321	6.5321	3.84735	164.16	2.5
SINTERED						
CaZrO$_3$	Orthorhombic	5.8033	8.0985	5.6488	265.48	100

4.3.1.2 *x*$LaYbO_3$ – (1-*x*)$SrZrO_3$ *x* = 0.1

As seen in Table 19, this composition shows four phases after calcination. In this case the orthorhombic $SrZrO_3$ is the main component. Again the cubic Yb_2O_3 and the hexagonal $La(OH)_3$ could be discovered through the XRD analysis. A further compound is the orthorhombic $SrYb_2O_4$ which also manifests small amounts in the structure. After the sintering process only a pure phase of the main component remains in the SZ-based system (Table 19). Besides the cell volume is slightly risen.

Table 19: List of the phases, the symmetry, the lattice parameters, the cell volume and the weight percent of the sample with nominal composition $Sr_{0.90}La_{0.10}Zr_{0.9}Yb_{0.10}O_3$ after calcination and sintering.

CALCINATED						
Phase	**Symmetry**	**a [Å]**	**b [Å]**	**c [Å]**	**Cell volume [Å^3]**	**Wt%**
$SrZrO_3$	Orthorhombic	5.7984	5.8262	8.2027	277.11	80.9
Yb_2O_3	Cubic	10.425	10.425	10.425	1133.00	16.6
$SrYb_2O_4$	Orthorhombic	9.990	11.806	3.3578	393.03	4.7
$La(OH)_3$	Hexagonal	6.530		3.854	164.34	1.3
SINTERED						
$SrZrO_3$	Orthorhombic	5.8082	5.8542	8.2350	280.01	100

4.3.2 Densification and Shrinkage

The theoretical density and the relative density of the samples LYCZ10 and LYSZ10 can only be estimated as there are no comparable values from literature available (Table 20).

The results of the substituted $CaZrO_3$ with a content of 10 mol% $LaYbO_3$ achieve a high relative density which can be reflected in the shrinkage measurements. Moreover, the apparent density and the theoretical one show nearly the same value. On the other hand, the value for the LYSZ10 ceramics is not possible as it cannot achieve a relative density above 100 %. This could be caused, if the secondary phases of the sample contain non-detectable amorphous fractions. However this cannot be clarified in thesis as no SEM (scanning electron microscope) image is recorded.

Table 20: List of the densities of $Ca_{0.90}La_{0.10}Zr_{0.9}Yb_{0.10}O_3$ and $Sr_{0.90}La_{0.10}Zr_{0.9}Yb_{0.10}O_3$.

Sample	**Theoretical density [g·cm^{-3}]**	**Archimedes' density [g·cm^{-3}]**	**Relative density [%]**
LYCZ10	4.938	4.89	99.03
LYSZ10	5.381	5.57	103.45

In Figure 24 the data for shrinkage of the CZ-based ceramic show high values which indicate that this sample is very dense. For the other sample, this conclusion cannot be claimed.

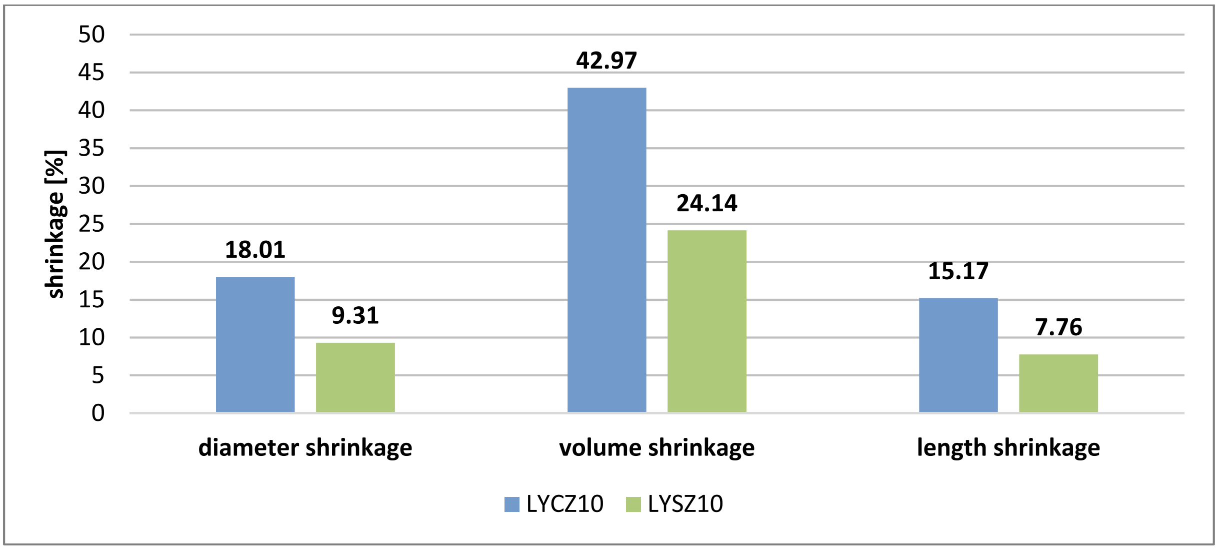

Figure 24: Comparison of shrinkage values between the geometric density of the green body and sintered samples of $Ca_{0.90}La_{0.10}Zr_{0.9}Yb_{0.10}O_3$ and $Sr_{0.90}La_{0.10}Zr_{0.9}Yb_{0.10}O_3$ ceramics.

4.3.3 Small Signal Electrical Measurement

Capacitance, loss factor and relative permittivity have been measured at room temperature with a frequency of 10 kHz for the CZ-based system and with 100 kHz for the SZ-based system (Table 21). The relative permittivity and loss factor of both systems are very low which is comparable to paraelectric materials.

Table 21: Results of the small signal electrical measurements of $Ca_{0.90}La_{0.10}Zr_{0.9}Yb_{0.10}O_3$ and $Sr_{0.90}La_{0.10}Zr_{0.9}Yb_{0.10}O_3$ ceramics.

Sample	**Capacitance [pF]**	**Loss factor []**	**Relative permittivity []**
LYCZ10	17.09	0.01	24
LYSZ10	10.54	0.004	15

4.3.4 Hysteresis Loops

For these samples no polarization curves can be measured. Polarization is so low that only noise can be detected. Therefore the curves are not shown here.

5 Conclusion

It was shown that solid solutions of $x\mathrm{CaZrO_3} – (1-x)\mathrm{NaNbO_3}$ (CZNN with x = 0.00, 0.02, 0.04 and 0.10) could be synthesized by the mixed oxide route. Sintered samples of CZNN consist of single phase perovskite. The relative density of samples up to x = 0.04 exceeds 96%, which indicates adequate densification for further electrical characterization. For CZNN with x = 0.10 a relative density of only 89% is obtained.

The relative permittivity of samples up to x = 0.04 increases with increasing x and ranges from 200 to 270. The loss factor of these samples is below 0.02. Polarization curves showed rather paraelectric behaviour without a typical ferroelectric hysteresis or antiferroelectric double-hysteresis. The polarization curves shown by Shimizu et al.[4] could not be reproduced and no switching was observed although the samples exceeded the breakdown strength of the samples described in that reference.

$BiYbO_3$ ceramics doped with $CaZrO_3$, $SrZrO_3$ and La_2O_3 are also prepared via mixed oxide route. XRD data show that all samples consist of two phases. Calcinated as well as sintered $BiYbO_3$ samples show a Bi-rich phase with a small cubic defect-fluorite cell and a secondary Bi- deficient phase with a larger cubic cell, which has a Yb_2O_3 structure. After sintering the fraction of the secondary phase decreases.

$BiYbO_3$ exhibits a relative permittivity of 18, which remains unchanged in solid solutions with 2 mol% $CaZrO_3$ or $SrZrO_3$ as well as with 10 mol% La_2O_3. 10 mol% of $CaZrO_3$ or $SrZrO_3$ reduce the relative permittivity to 15. No sample showed ferroelectric or antiferroelectric behaviour under high electric field conditions. For relaxor dielectrics containing $BiYbO_3$ it can be assumed that this component acts only as dopant. In $BaTiO_3$-based ceramics $BiYbO_3$ obviously has the function of a compensated donor-acceptor pair. The lone pair of Bi^{3+} does not make any contribution to orientation polarization.

Finally, the concept of lowering tolerance factor and increasing electronegativity difference was applied to $CaZrO_3$- and $SrZrO_3$-based ceramics by substitution of La^{3+}- and Yb^{3+}- on A- and B-site, respectively, with a concentration of 10 mol% (LYCZ and LYSZ). The Rietveld refinement results of calcinated samples show multiphase composition but after sintering only a single phase remains.

The relative permittivity for LYCZ is 24, that of LYSZ is 15. These samples again show no ferroelectric or antiferroelectric polarization.

To sum up, the reduction of tolerance factor and the increase of electronegativity difference is not sufficient to stabilize the antiferroelectric phase in polar oxides. Obviously other factors, which have to be found in further investigations, as well as processing play an important role for the stabilization of the antiferroelectric phase.

List of References

[1] A. J. Moulson, J. M. Herbert, Electroceramics: Materials, Properties, Applications, second ed., John Wiley & Sons Ltd., West Sussex, England, 2003.

[2] Amtsblatt der Europäischen Union. Richtlinie 2002/95/EG DES EUROPÄISCHEN PARLAMENTS UND DES RATES vom 27. Januar 2003 zur Beschränkung und Verwendung bestimmter gefährlicher Stoffe in Elektro- und Elektronikgeräten, L37 (2003) 19 - 23.

[3] Koruza, J., Tellier, J., Malič, B., Bobnar, V., Kosec, M., Phase transitions of sodium niobate powder and ceramics, prepared by solid state synthesis, J. Appl. Phys. 108 (2010) 113509 – 9.

[4] Shimizu, H., Guo, H., Reyes-Lillo, S.E., Mizuno, Y., Rabe, K.M., Randall, C.A., Lead-free antiferroelectric: $xCaZrO_3$-(1-x)$NaNbO_3$ system ($0 \le x \le 0.10$), Dalton Trans. 44 (2015) 10763 - 10772.

[5] T. Kainz, Relationship of Structure and Properties of antiferroelectric Lead Zirconate – Lead Titanate, Technical University Graz, 2015.

[6] Schileo, G., Luisman, L., Feteira, A., Deluca, M., Reichmann, K., Structure-property relationships in $BaTiO_3$-$BiFeO_3$-$BiYbO_3$ ceramics, J. Europ. Ceram. Soc. 33 (2013) 1457 - 68.

[7] Guo, H., Shimizu, H., Mizuno, Y., Randall, C.A., Strategy for stabilization of the antiferroelectric phase (Pmba) over the metastable ferroelectric phase (P21ma) to establish double loop hysteresis in lead-free (1-x) $NaNbO_3$-x$SrZrO_3$ solid solution, J. Appl. Phys. 117 (2015) 214103.

[8] Wood, E.A., Polymorphism in potassium niobate, sodium niobate, and other ABO_3 compounds, Acta Cryst. 4 (1951) 353 – 362.

[9] Lefkowitz, I., Lukaszewicz, K., Megaw, H. D., The high-temperature phases of sodium niobate and the nature of transitions in pseudosymmetric structures, Acta Cryst. 20 (1966) 670 – 683.

[10] Megaw, H. D., The seven phases of sodium niobate. Ferroelectrics, 7 (1974) 87 – 89.

[11] Matthias, B. T., New Ferroelectric Crystals, Phys. Rev. 75 (1949) 1771 – 1771.

[12] K.M. Rabe, Functional Metal Oxides: New Science and Novel Applications, Wiley, New York, 2013.

[13] Tan, X., Ma, C., Frederick, J., Beckman, S., Webber, K. G., The Antiferroelectric ↔ Ferroelectric Phase Transition in Lead-Containing and Lead-Free Perovskite Ceramics, J. Am. Ceram. Soc. 94 (2011) 4091 - 4107.

[14] Liang, W., Wu, W., Xiao, D., Zhu, J., Effect of the Addition of $CaZrO_3$ and $LiNbO_3$ on the Phase Transitions and Piezoelectric Properties of $K_{0.5}Na_{0.5}NbO_3$ Lead-Free Ceramics, J. Am. Ceram. Soc. 94 (2011) 4317 - 4322.

[15] Liu, W., Ren, X., Large Piezoelectric Effect in Pb-Free Ceramics, Phys. Rev. Lett. 103 (2009) 257602.

[16] Buhrer, C.F., Some Properties of Bismuth Perovskites, J. Chem. Phys. 36 (3) (1962) 1962798 - 803.

[17] E. A. Moore, L. A. Smart, Solid State Chemistry: An Introduction, Taylor & Francis Group: New York, 2012.

[18] Haertling, G.H., Ferroelectric Ceramics: History and Technology, J. Am. Ceram. Soc. (1999) 797 – 818.

[19] V. M. Goldschmidt, Die Gesetze der Krystallochemie, Die Naturwissenschaften, 21 (1926) 477 - 478.

[20] Johnsonn, M., Lemmens, P., Crystallography and Chemistry of Perovskites, J. Phys.: Condensed Matter (2008) 1 – 6.

[21] Li, Z., Yang, M., Park, J.-S., Wie, S.-H., Berry, J.J., Zhu, K., Stabilizing Perovskite Structures by Tuning Tolerance Factor: Formation of Formamidinium and Cesium Lead Iodide Solid-State Alloys, Chem. Mater. 28 (1) (2016) 284 - 292.

[22] Shannon, R. D., Revised effective ionic radii and systematic studies of interatomic distances in halides and chaleogenides. Acta Cryst. 32 (1976) 751 - 67.

[23] L. Pauling, The Nature of the Chemical Bond, third ed., Cornell University Press, New York, 1960, 93.

[24] H. Schaumburg, Werkstoffe und Bauelemente der Elektrotechnik (5th ed.); Hamburg-Harburg, Stuttgart,1994.

[25] R. Waser, U. Böttger, S. Tiedke, Polar Oxides: Properties, Characterization, and Imaging, Wiley-VCH Verlag GmbH &Co. KgaA, Weinheim, 2005.

[26] Patel, S., Chauhan, A., Vaish, R., Enhancing electrical energy storage density in antiferroelectric ceramics using ferroelastic domain switching. Mater. Res. Express 1 (2014) 045502.

[27] C. Kittel, Introduction to Solid State Physics, Wiley, New York, 1996.

[28] K. C. Kao, Dielectric Phenomena in Solids, Elsevier Academic Press, 2004.

List of Figures

List of Tables

List of Equations

List of Abbreviations

ICSD	Inorganic Crystal Structure Database
XRD	X-ray diffraction
PZT	$Pb(ZrTi)O_3$
PLZT	$(PbLa)(ZrTi)O_3$
BF	$BiFeO_3$
FE	Ferroelectric
AFE	Antiferroelctric
NN	$NaNbO_3$
PZ	$PbZrO_3$
ST	$SrTiO_3$
CZNN0	$NaNbO_3$
CZNN2	$Na_{0.98}Ca_{0.02}Nb_{0.98}Zr_{0.02}O_3$
CZNN4	$Na_{0.96}Ca_{0.04}Nb_{0.96}Zr_{0.04}O_3$
CZNN10	$Na_{0.90}Ca_{0.10}Nb_{0\cdot90}Zr_{0.10}O_3$
BY	$BiYbO_3$
LBY10	$Bi_{0.90}La_{0.10}YbO_3$
SZBY2	$Bi_{0.98}Sr_{0.02}Yb_{0.98}Zr_{0.02}O_3$
SZBY10	$Bi_{0.90}Sr_{0.10}Yb_{0.90}Zr_{0.10}O_3$
CZBY2	$Bi_{0.98}Ca_{0.02}Yb_{0.98}Zr_{0.02}O_3$
CZBY10	$Bi_{0.90}Ca_{0.10}Yb_{0.90}Zr_{0.10}O_3$
LYCZ10	$Ca_{0.90}La_{0.10}Zr_{0.90}Yb_{0.10}O_3$
LYSZ10	$Sr_{0.90}La_{0.10}Zr_{0.90}Yb_{0.10}O_3$
Wt%	Weight percent
t	Goldschmidt tolerance factor
X	Electronegativity difference
SEM	Scanning electron microscopy

Appendix

Appendix 1: XRD spectra of the xCaZrO$_3$ – (1-x)NaNbO$_3$ compositions.

The blue solid line represent the experimental data and the red line the calculated patterns. The vertical bars indicate the positions of the diffraction peaks. The black line at the bottom displays the difference between the experimental and calculated data.

NaNbO$_3$

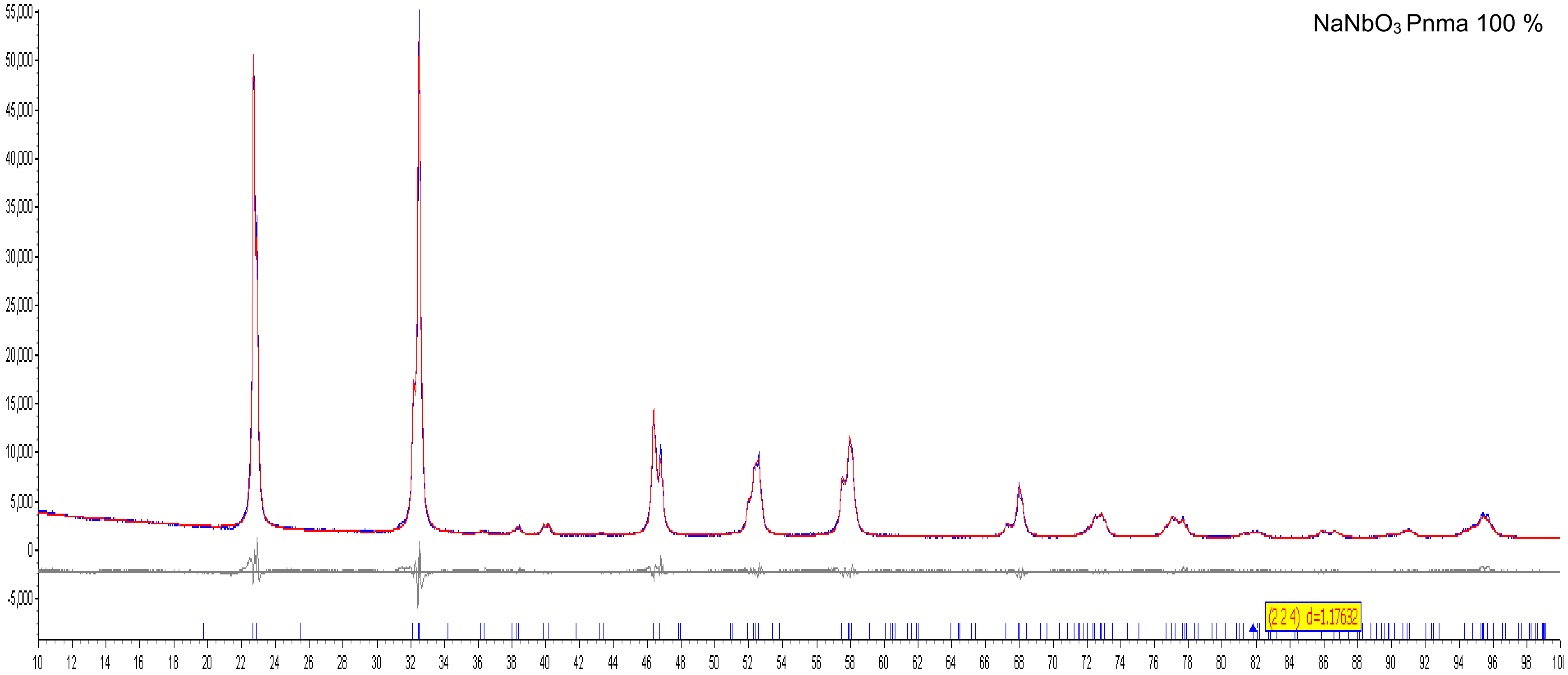

Figure 25: XRD pattern of calcinated powder of CZNN0.

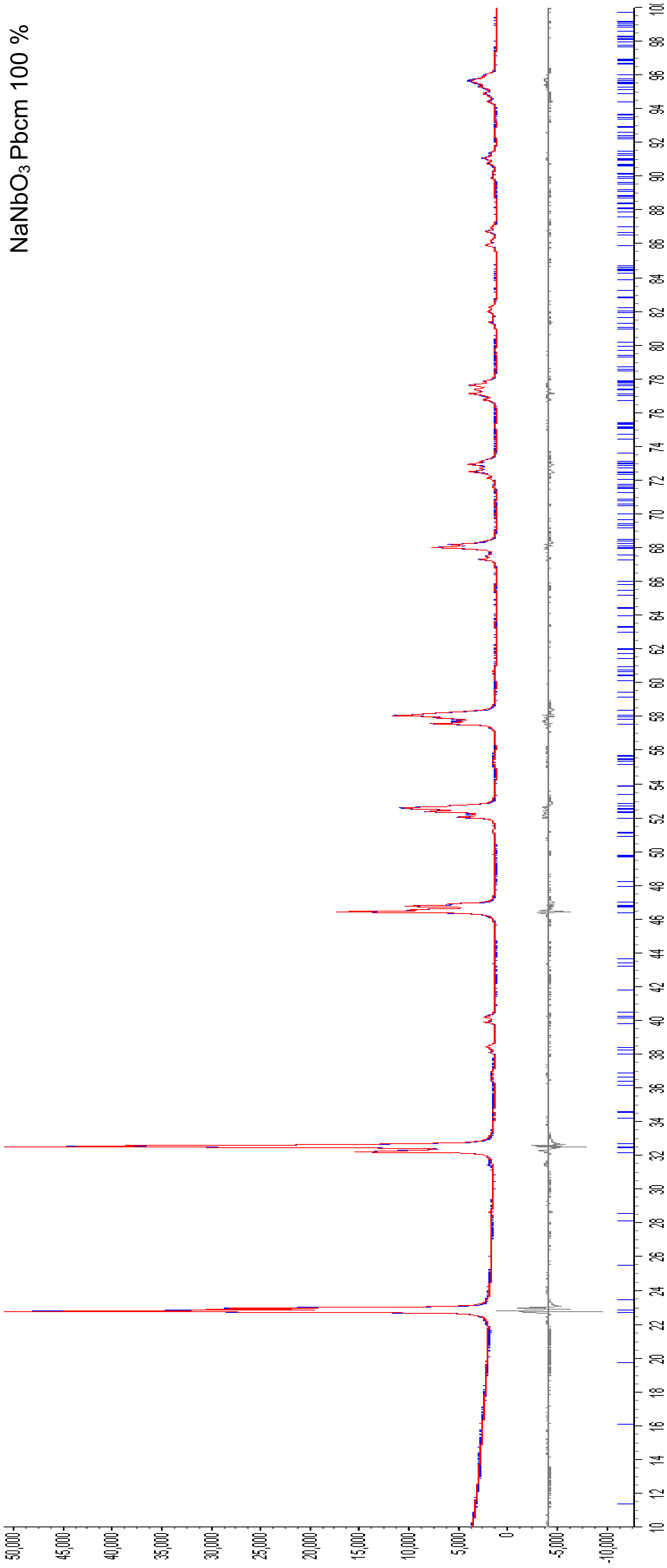

Figure 26: XRD pattern of CZNN0 after sintering.

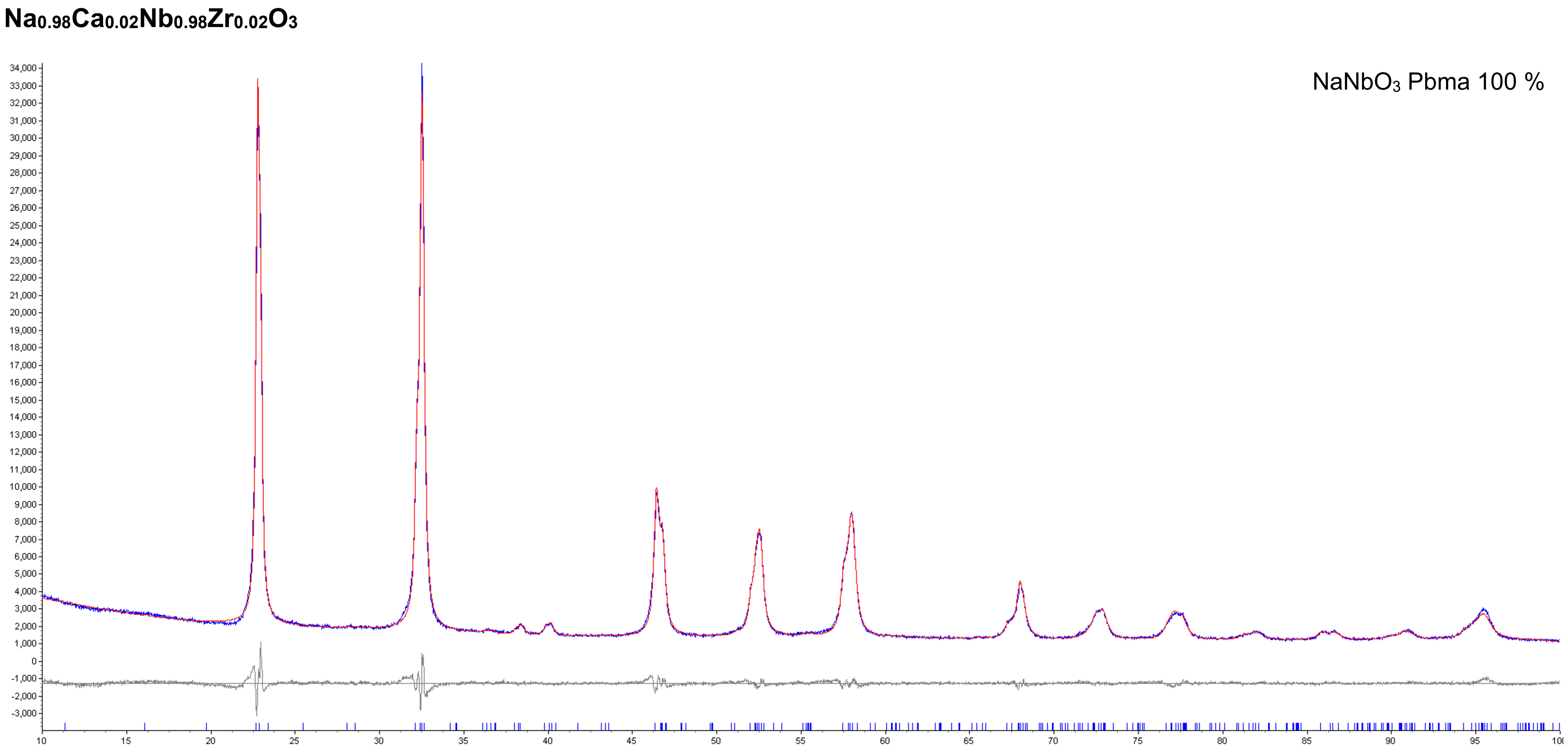

Figure 27: XRD pattern of calcinated powder of CZNN2.

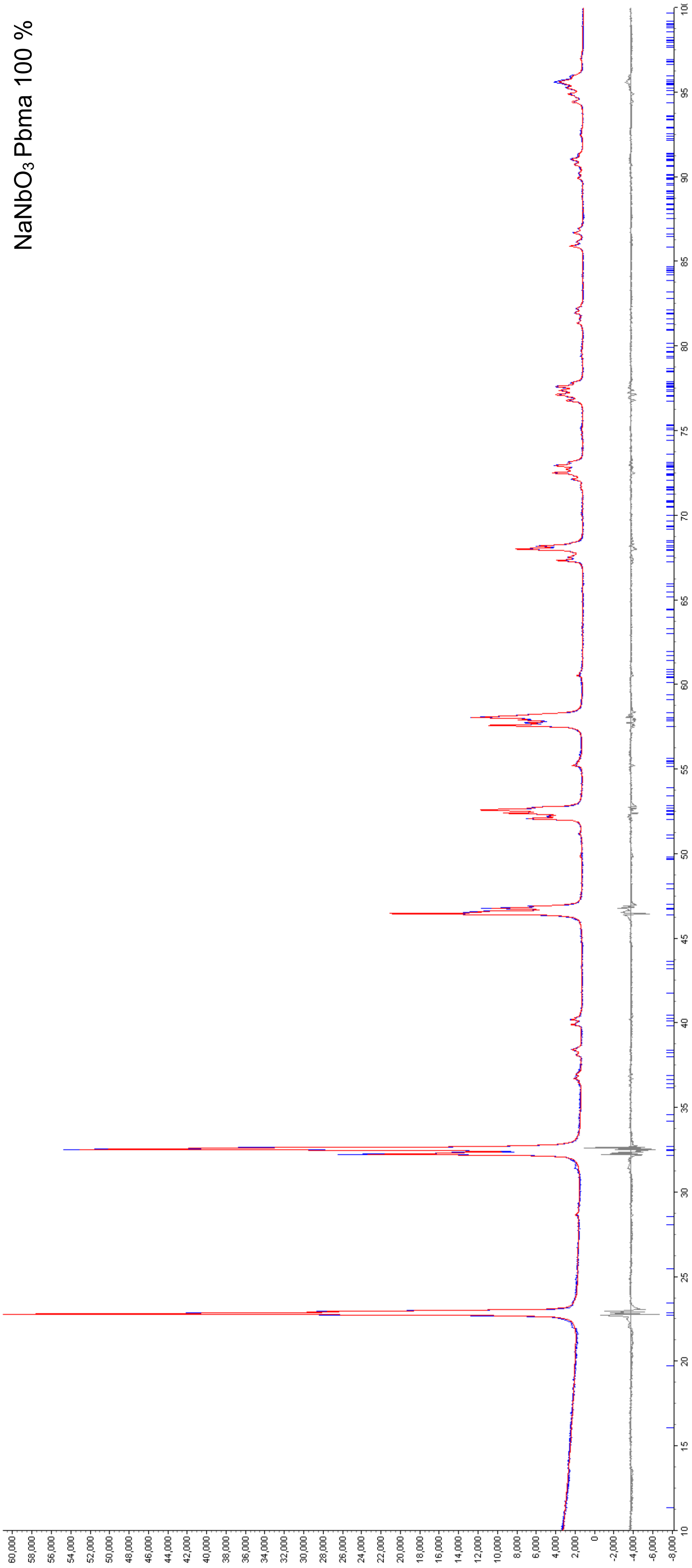

Figure 28: XRD pattern of CZNN2 after sintering.

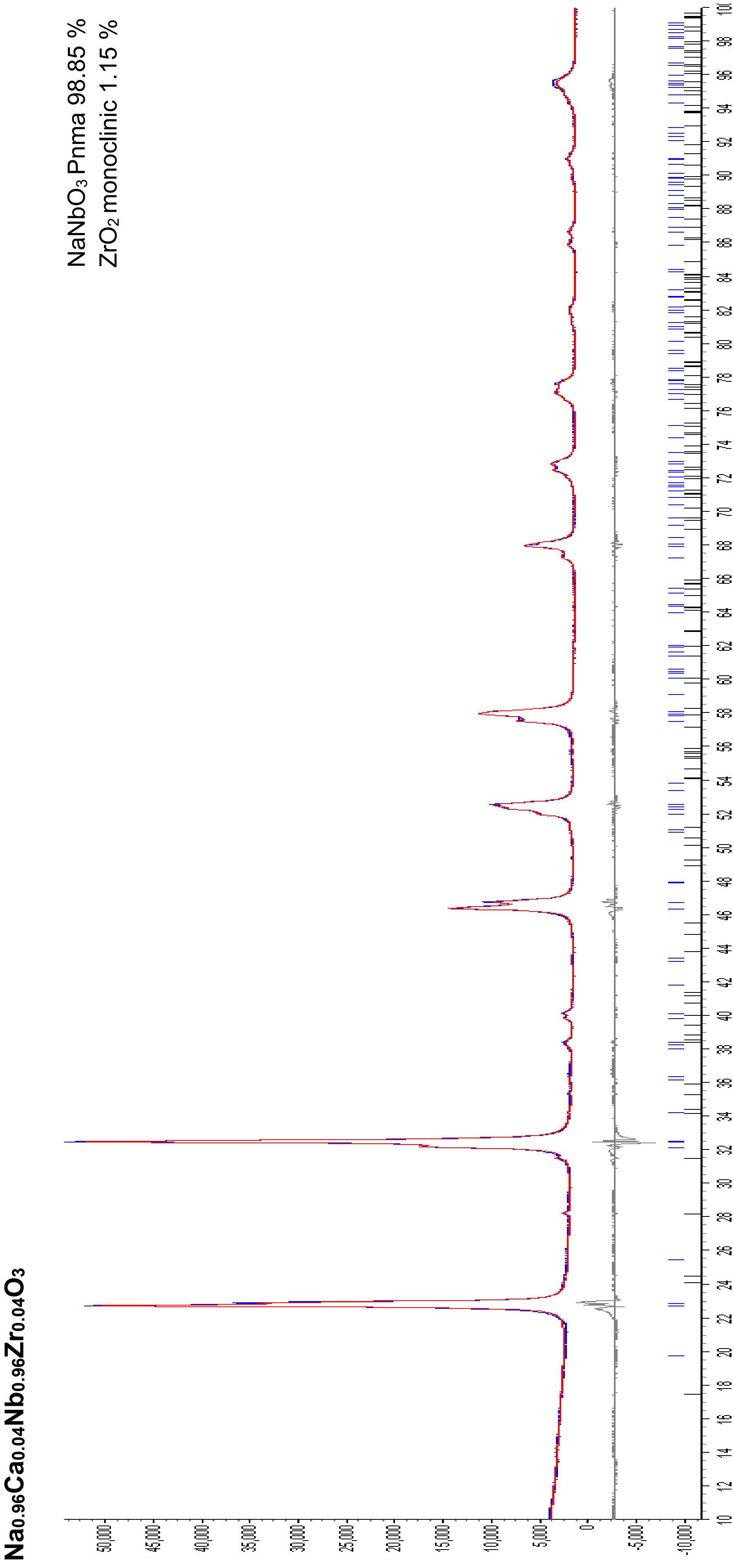

Figure 29: XRD pattern of calcinated powder of CZNN4.

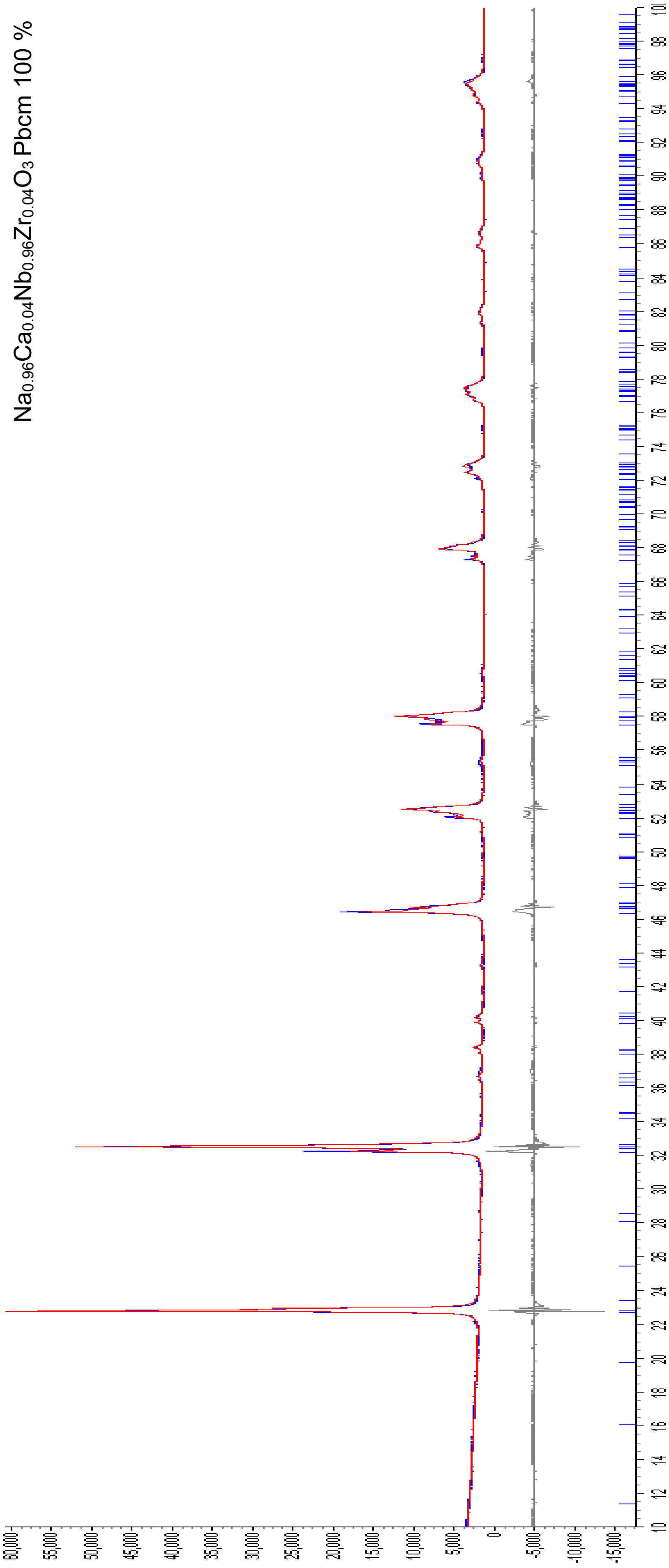

Figure 30: XRD pattern of CZNN4 after sintering.

$Na_{0.90}Ca_{0.10}Nb_{0.90}Zr_{0.10}O_3$

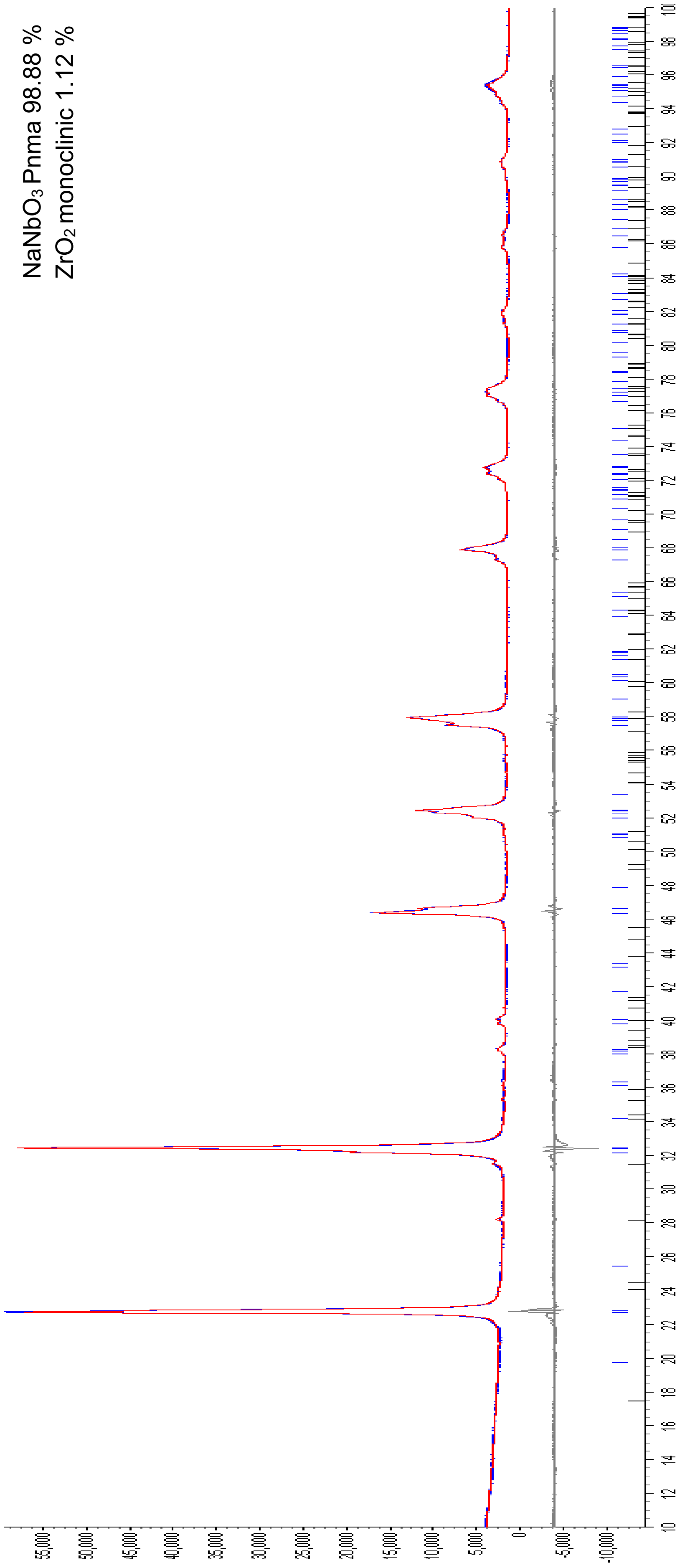

Figure 31: XRD pattern of calcinated powder of CZNN10.

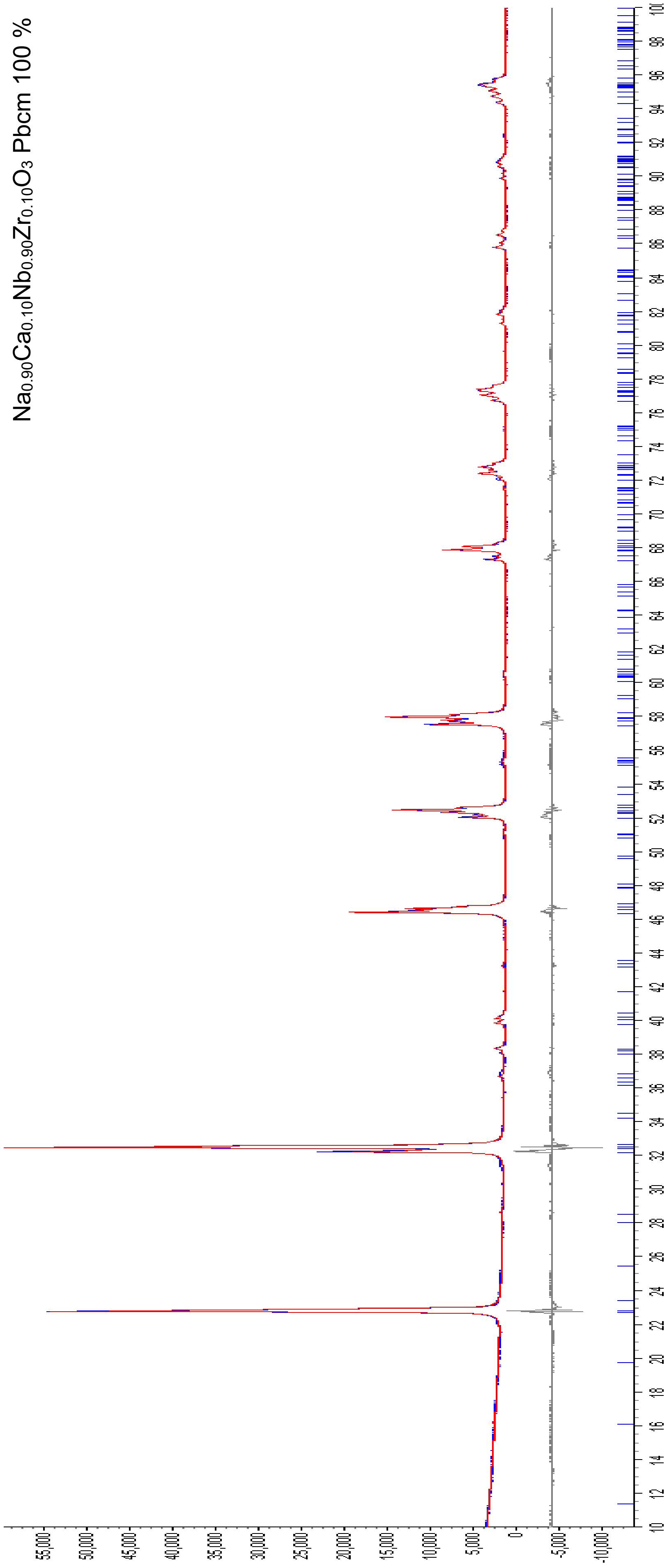

Figure 32: XRD pattern of CZNN10 after sintering.

Appendix 2: XRD spectra of the different doped $BiYbO_3$ compositions.

The blue solid line represent the experimental data and the red line the calculated patterns. The vertical bars indicate the positions of the diffraction peaks. The black line at the bottom displays the difference between the experimental and calculated data.

$BiYbO_3$ – Calcinated

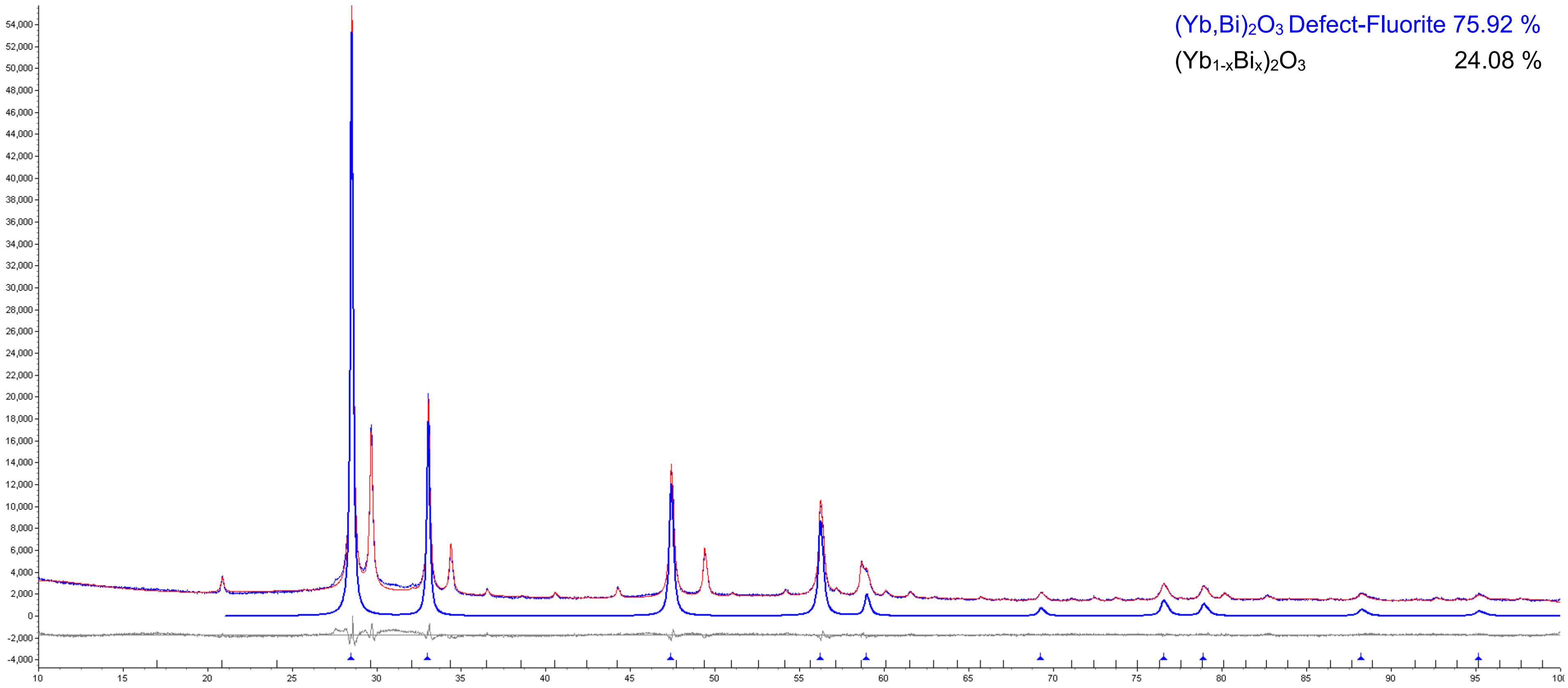

Figure 33a: XRD pattern of calcinated powder of $BiYbO_3$.

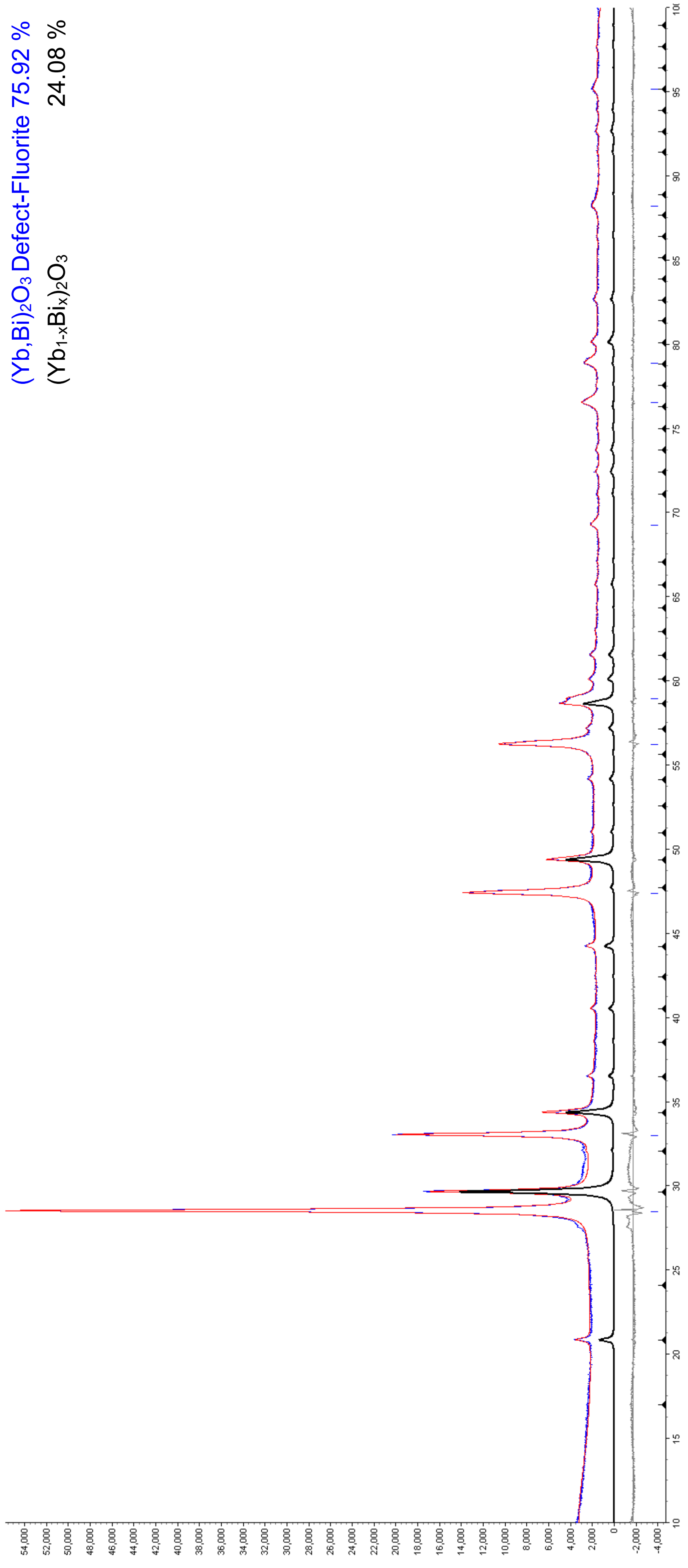

Figure 34b: XRD pattern of calcinated powder of BiYbO$_3$.

$BiYbO_3$ – Sintered

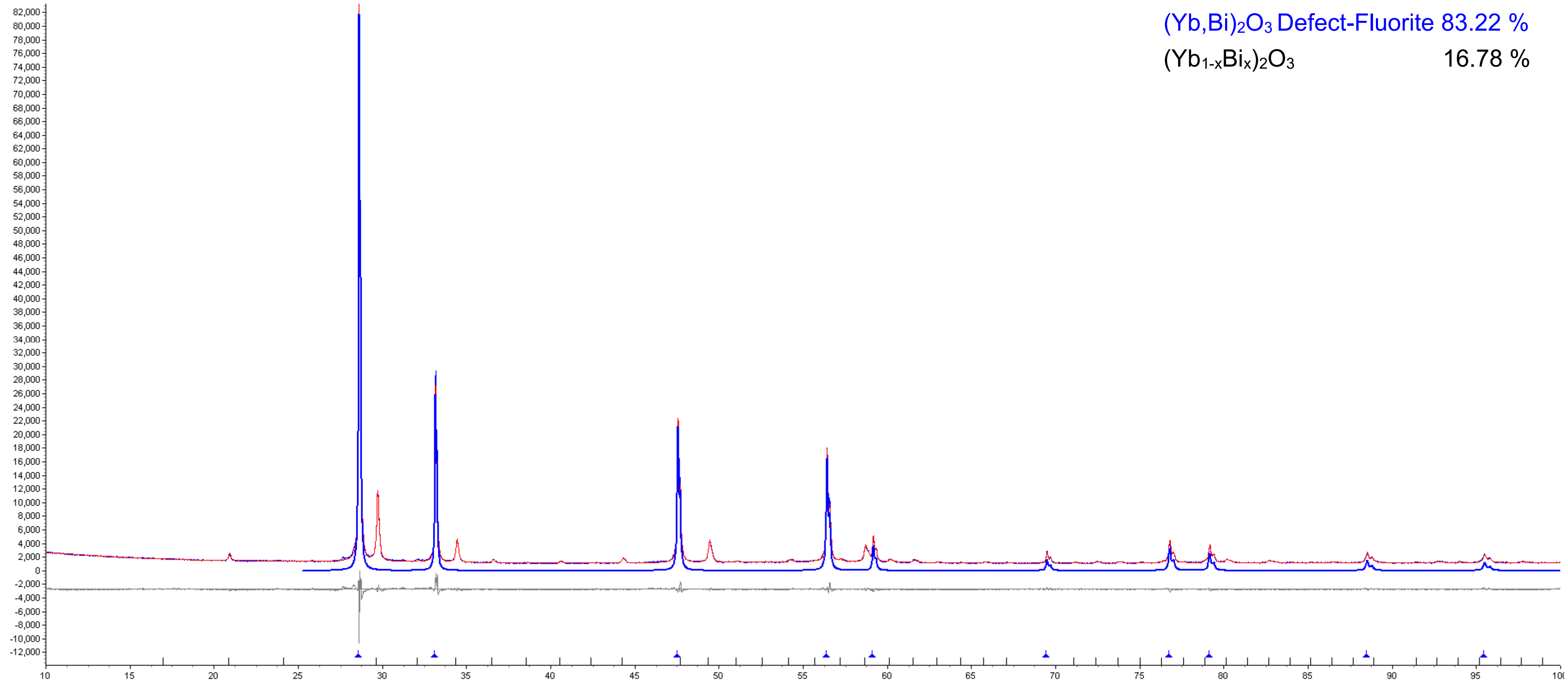

Figure 35a: XRD pattern of $BiYbO_3$ after sintering.

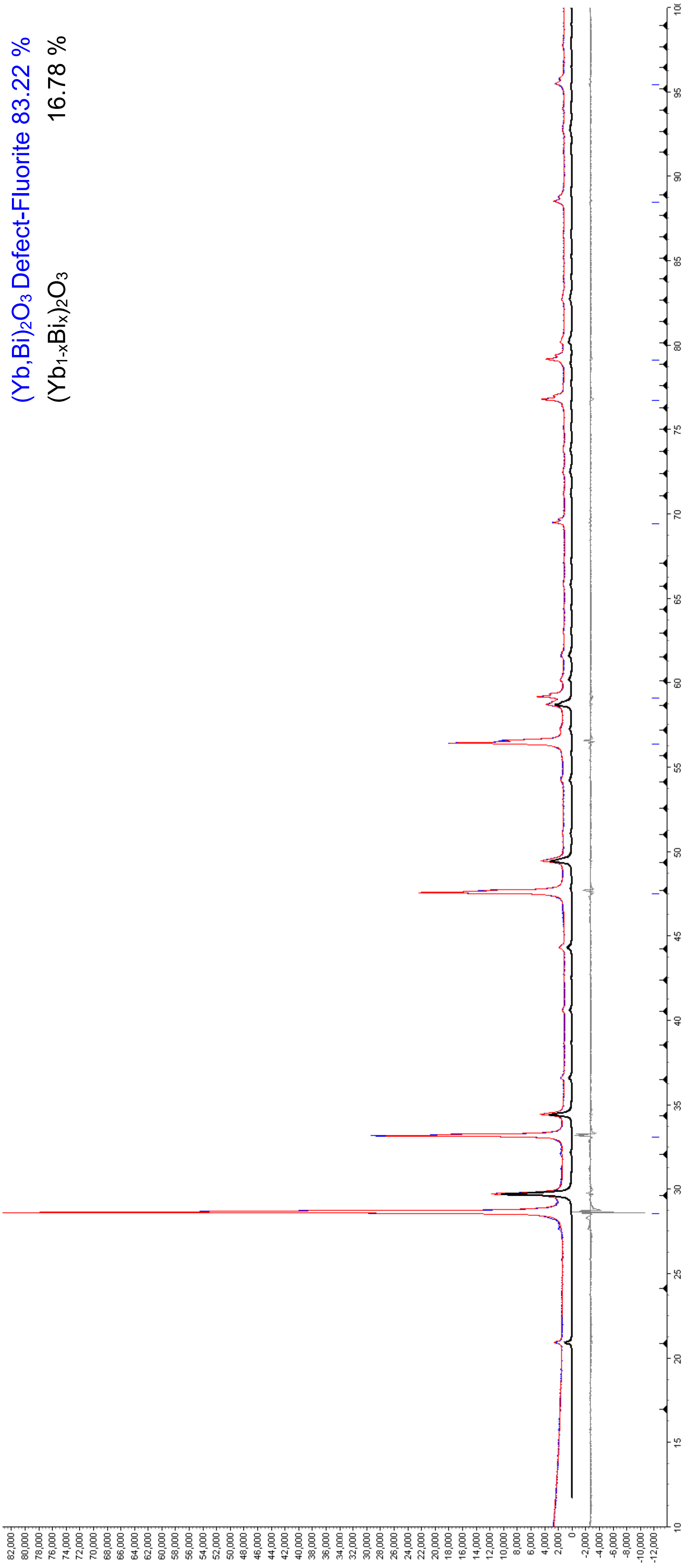

Figure 36b: XRD pattern of BiYbO$_3$ after sintering.

$Bi_{0.98}Ca_{0.02}Yb_{0.98}Zr_{0.02}O_3$ – Calcinated

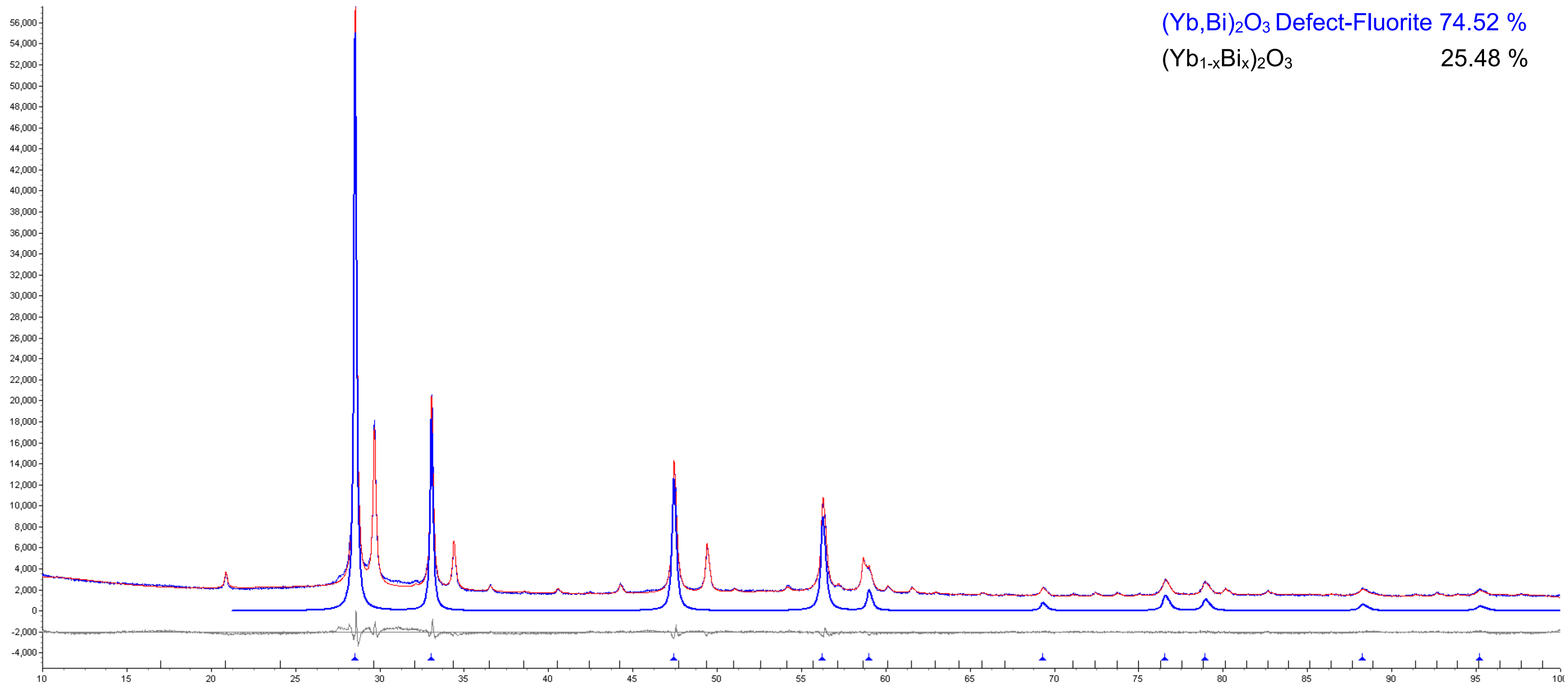

Figure 37a: XRD pattern of calcinated powder of BCYZ2.

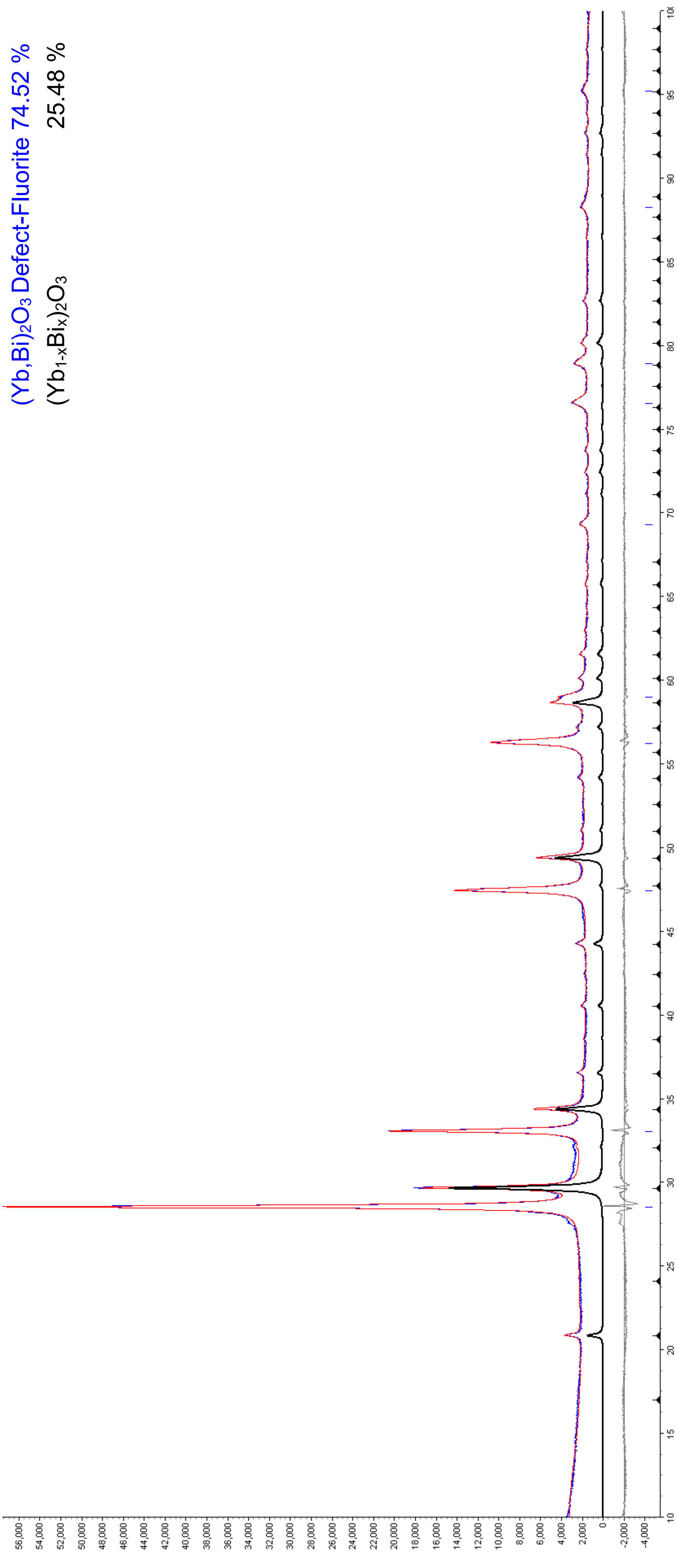

Figure 38b: XRD pattern of calcinated powder of BCYZ2.

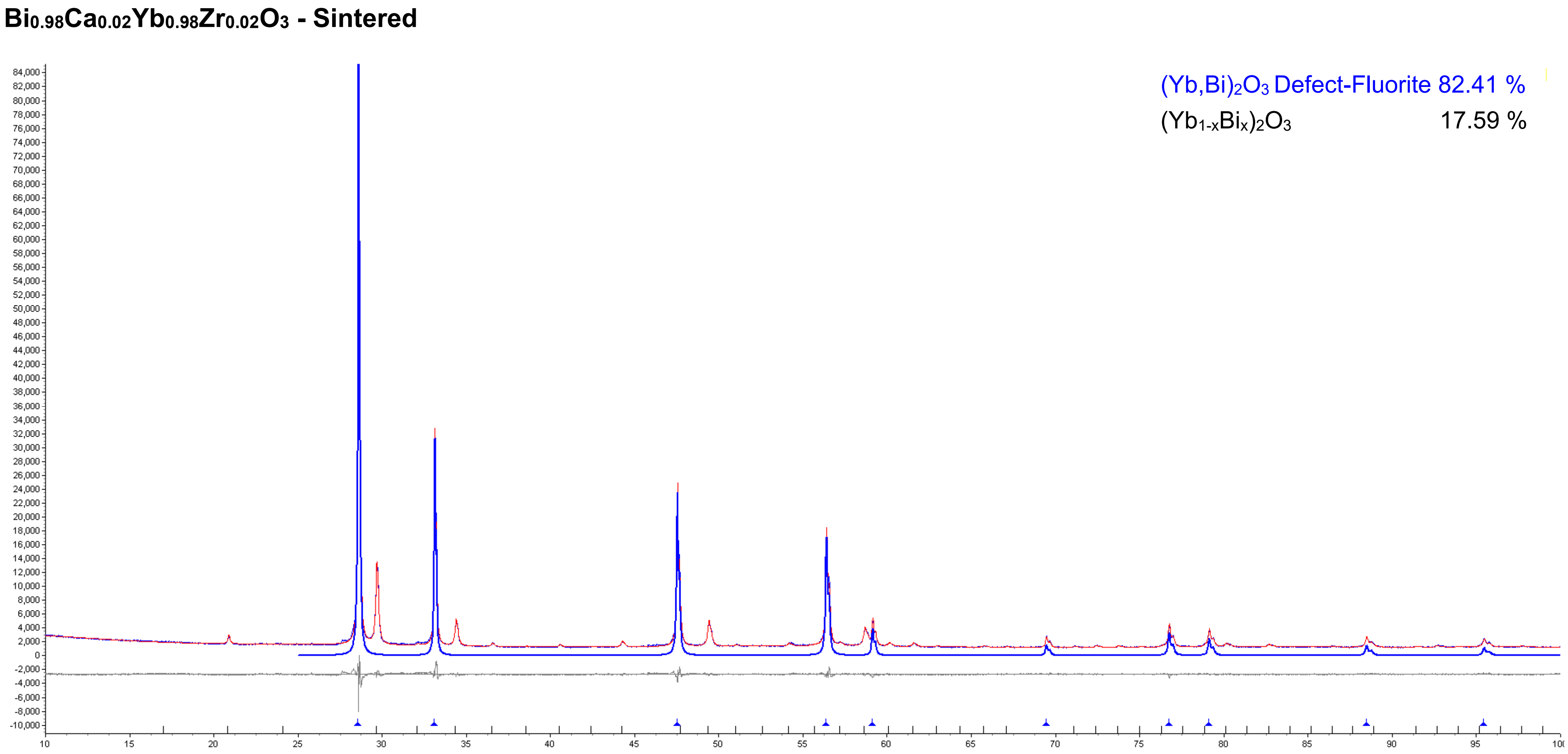

Figure 39a: XRD pattern of BCYZ2 after sintering.

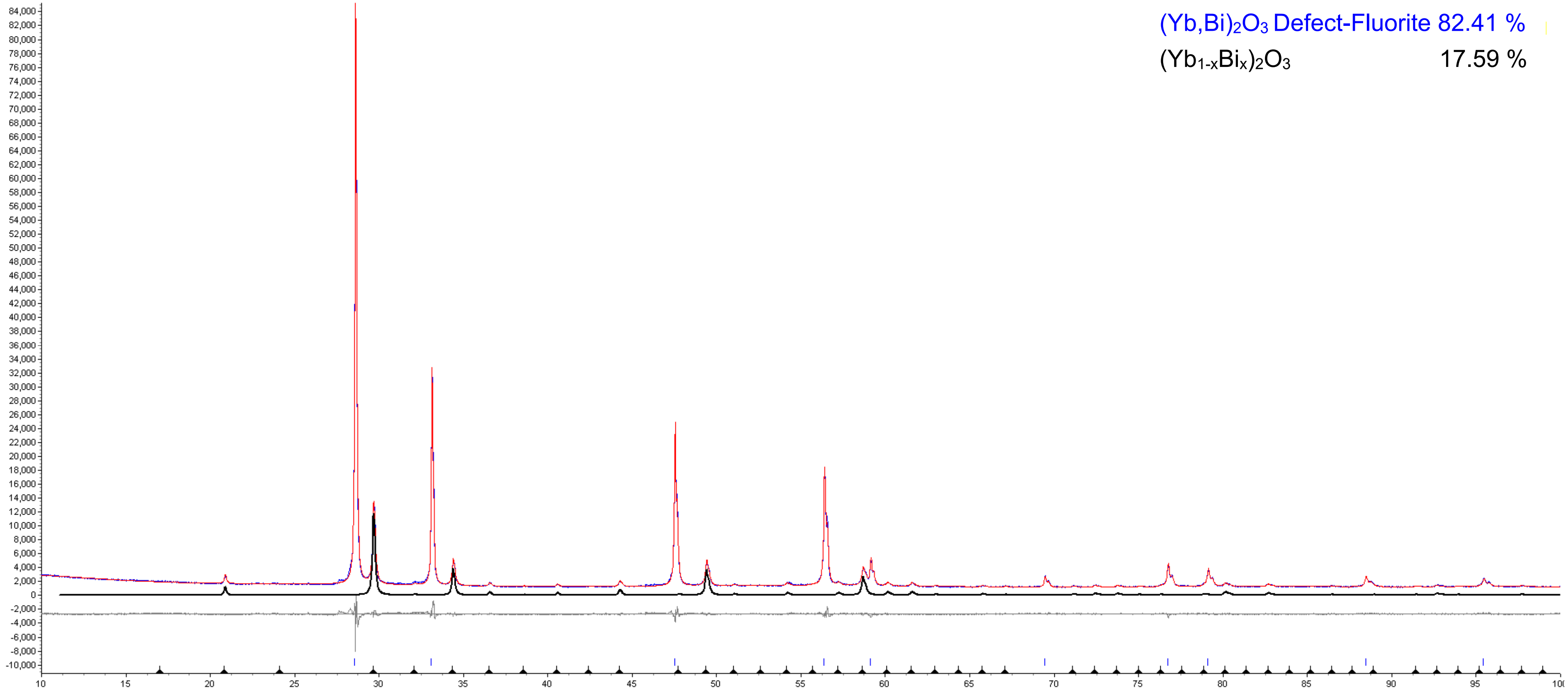

Figure 40b: XRD pattern of BCYZ2 after sintering.

$Bi_{0.90}Ca_{0.10}Yb_{0.90}Zr_{0.10}O_3$ – Calcinated

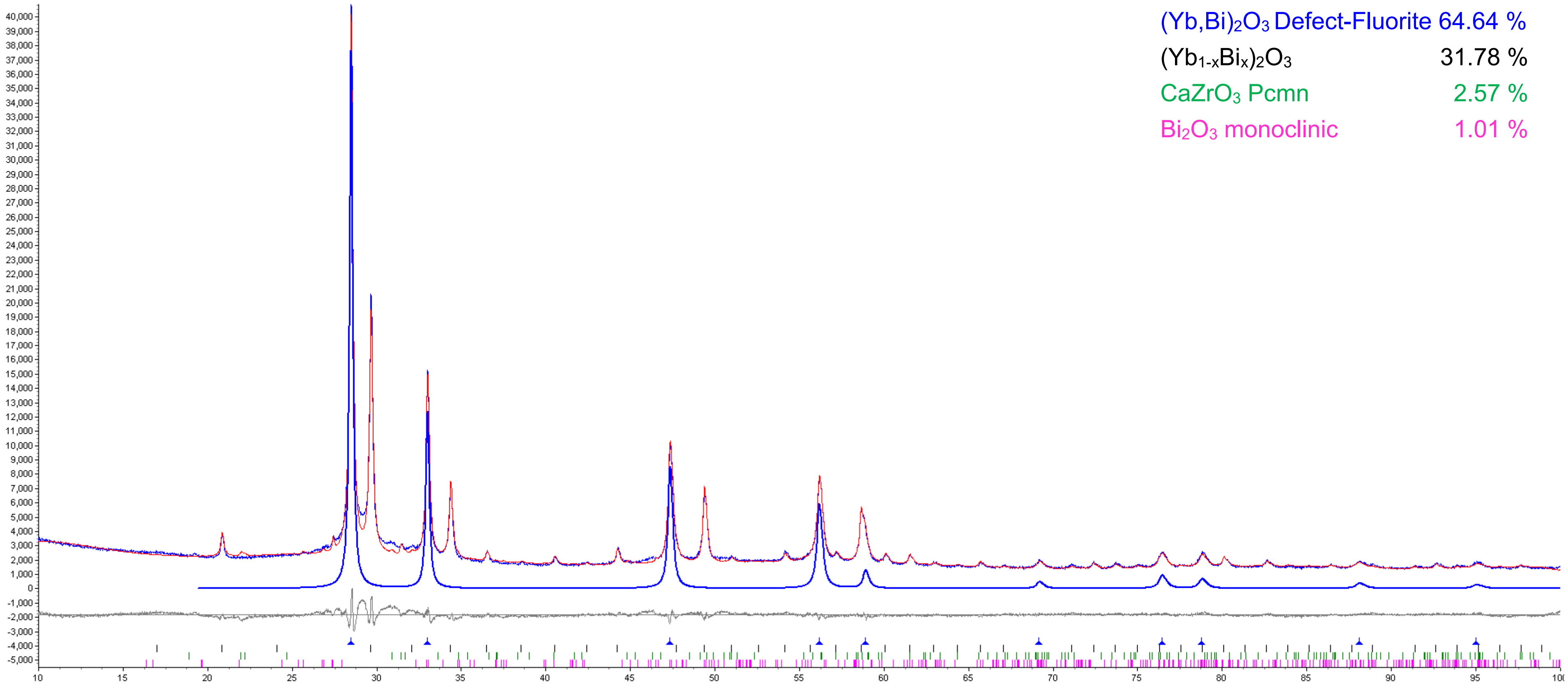

Figure 41a: XRD pattern of calcinated powder of BCYZ10.

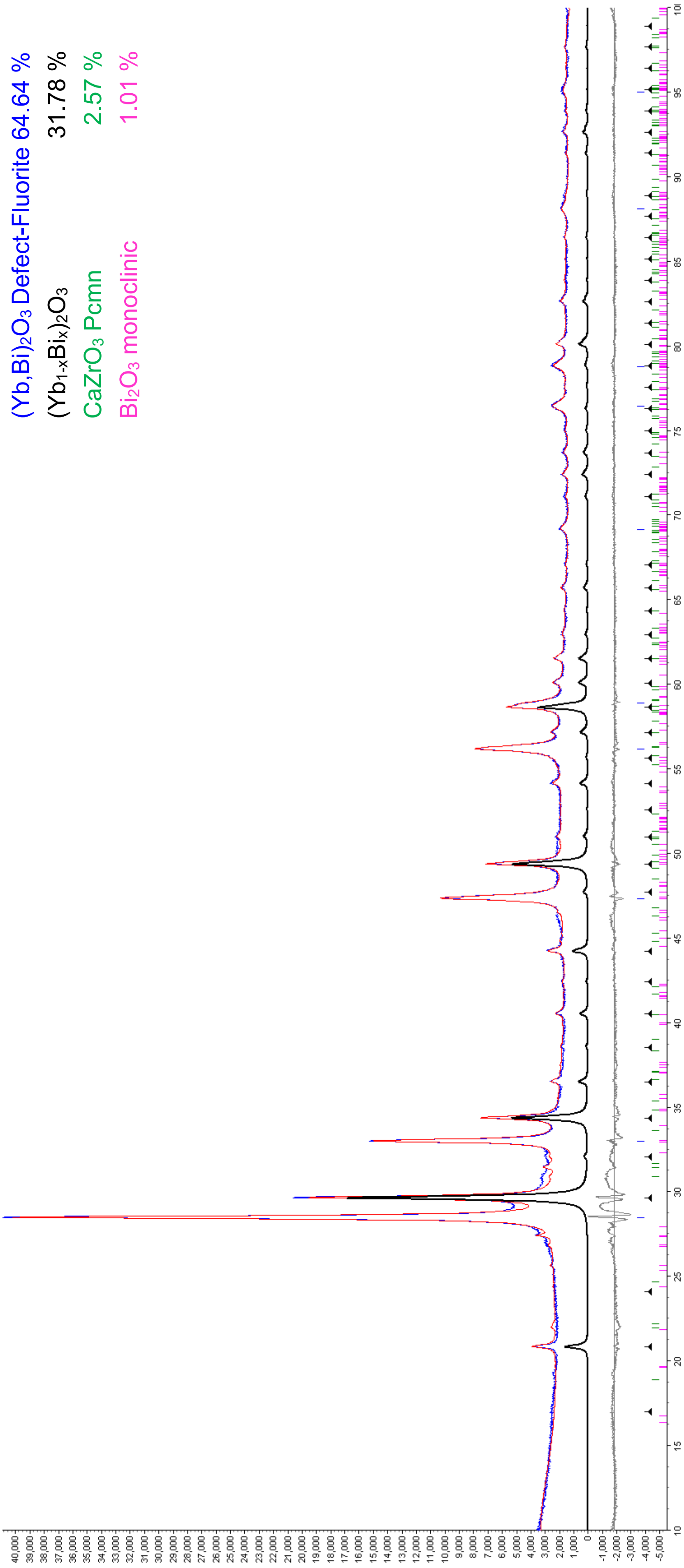

Figure 42b: XRD pattern of calcinated powder of BCYZ10.

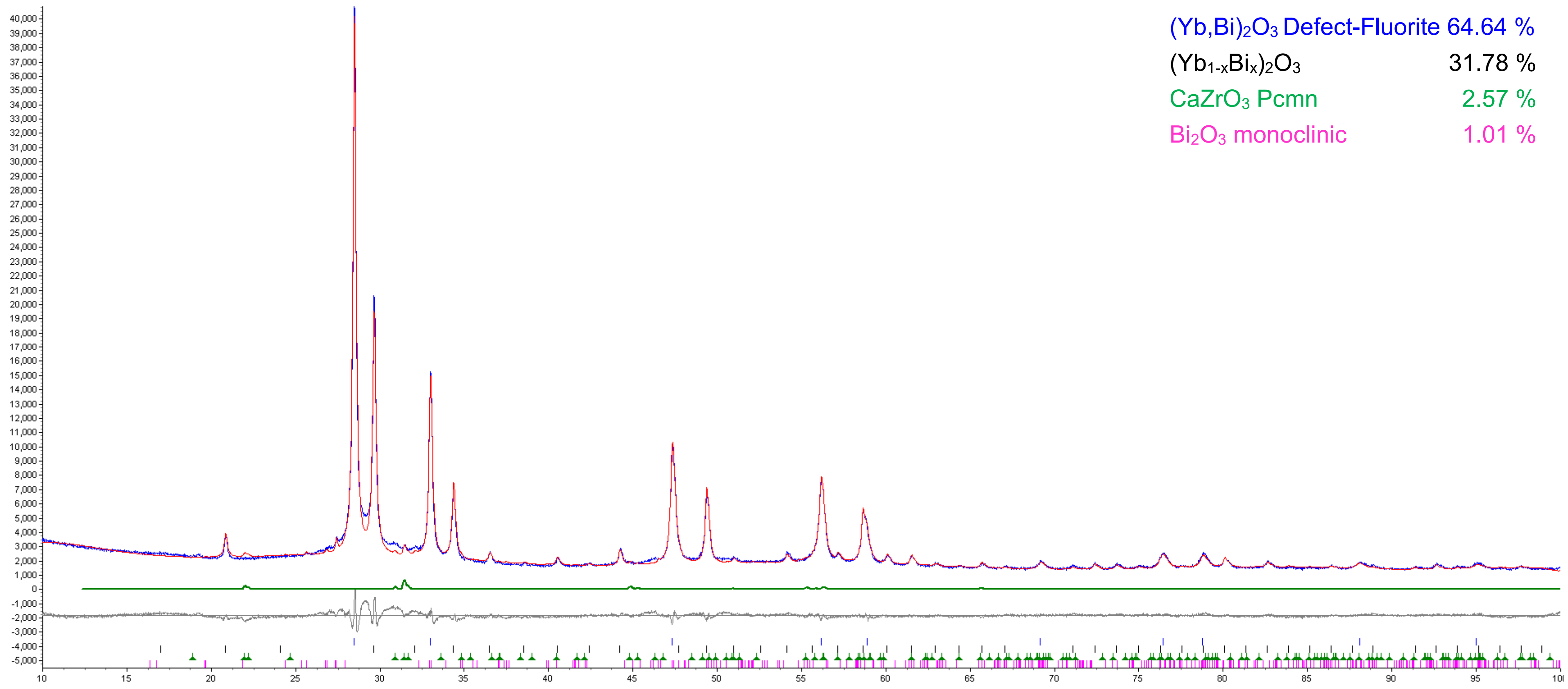

Figure 43c: XRD pattern of calcinated powder of BCYZ10.

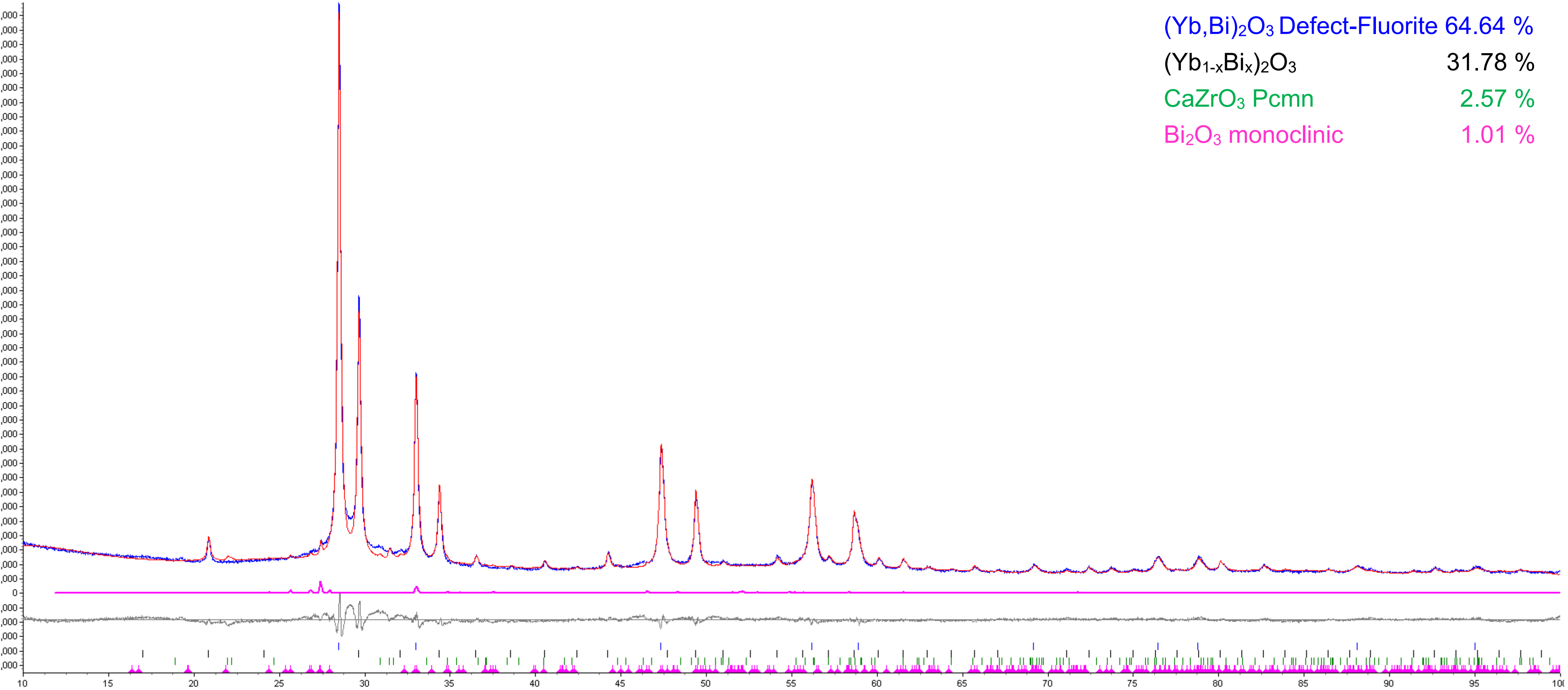

Figure 44d: XRD pattern of calcinated powder of BCYZ10.

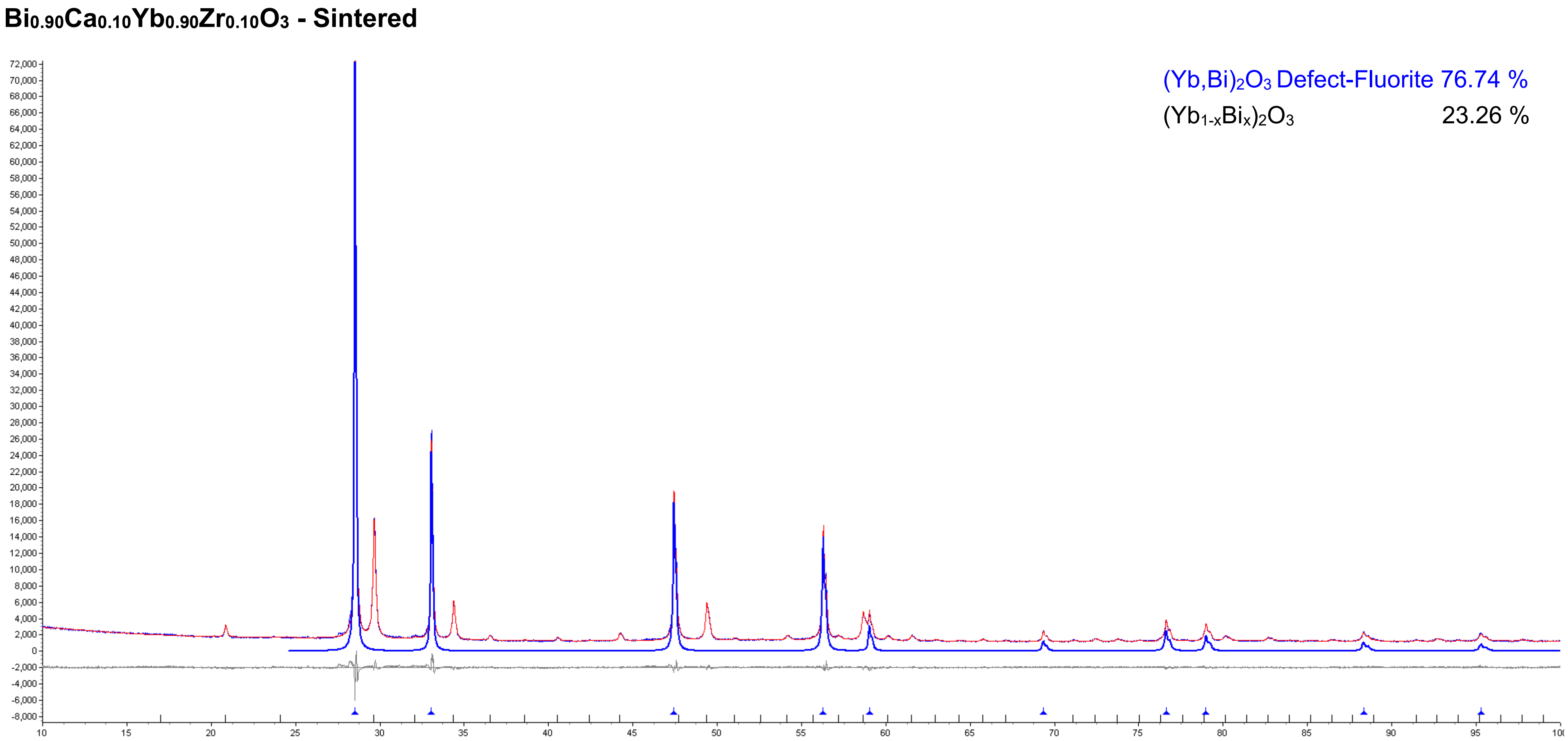

Figure 45a: XRD pattern of BCYZ10 after sintering.

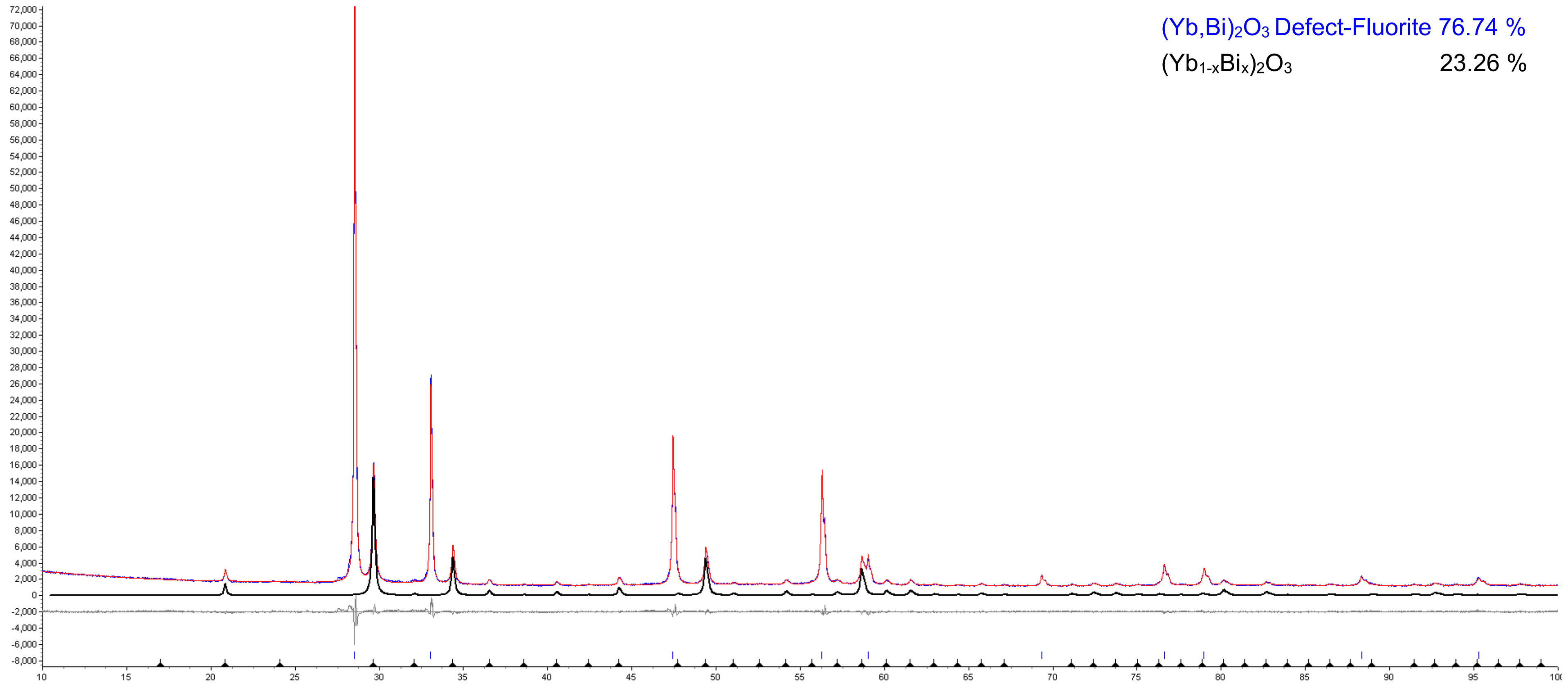

Figure 46b: XRD pattern of BCYZ10 after sintering.

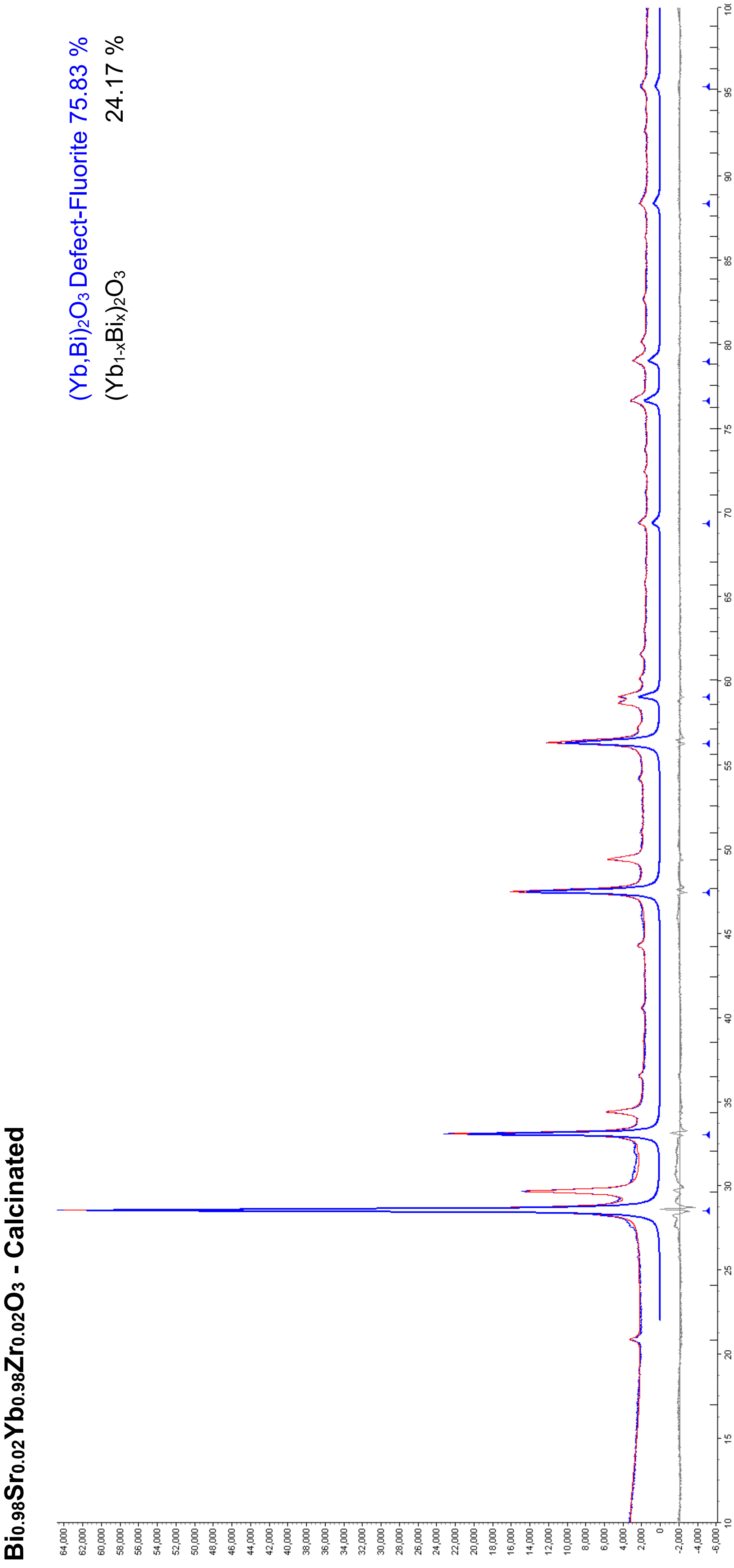

Figure 47a: XRD pattern of calcinated powder of BSYZ2.

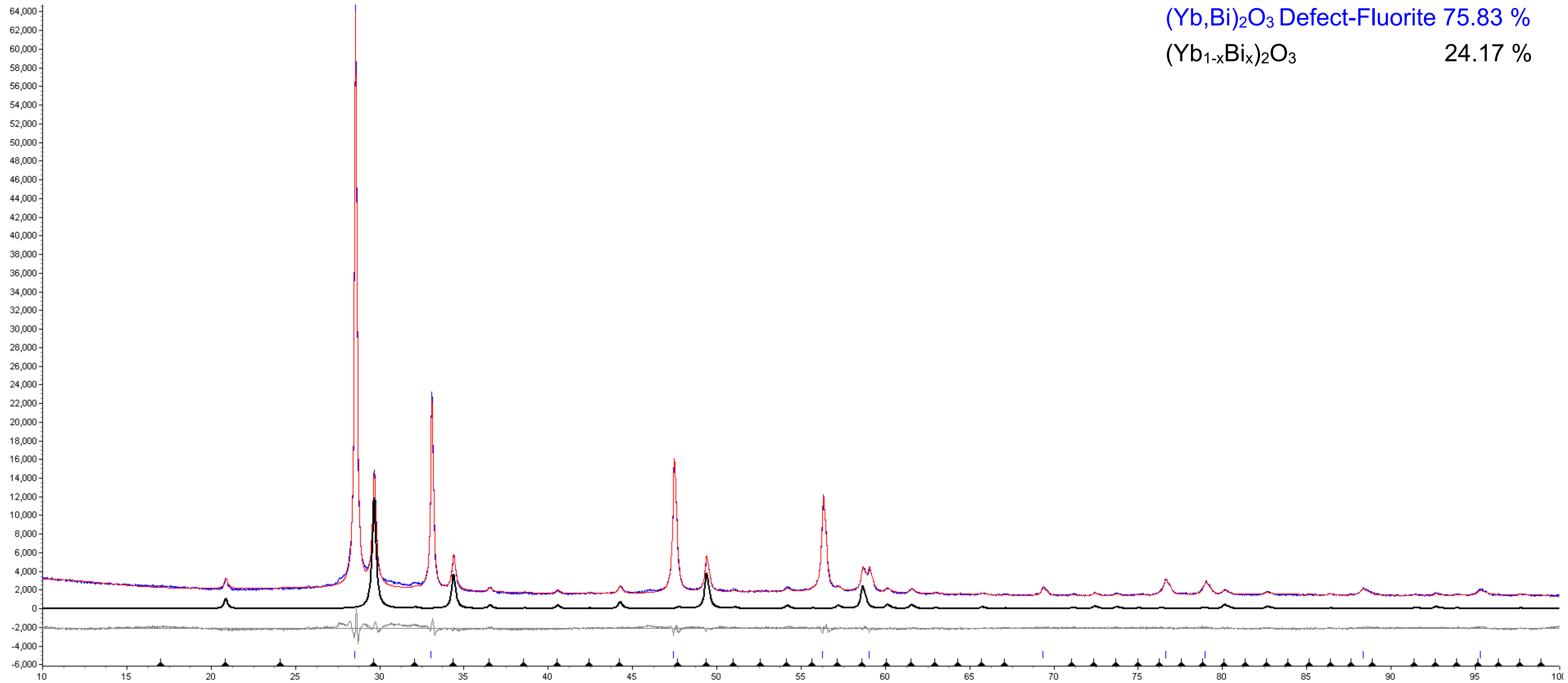

Figure 48b: XRD pattern of calcinated powder of BSYZ2.

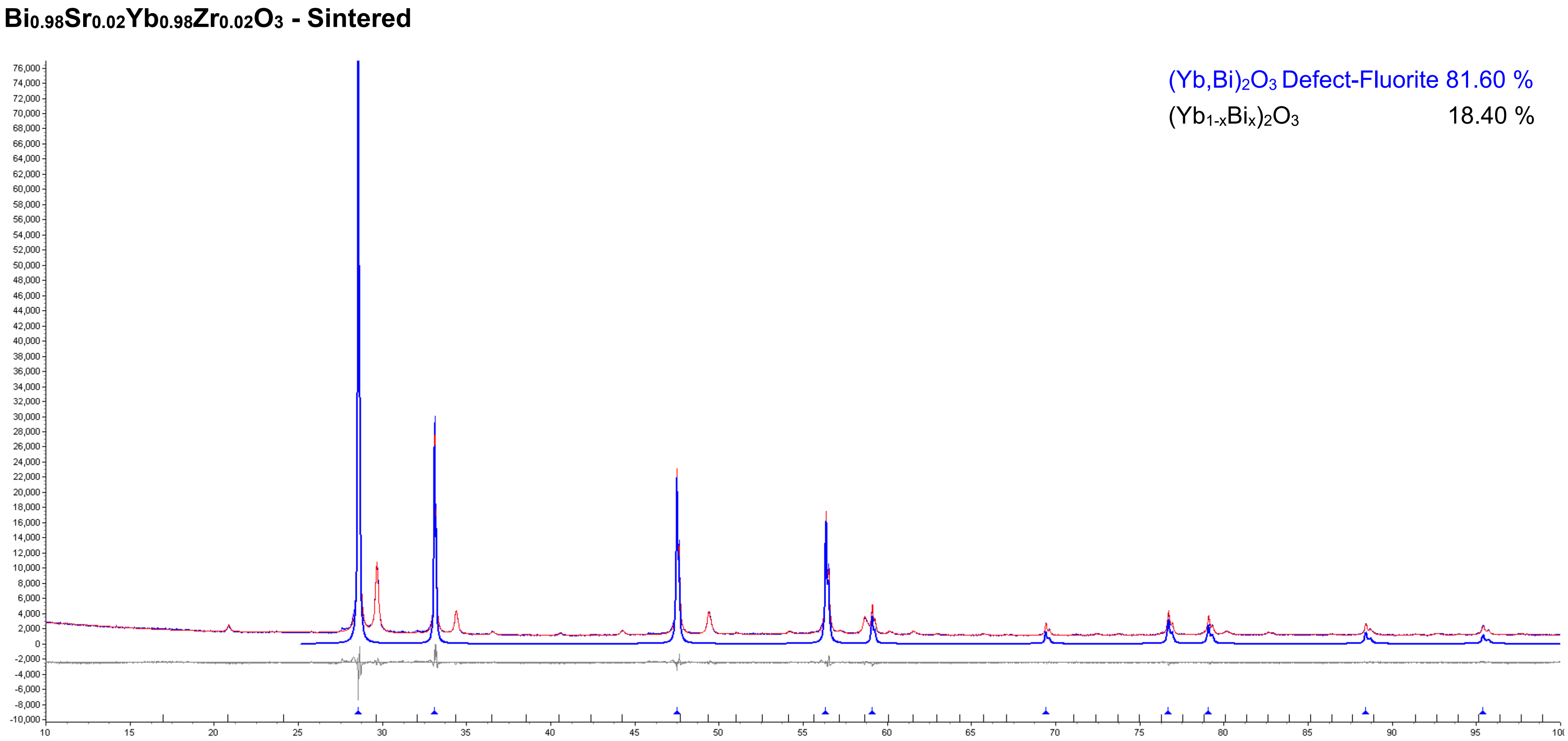

Figure 49a: XRD pattern of BSYZ2 after sintering.

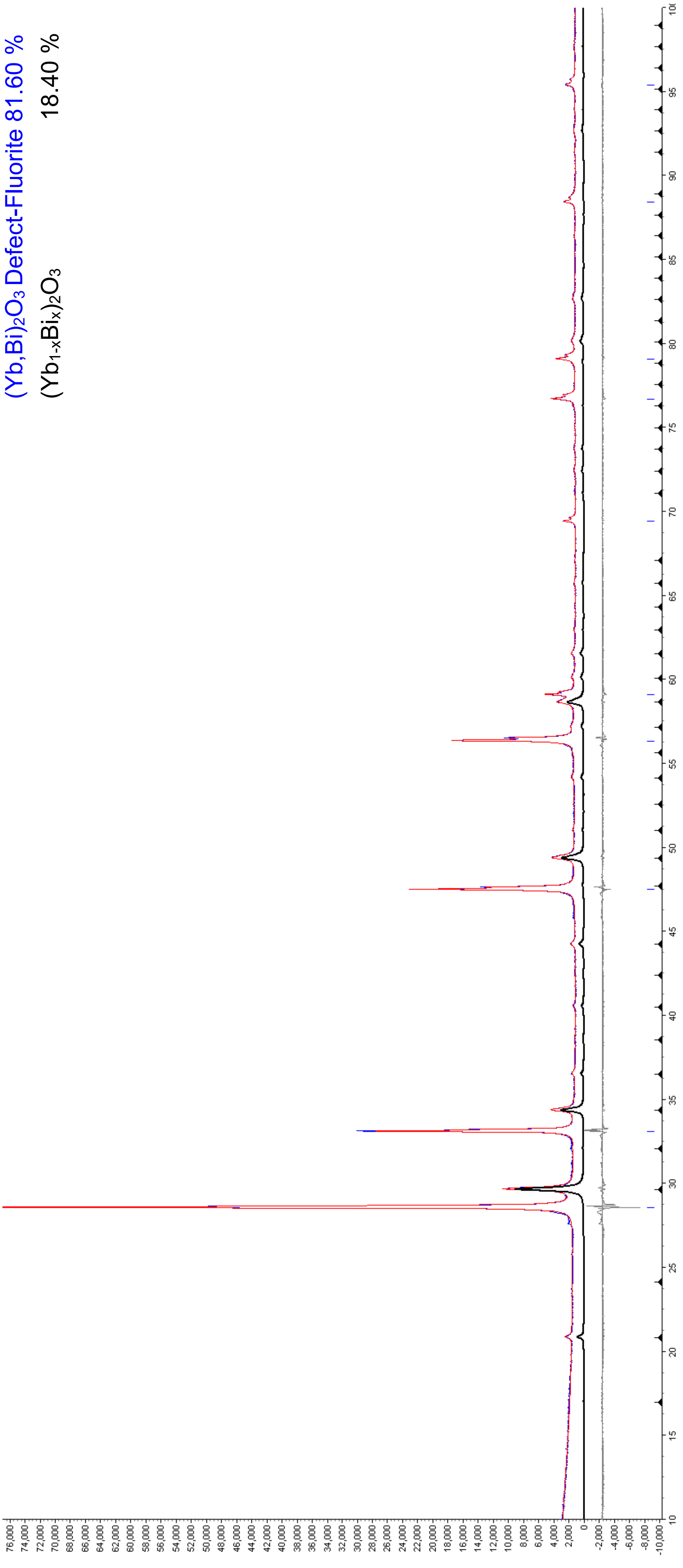

Figure 50b: XRD pattern of BSYZ2 after sintering.

$Bi_{0.90}Sr_{0.10}Yb_{0.90}Zr_{0.10}O_3$ – Calcinated

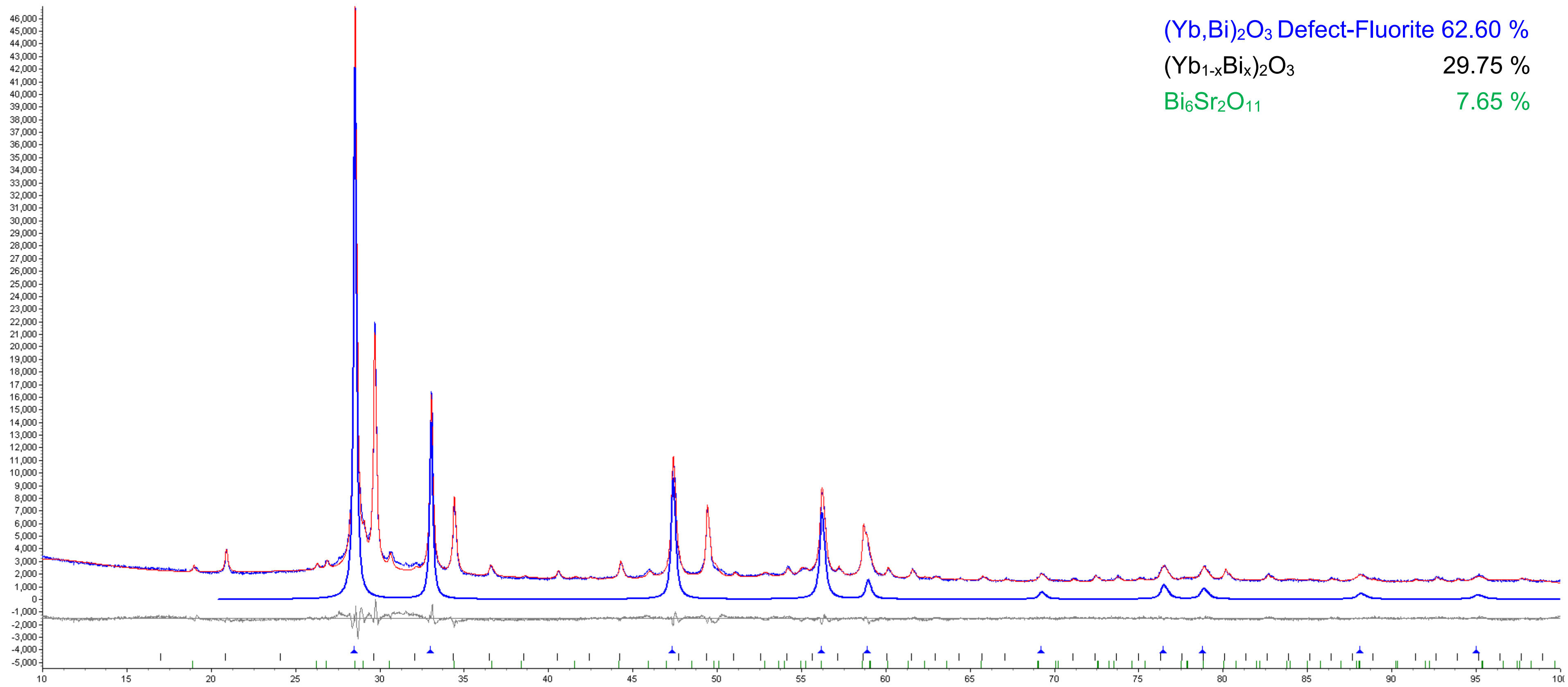

Figure 51a: XRD pattern of calcinated powder of BSYZ10.

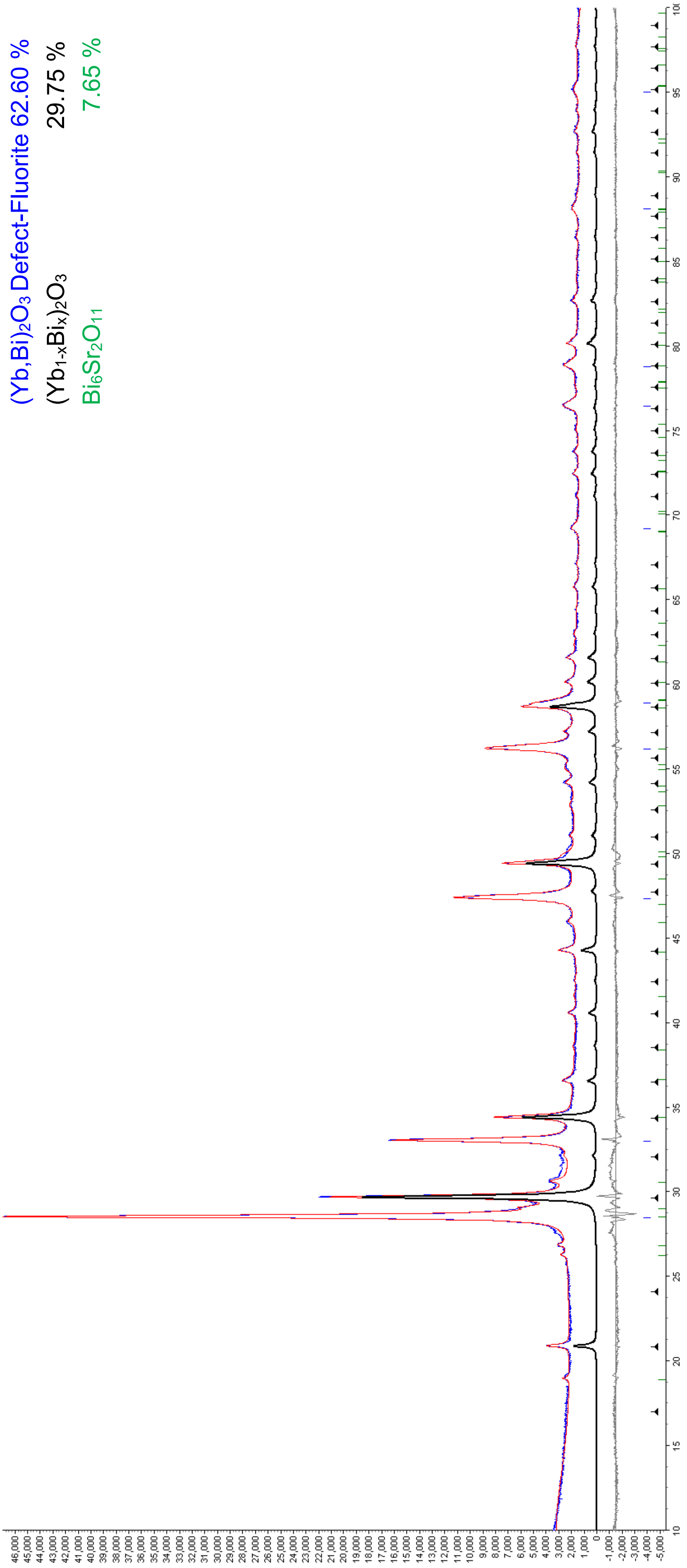

Figure 52b: XRD pattern of calcinated powder of BSYZ10.

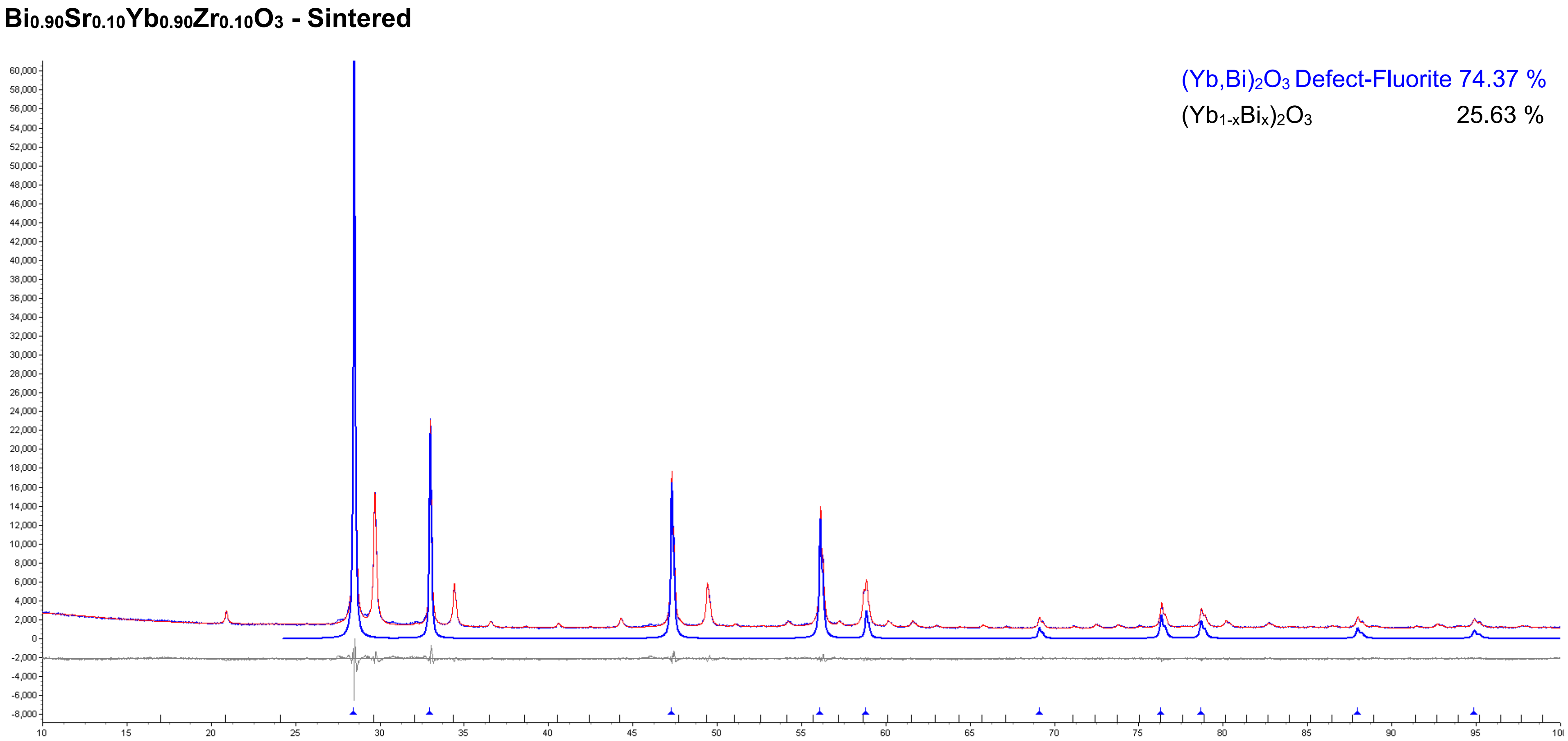

Figure 53a: XRD pattern of BSYZ10 after sintering.

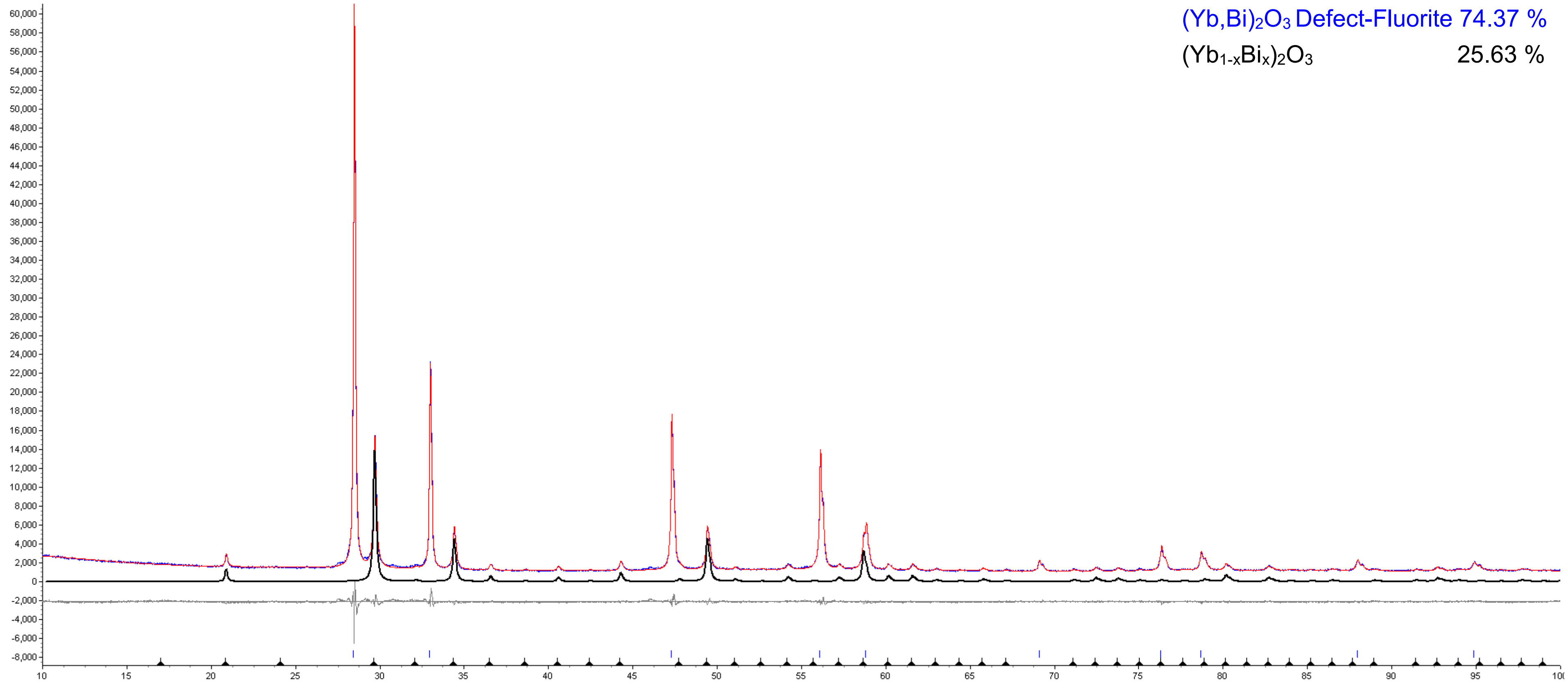

Figure 54b: XRD pattern of BSYZ10 after sintering.

(Bi$_{0.9}$La$_{0.1}$)YbO$_3$ – Calcinated

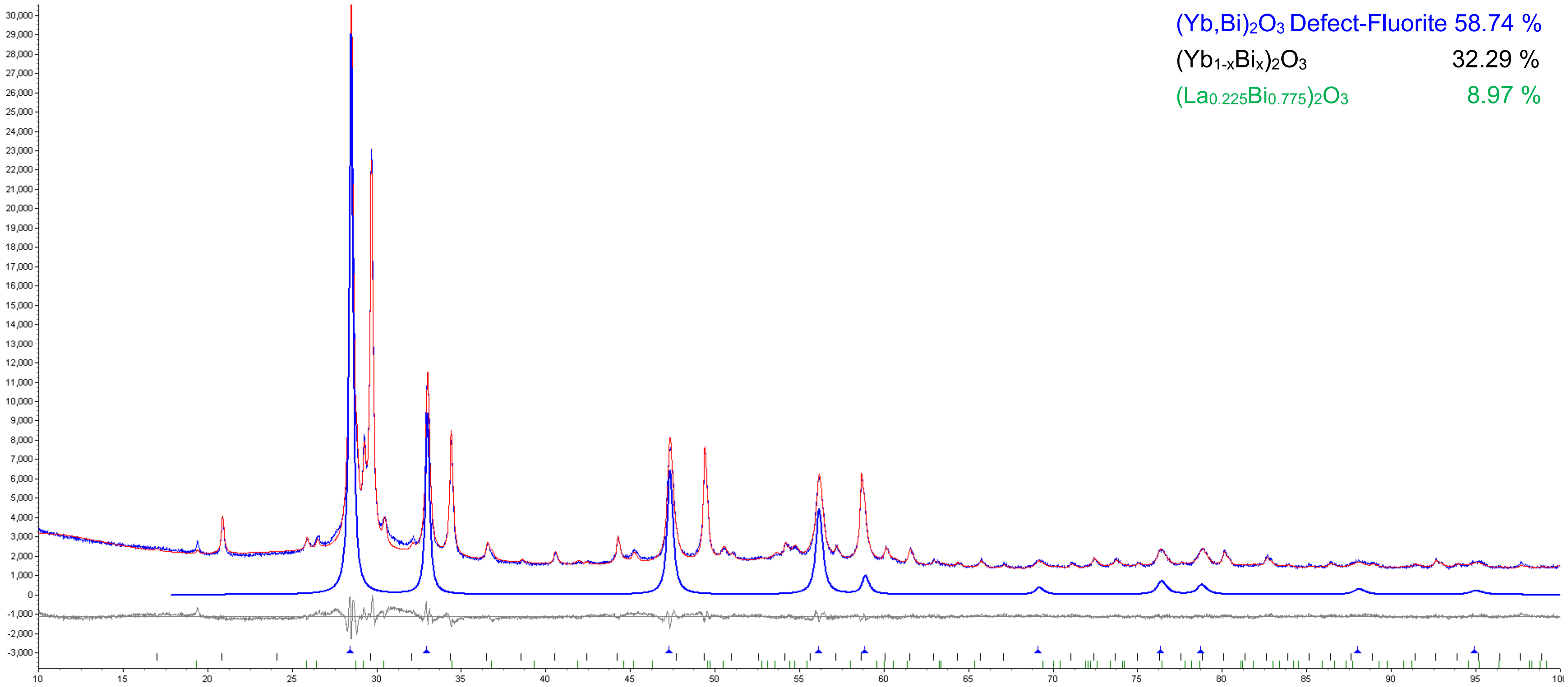

Figure 55a: XRD pattern of calcinated powder of BLY10.

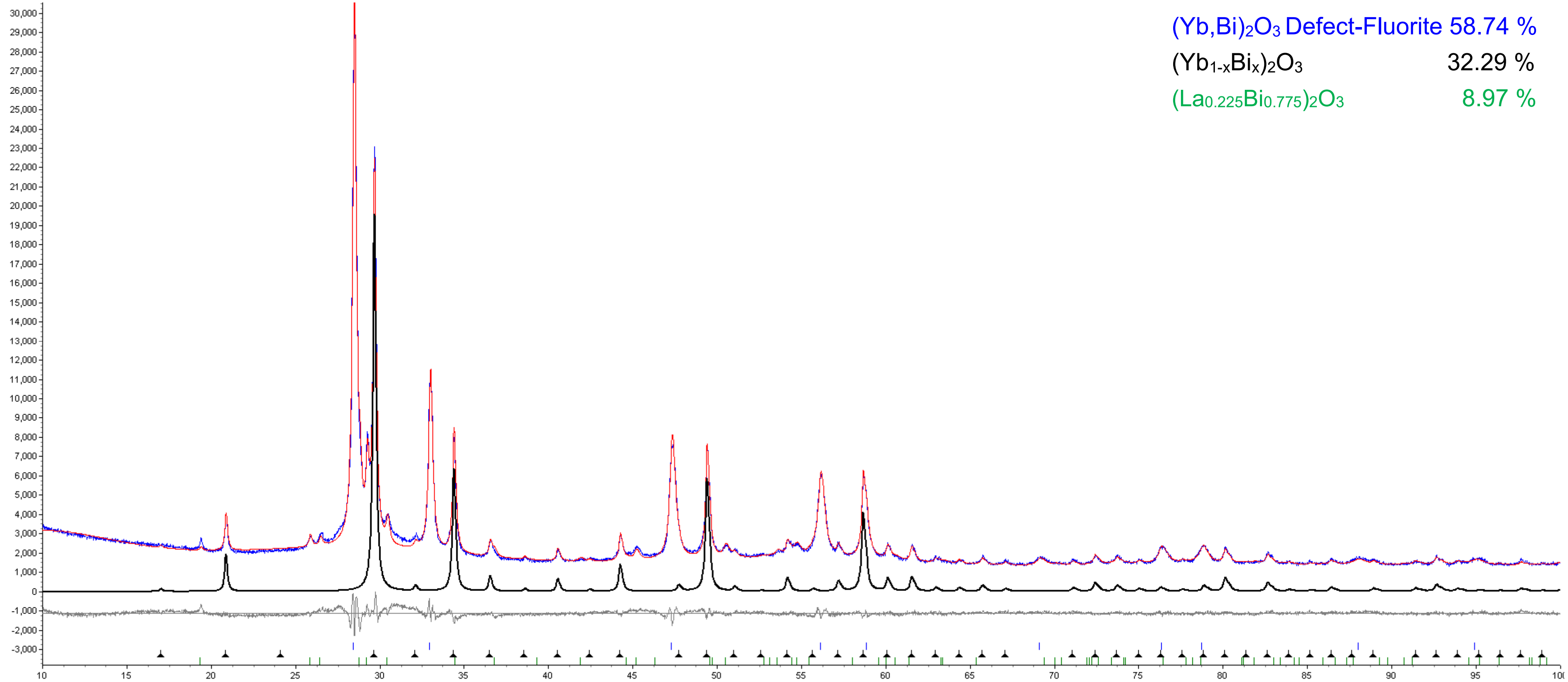

Figure 56b: XRD pattern of calcinated powder of BLY10.

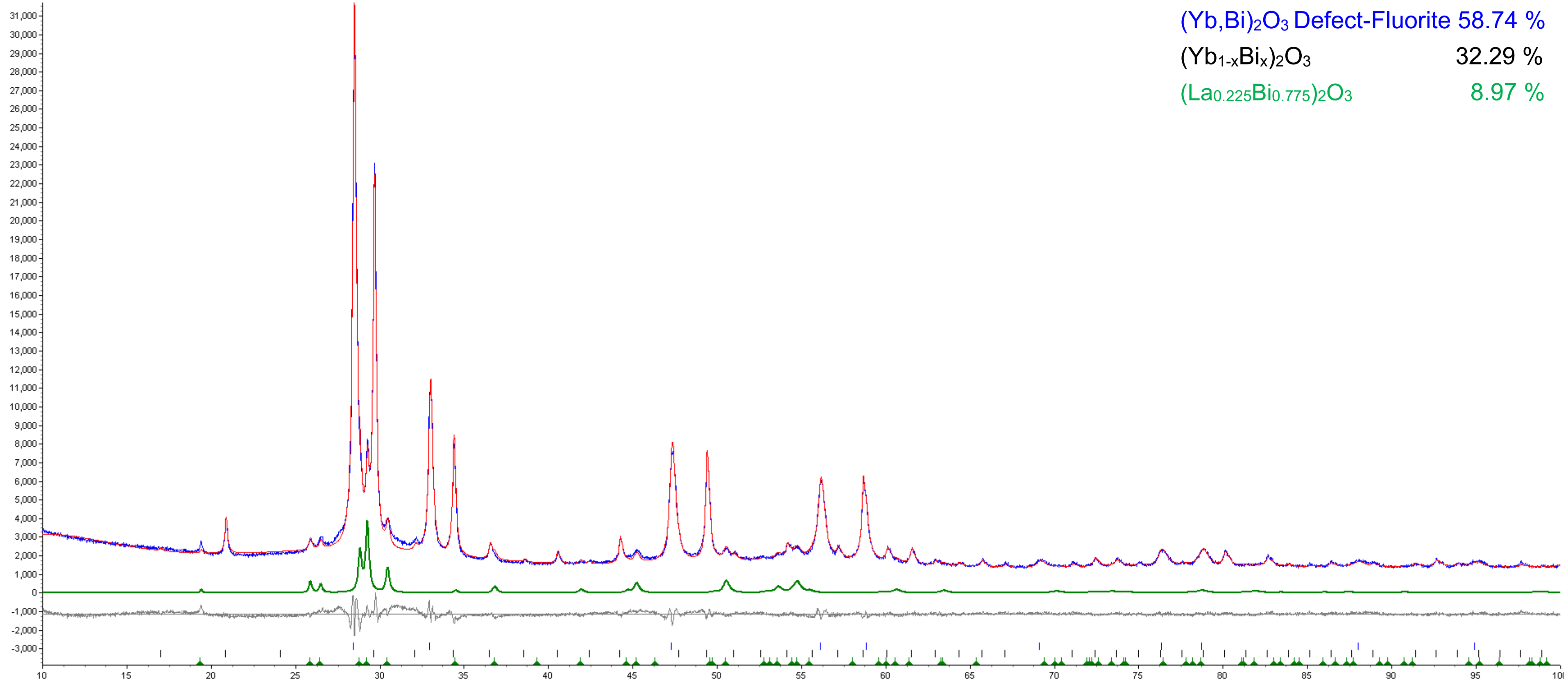

Figure 57c: XRD pattern of calcinated powder of BLY10.

(Bi$_{0.9}$La$_{0.1}$)YbO$_3$ – Sintered

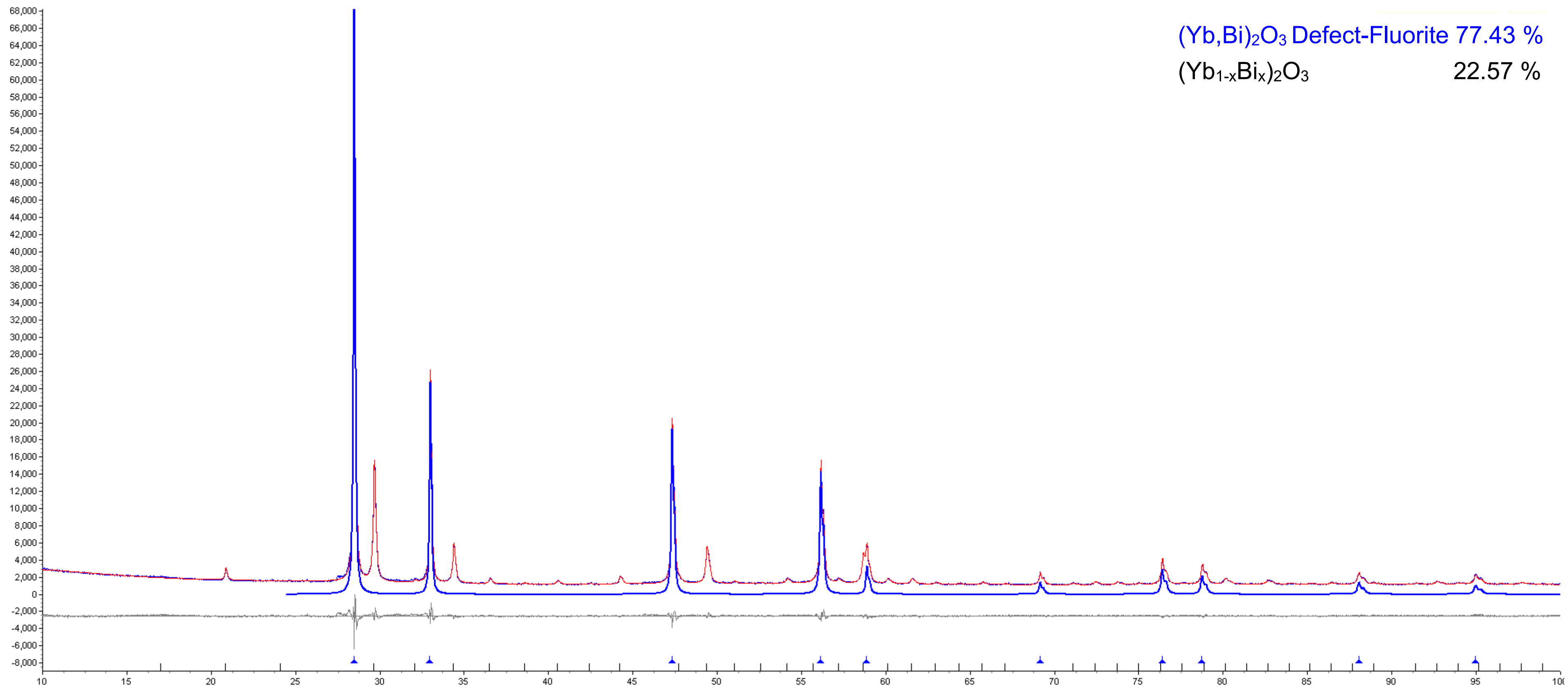

Figure 58: XRD pattern of BLY10 after sintering.

Appendix 3: XRD spectra of *x*LaYbO$_3$ – (1-*x*)CaZrO$_3$ and *x*LaYbO$_3$ – (1-*x*)SrZrO$_3$.

The blue solid line represent the experimental data and the red line the calculated patterns. The vertical bars indicate the positions of the diffraction peaks. The black line at the bottom displays the difference between the experimental and calculated data.

$Ca_{0.90}La_{0.10}Zr_{0.90}Yb_{0.10}O_3$ – Calcinated

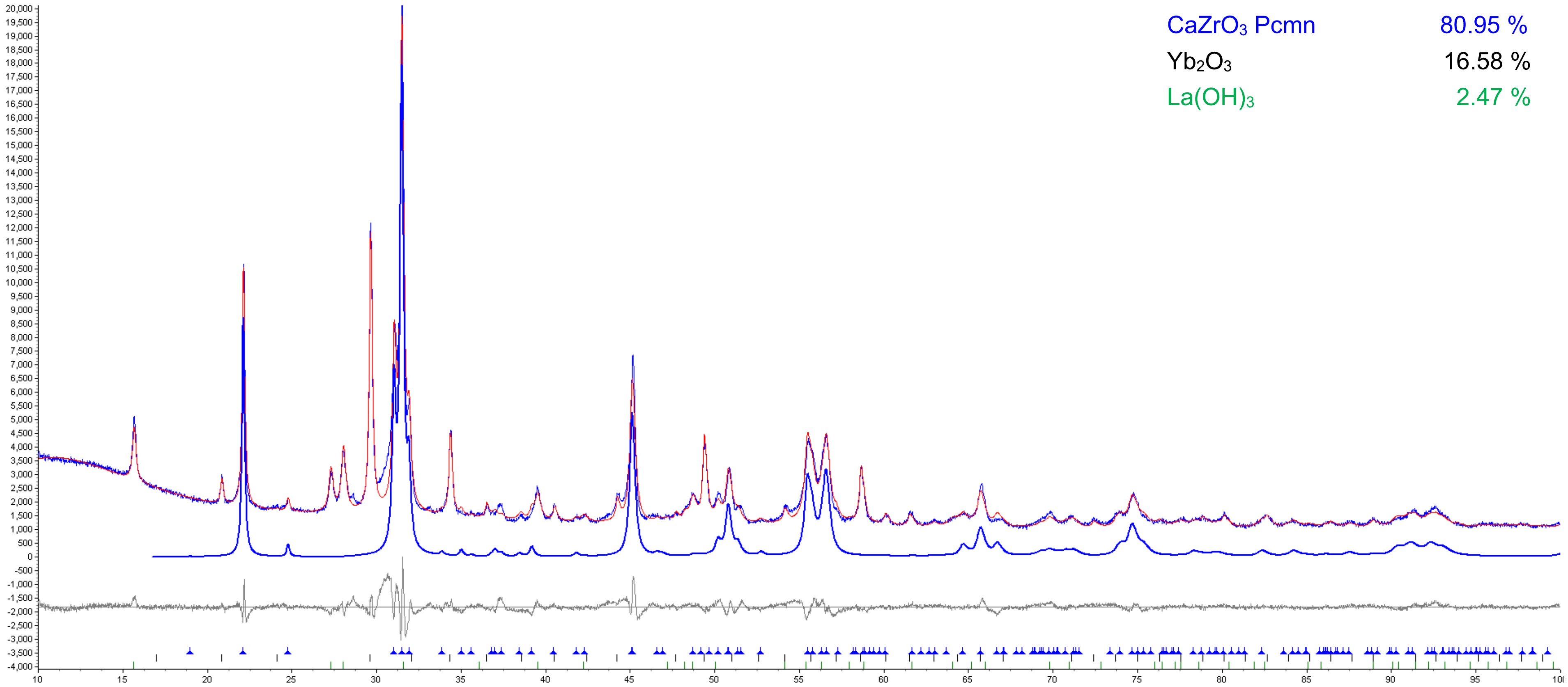

Figure 59a: XRD pattern of calcinated powder of CLZY10.

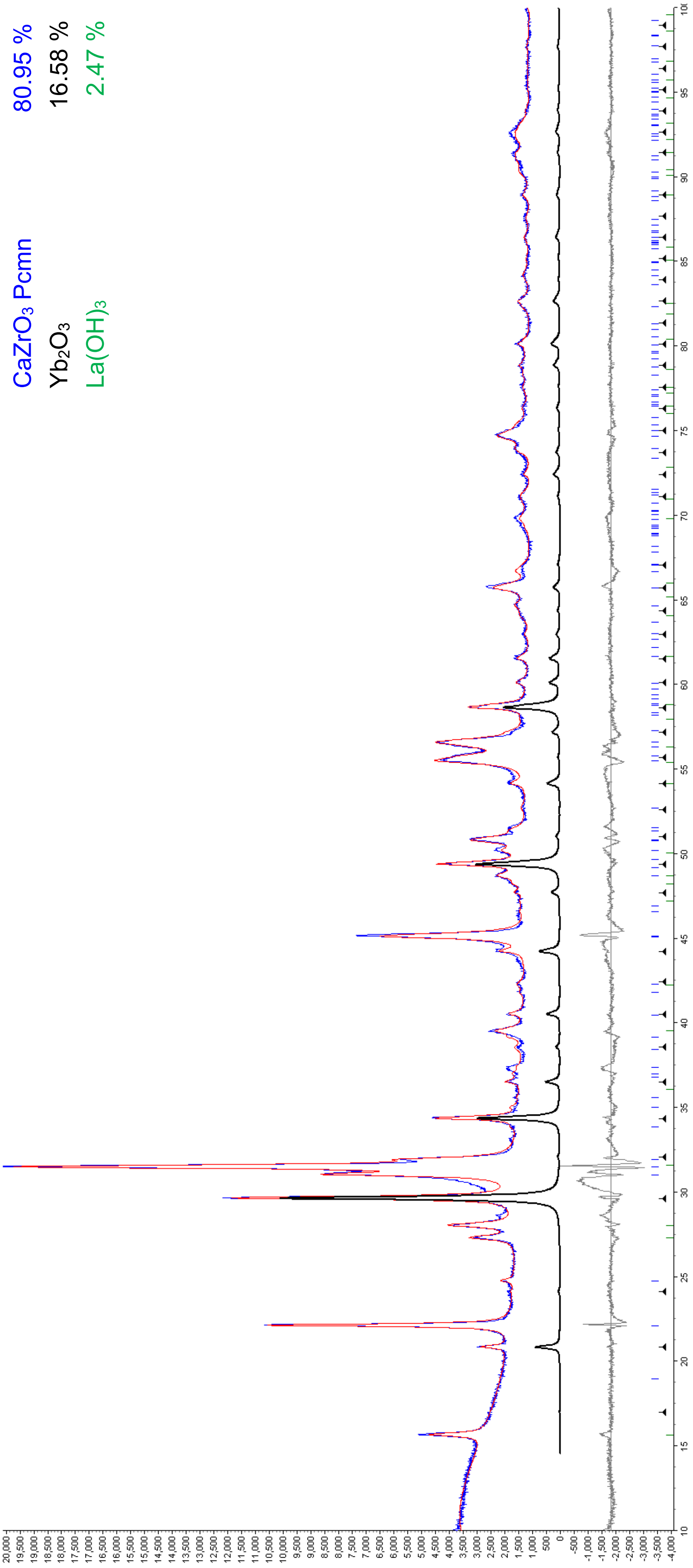

Figure 60b: XRD pattern of calcinated powder of CLZY10.

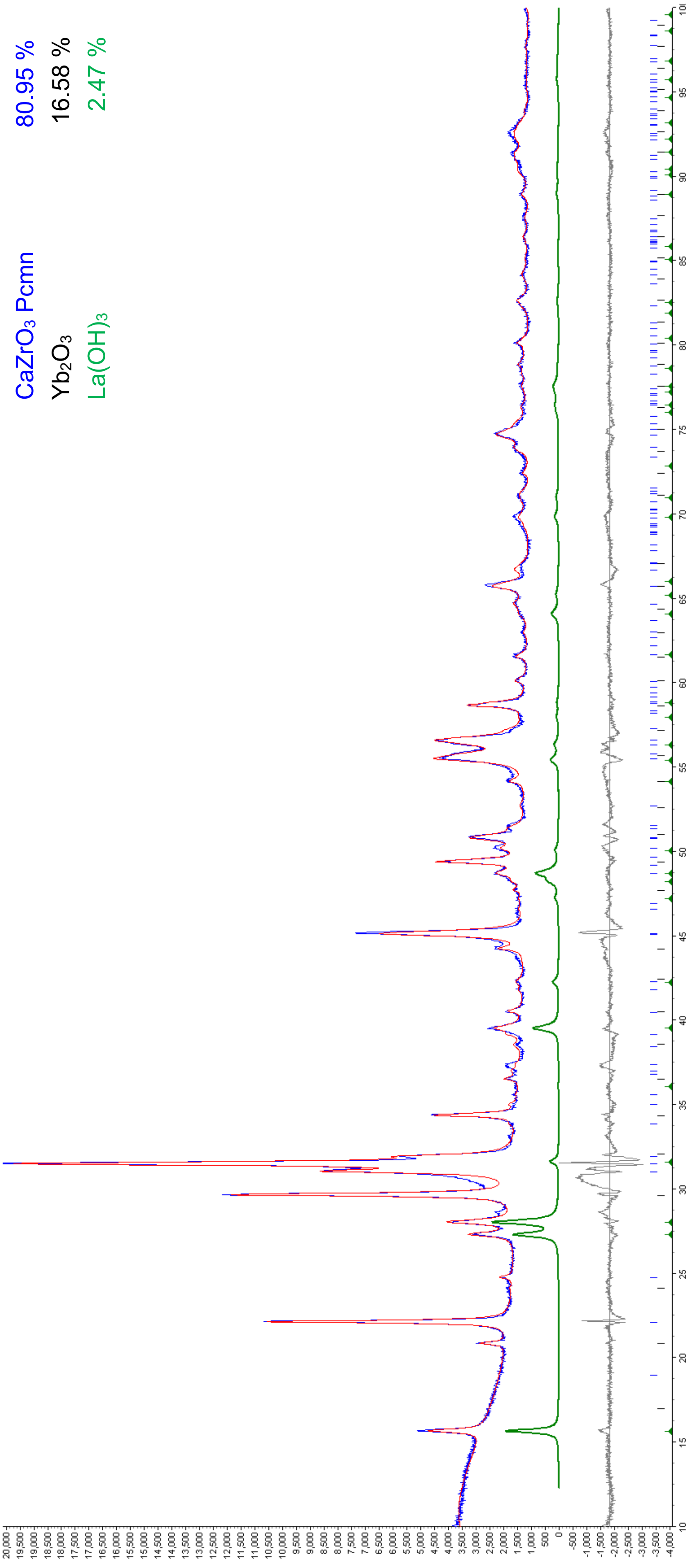

Figure 61c: XRD pattern of calcinated powder of CLZY10.

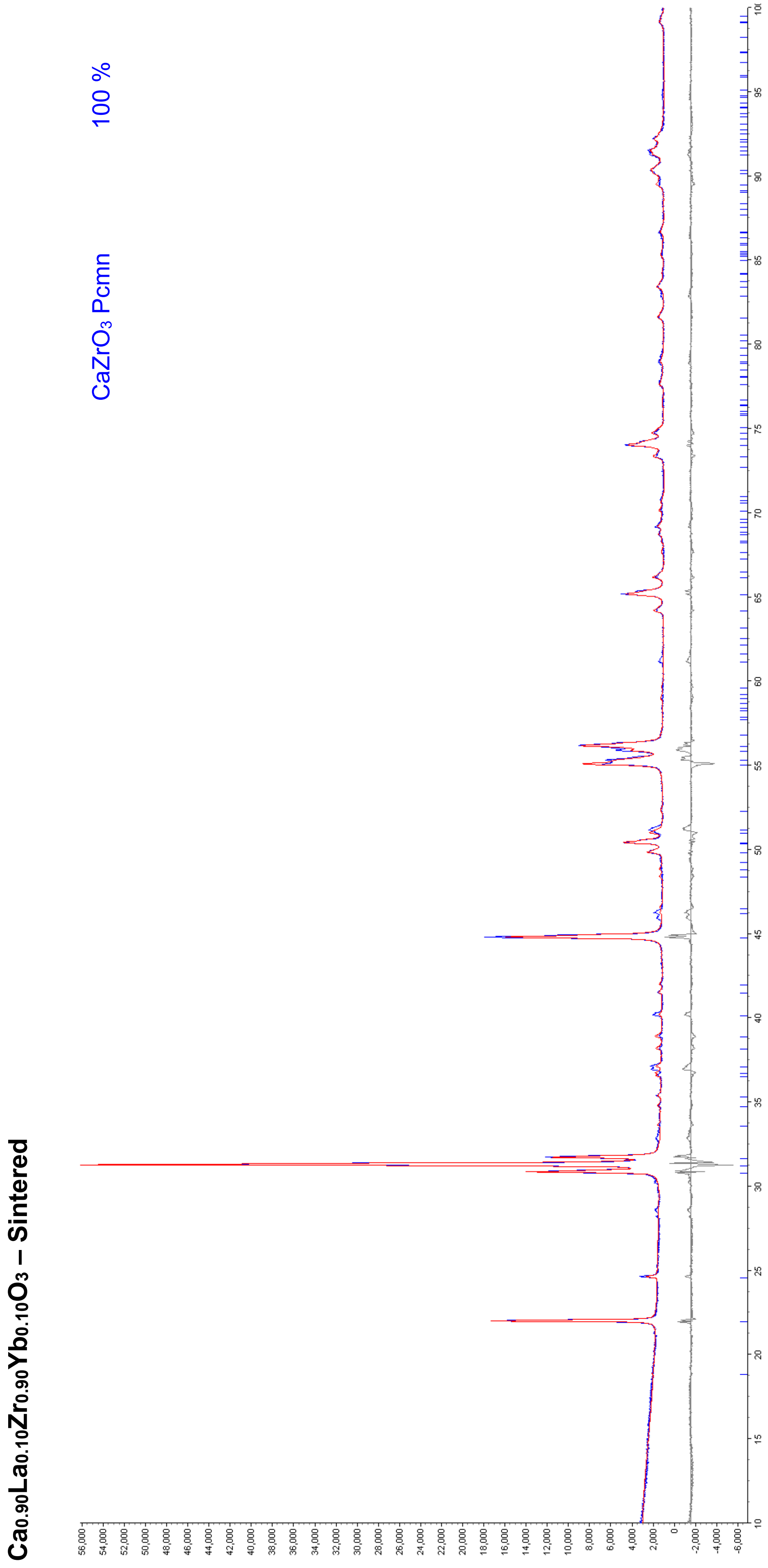

Figure 62: XRD pattern of CLZY10 after sintering.

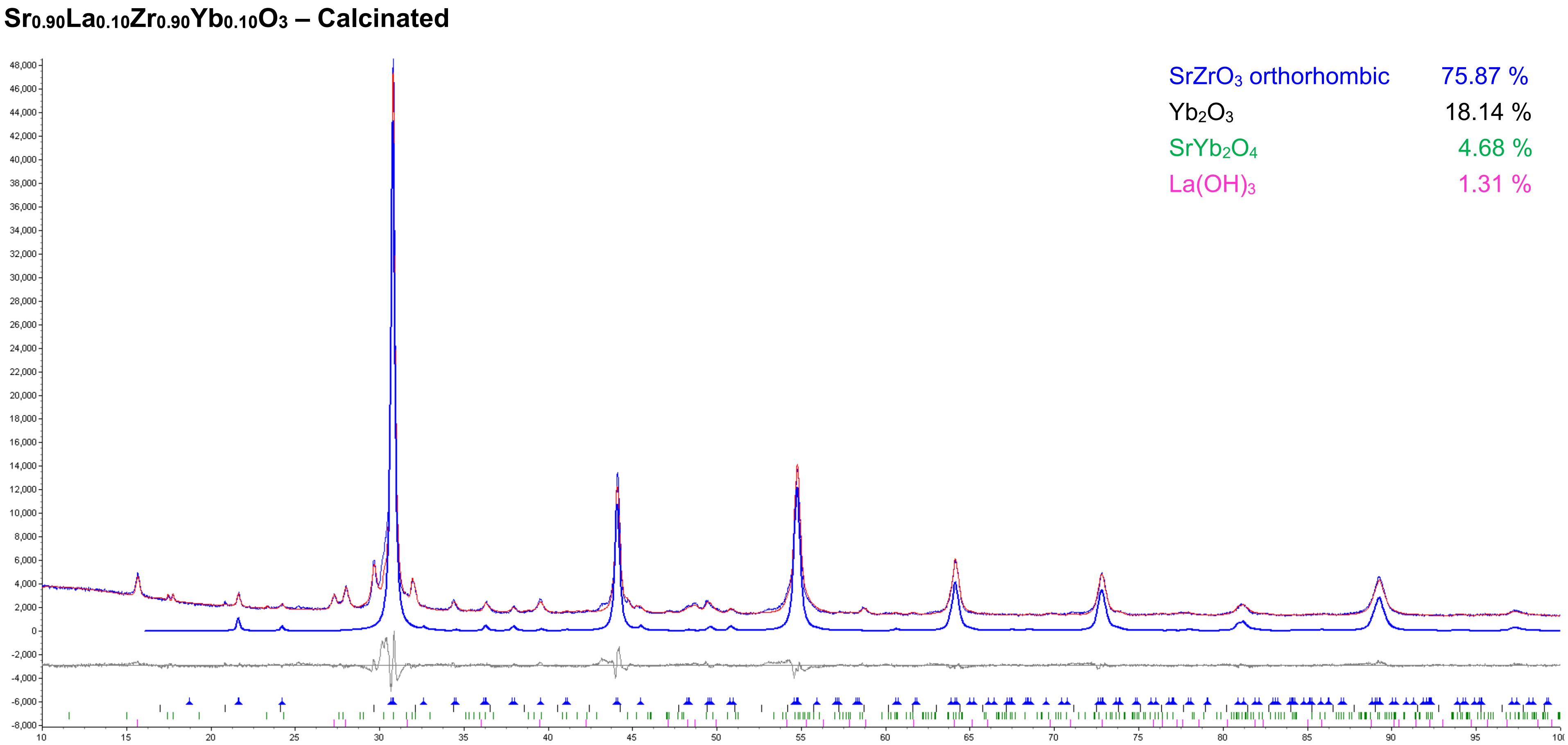

Figure 63a: XRD pattern of calcinated powder of SLZY10.

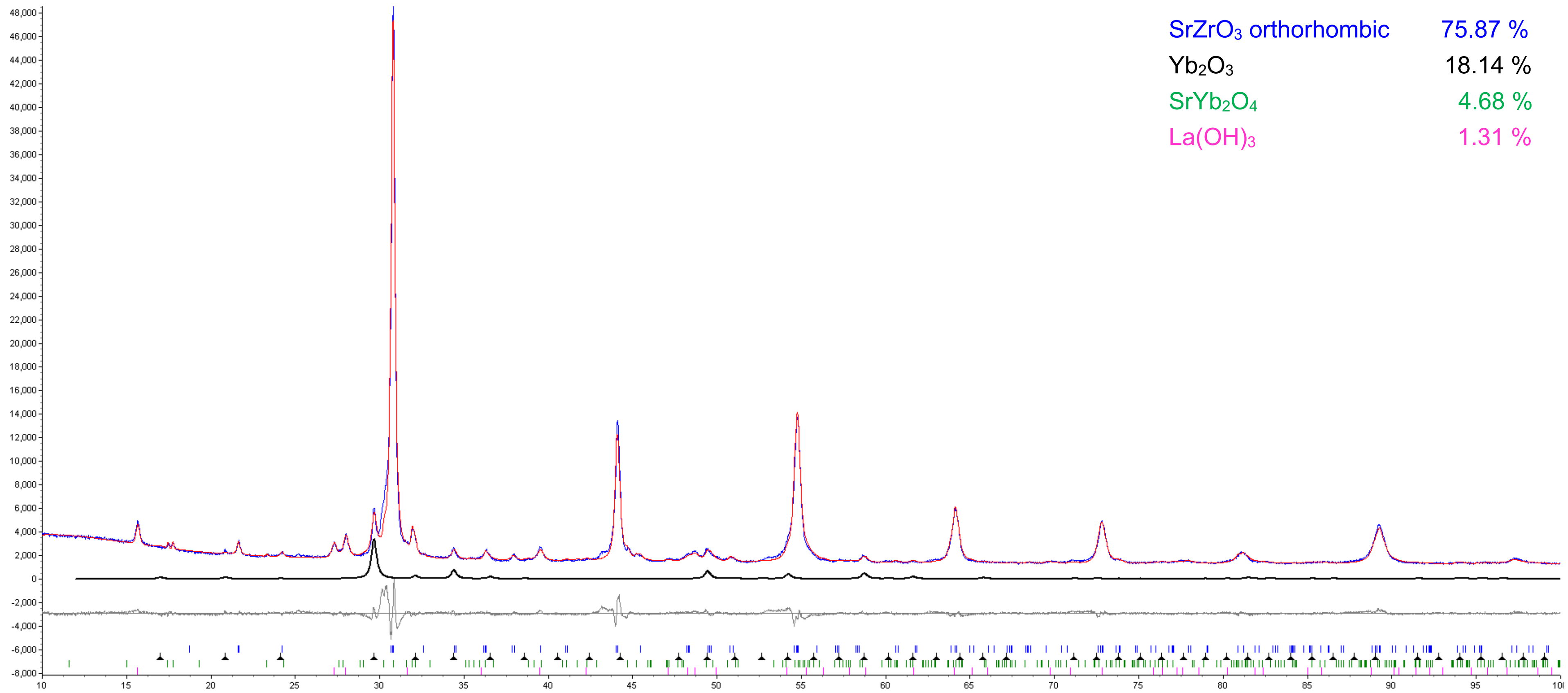

Figure 64b: XRD pattern of calcinated powder of SLZY10.

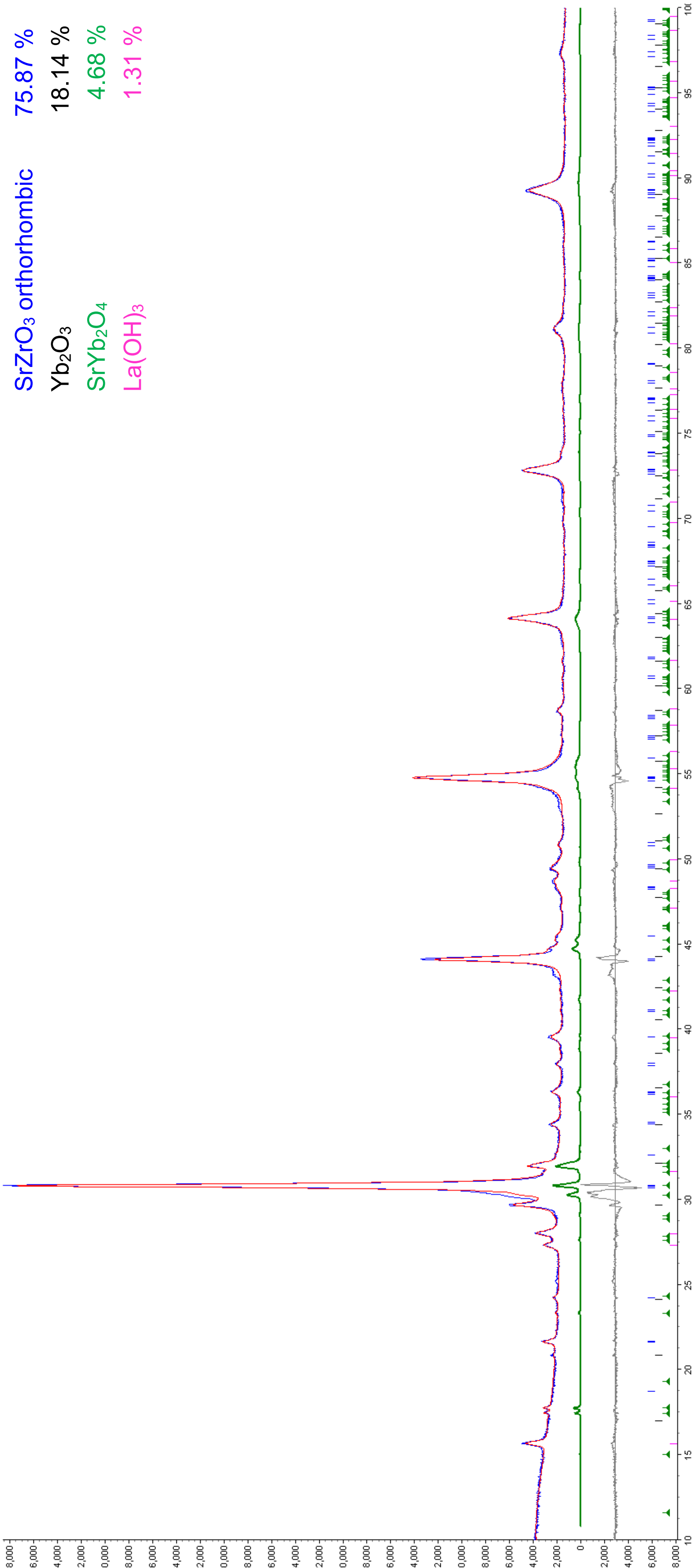

Figure 65c: XRD pattern of calcinated powder of SLZY10.

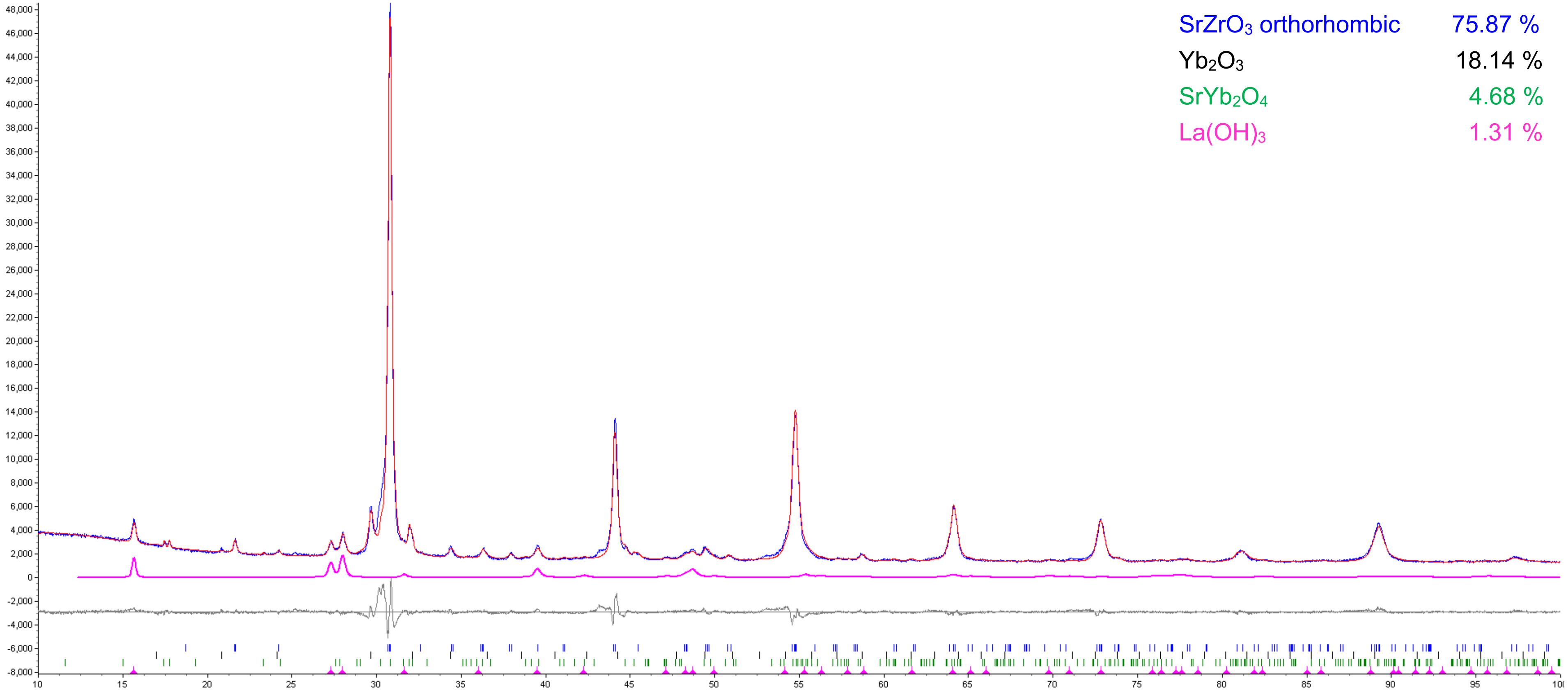

Figure 66d: XRD pattern of calcinated powder of SLZY10.

$Sr_{0.90}La_{0.10}Zr_{0.90}Yb_{0.10}O_3$ – Sintered

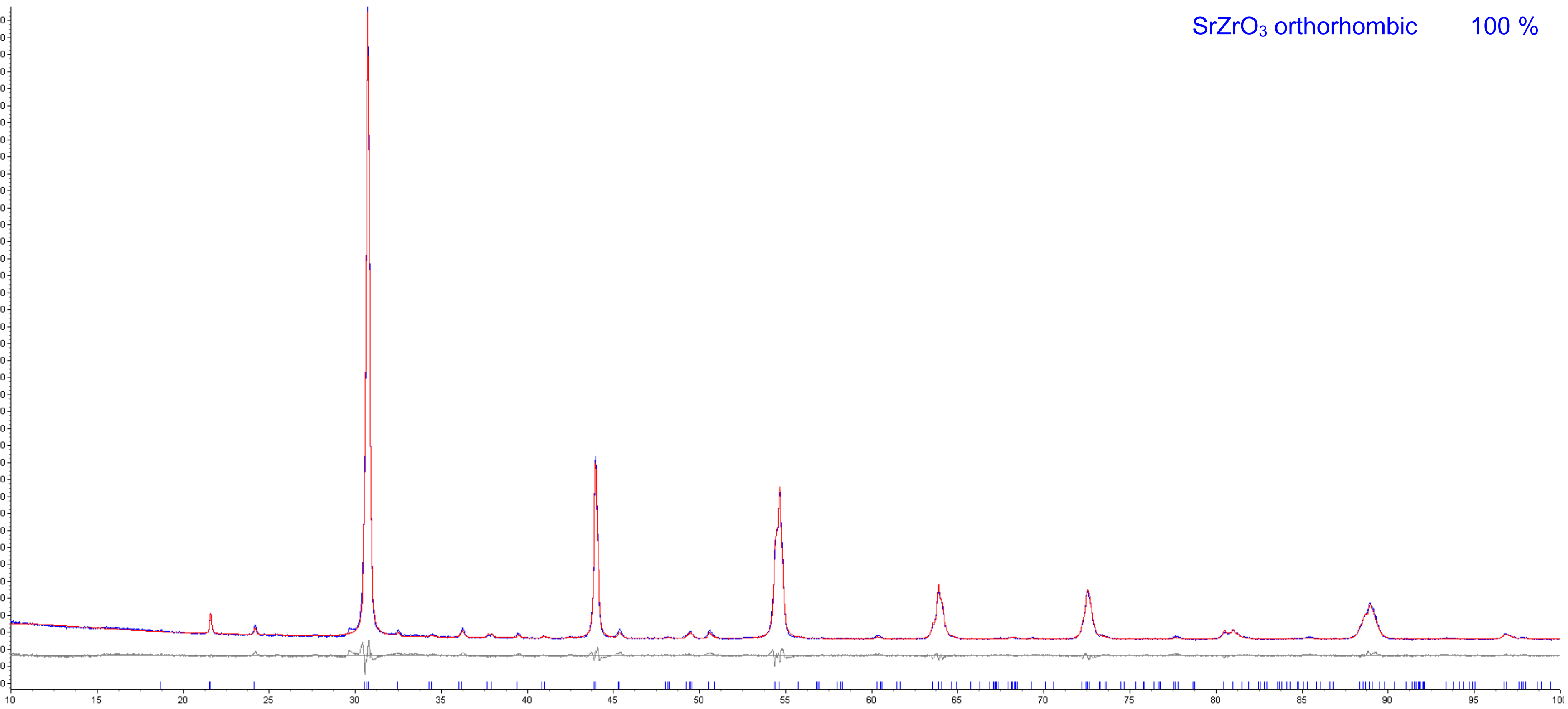

Figure 67: XRD pattern of SLZY10 after sintering.